Experimental and Numerical Investigation on Aerodynamic Performance Degradation on an UAV Airfoil

Master Thesis
by
can. aer. Jakob Röß

conducted at the
Institute of Aerodynamics and Gas Dynamics
University of Stuttgart

Stuttgart, May 2025

Acknowledgements

I would like to express my deepest gratitude to my two supervisors, Ulrich Deck and Dr. Richard Hann, for their invaluable guidance and support throughout this thesis. Their insightful feedback and encouragement have been central to shaping its direction. Without both of them, this would not have been possible.

I am also truly thankful to the members of the working group LaminarWindTunnel at the University of Stuttgart and the members of the UAV Icing Lab at the Norwegian University of Science and Technology for their helpful suggestions and technical support, which contributed greatly to the progress of this work.

Special thanks go to UBIQ Aerospace for generously providing the software and tools essential for the simulations of this thesis.

I also want to thank the Institute of Aircraft Design for providing the additive manufacturing resources needed to manufacture the artificial ice shapes.

Last, I am profoundly grateful to my family and friends for their support, understanding, and belief in me throughout my studies. Their encouragement has been a constant source of strength.

Contents

Nomenclature

Acronyms

2D	Two-Dimensional
3D	Three-Dimensional
AoA	Angle of Attack
CAD	Computer-Aided Design
CFD	Computional Fluid Dynamics
CFL	Courant–Friedrichs–Lewy
CNC	Computerized Numerical Control
DNS	Direct Numerical Simulation
DES	Detached-Eddy Simulation
FAA	Federal Aviation Administration
FDM	Fused Deposition Modeling
IAG	Institute of Aerodynamics and Gas Dynamics
ICAO	International Civil Aviation Organization
IFB	Institute of Aircraft Design
LSB	Laminar Separation Bubble
LWC	Liquid Water Content
MCCS	Maximum Combined Cross Section
MVD	Mean Volume Diameter
NTNU	Norwegian University of Science and Technology
RANS	Reynolds-Averaged Navier-Stokes
SLS	Selective Laser Sintering
TE	Trailing Edge
UAS	Unmanned Aerial System
UAV	Unammend Aerial Vehicle
VTT	VTT Technical Research Centre of Finland

Roman Symbols

c	$[m]$	Chord length
C_d	[-]	Coefficient of drag

C'_d, C'_l	[-]	Uncorrected coefficient of drag, lift
C_l	[-]	Coefficient of lift
$C_{l,max}$	[-]	Maximum coefficient of lift
D	$[N]$	Drag force
e	$[J/kg]$	Specific energy
$\tilde{e}$	$[J/kg]$	Mean specific energy
f_1, f_2, f_3	[-]	Richardson extrapolation parameters
h	$[J/kg]$	Enthalpy
$\tilde{h}$	$[J/kg]$	Specific enthalpy
i, j, k	[-]	Unit vectors in x,y,z direction
K	[-]	Correction factor drag momentum deficit method
$K_{C_l}, K_{C_d}, K_\alpha$	[-]	Wind tunnel correction factors
L	$[N]$	Lift force
l	$[m]$	Characteristic length
Ma	[-]	Mach number
p	$[Pa]$	Static pressure
P_∞	$[Pa]$	Total freestream pressure
$\tilde{p}$	$[Pa]$	Mean pressure
P_{wake}	$[Pa]$	Total integrated pressure in the wake
$p_{Rirchardson}$	[-]	Order of convergence
$Pr_{h=0}$	[-]	Richardson extrapolated solution
q_∞	$[Pa]$	Freestream stagnation pressure
q_L	$[W/m^2]$	Mean heat-flux vector
r	[-]	Grid refinement ratio
Re	[-]	Reynolds number
S	$[m^2]$	Wing area
s	$[m/s]$	Speed of sound
S_ij	$[s^{-1}]$	Mean strain-rate tensor
t	$[s]$	time
T	$[^\circ C]$	Air temperature
U_∞	$[m/s]$	Freestream velocity
u, v	$[m/s]$	Velocities in x,y direction
u''	$[m/s]$	Fluctuating velocity
$\tilde{u}$	$[m/s]$	Mean velocity
w	$[m]$	Wake rake width
y^+	[-]	Dimensionless wall distance

Greek Symbols

α	[°]	Angle of attack
α'	[°]	Uncorrected angle of attack
Δs	[m]	Initial cell height
δ_{ij}	[-]	Kronecker delta
ϵ	[%]	Error
η	$[m^2/s]$	Kinematic viscosity
μ_T	$[m^2/s]$	Eddy viscosity
ρ	$[kg/m^3]$	Density
$\tilde{\rho}$	$[kg/m^3]$	Mean density
σ	[-]	Standard deviation
$\tilde{\tau}$	[Pa]	Reynolds stress tensor

List of Figures

List of Tables

Abstract

Unmanned Aerial Vehicles (UAVs) have in recent years gained an increase in attention driven by technological advancements and the emergence of new business models for commercial and military applications. In-flight poses a significant risk for reliable and safe UAV operation, often resulting in limitations of the operational envelope. Ice accretion on aerodynamic surfaces can lead to significant performance degradation in terms of increased drag and reduced lift. To better understand the aerodynamic impact of ice accreted low Reynolds number airfoils, this thesis investigated the ice-induced aerodynamic performance degradation of the RG-15 airfoil through an experimental and numerical study.

This study investigated four ice shapes representing glaze, mixed, and rime ice conditions. These were investigated at three Reynolds numbers in the range of Re = 100 000 - 300 000. In the experimental measurement campaign, wind tunnel tests at the Model Wind Tunnel at the University of Stuttgart were conducted. Lift and drag forces were measured on a two-dimensional wind tunnel model with and without artificial ice shapes. For the numerical study, two-dimensional steady-state RANS simulations with the k–ω SST turbulence model were performed using the software FENSAP-ICE.

The results show that all ice shapes degrade the aerodynamic performance, with the glaze ice shape inducing the most significant drag increase and lift decrease. The results of the rime ice shapes show a unexpected increase of the maximum coefficient of lift. Furthermore, laminar effects were observed for the lowest Reynolds number regime. The numerical results showed good agreement with the experimental data in the linear lift section, showed however limitations in separated flow regions. The findings of this thesis show that in-flight icing can be a significant risk for UAV operation and demonstrate the validity of a RANS-based numerical approach for modeling the iced airfoil performance.

Kurzfassung

Unbemannte Luftfahrzeuge (UAVs) haben in den letzten Jahren zunehmend an Bedeutung gewonnen, angetrieben durch technologische Fortschritte und das Aufkommen neuer Geschäftsmodelle für kommerzielle und militärische Anwendungen. Vereisung im Flug stellt ein erhebliches Risiko für einen zuverlässigen und sicheren UAV-Betrieb dar und führt häufig zu Einschränkungen im Operationsbereich. Eisbildung auf aerodynamischen Flächen können zu erheblichen Leistungseinbußen in Form von erhöhtem Widerstand und reduziertem Auftrieb führen. Um die aerodynamischen Auswirkungen von Eis auf Flugzeugflächen bei niedrigen Reynolds-Zahlen besser zu verstehen, untersucht diese Arbeit die durch Eis verursachte Leistungsdegradation des RG-15 Profils in einer experimentellen und numerischen Studie.

Untersucht wurden vier Eisformen, die Glaze-, Mixed- und Rime-Eisbedingungen repräsentieren. Diese wurden bei drei verschiedenen Reynolds-Zahlen im Bereich von Re = 100 000 bis 300 000 untersucht. Im Rahmen der experimentellen Untersuchungen wurden Windkanalversuche im Modellwindkanal der Universität Stuttgart durchgeführt. Dabei wurden Auftriebs- und Widerstandskräfte an einem zweidimensionalen Windkanalmodell mit und ohne künstliche Eisformen gemessen. Für die numerische Untersuchung wurden zweidimensionale stationäre RANS-Simulationen mit dem k–ω SST-Turbulenzmodell mit der Software FENSAP-ICE durchgeführt.

Die Ergebnisse zeigen, dass alle Eisformen die aerodynamische Leistung beeinträchtigen, wobei die Glaze-Eisform den stärksten Anstieg des Widerstands und die größte Reduktion des Auftriebs verursacht. Die Ergebnisse der Rime-Eisformen zeigen eine unerwartete Erhöhung des maximalen Auftriebsbeiwerts. Zudem traten im Bereich der niedrigsten Reynolds-Zahl laminare Strömungseffekte auf. Die numerischen Ergebnisse stimmen im linearen Auftriebsbereich gut mit den experimentellen Daten überein, weisen jedoch in Bereichen mit Strömungsablösungen Einschränkungen auf. Die Erkenntnisse dieser Arbeit verdeutlichen das erhebliche Risiko, das von Vereisung für den UAV-Betrieb ausgeht, und zeigen die Anwendbarkeit eines RANS-basierten numerischen Ansatzes zur Modellierung der aerodynamischen Leistung vereister Flügelprofile.

1. Introduction

Aircraft in-flight icing has been a major safety concern for manned aviation aircraft and has in the past caused numerous fatal accidents [14]. In-flight icing is dangerous primarily since it leads to significant performance degradation of the aircraft's lift and control surfaces. Ice accretion also adds mass and can affect sensors and instruments essential for aircraft operation. With respect to these effects, in-flight icing poses challenges for aircraft operation, often resulting in limitations of the aircraft's flight envelope and its ability to fulfill its mission. In-flight icing in manned aviation is generally a well-understood phenomenon, as much research has been performed on the topic until today [24].

In recent years, unmanned aerial vehicles (UAVs) or unmanned aerial systems (UAS) have gained an increase in attention, driven by technological advancements and the emergence of new business models and commercial applications [22]. The consideration of in-flight icing is also highly relevant for safe and reliable UAV operation. There are several fundamental differences between manned aviation aircraft and UAVs. UAVs are typically smaller and fly at lower speeds than manned aviation aircraft [24]. Furthermore, UAVs typically fly at lower altitudes, and their design generally differs significantly from manned aviation aircraft designs. These are examples of differences between manned aviation and UAVs that can affect the icing process and the impact of icing on the operation of the aircraft. However, how these processes are affected is not fully understood yet. Most icing research for manned aviation is conducted at Reynolds number regimes typically one order of magnitude higher than the operational regimes of UAVs, which may result in different icing dynamics and challenges for UAVs [23].

The motivation of this thesis is to provide scientific data in order to support further research and a better understanding of the effects of icing on UAVs at low Reynolds numbers, contributing to the development of safer and more reliable aircraft. Fast development of UAVs and UAV technology poses challenges for aviation safety agencies in providing proper regulations that are both reliable and do not hinder development. Understanding the effects of in-flight icing at low Reynolds numbers is a key factor in providing regulations that fulfill these two conditions. The findings of this thesis may offer valuable contributions to the understanding in this area, which can support innovation and the development of new technologies that address the issue of aircraft icing.

1.1. Goal of the Thesis

The main objective of this thesis is to conduct an experimental and numerical study of the aerodynamic impact of four different artificial ice shapes on the RG-15 airfoil at low Reynolds numbers. The goal of the experimental study is to quantify the aerodynamic penalties induced by different ice shapes representing different icing regimes. The goal of the numerical study is to show the validity of numerical methods for the investigation of iced airfoil aerodynamics. The measurements and simulations will be performed at three Reynolds number regimes: Re = 100 000, 200 000, and 300 000, with angles of attack ranging from $\alpha = -6^\circ$ up to $\alpha = +16^\circ$. Only lift and drag forces are

measured in the experimental study. All simulations are performed as two-dimensional steady-state RANS simulations. To summarize the main goals of this thesis, the key objectives are defined below.

- Conduct an experimental and a numerical study on RG-15 airfoil with artificial ice at low Reynolds numbers to assess the aerodynamic performance degradation
- Discuss and compare experimental and numerical results to existing icing literature
- Evaluate the validity of numerical methods in low Reynolds number icing studies

1.2. Structure of the Thesis

To provide a clear overview to the reader, the structure of the thesis is presented below. This overview is intended to help readers navigate the thesis more easily. Each chapter is briefly summarized to highlight its purpose and how it contributed to the overall objectives.

Chapter 1 - Introduction: The introduction presents the motivation, the objectives, and the scope of this thesis.

Chapter 2 - Fundamentals and Background: This chapter presents key theoretical principles to establish the context for the main matter. This chapter is recommended for readers who are not familiar with in-flight icing, fundamental aerodynamics, and/or fundamentals of computational fluid dynamics.

Chapter 3 - Baseline Airfoil and Definition of Ice Shapes: This chapter presents the baseline airfoil, as well as the background of the four ice shapes investigated in this thesis.

Chapter 4 - Experimental Methods: In the experimental methods, the setup and the methodology for the experimental measurement campaign are explained. This includes an overview of the wind tunnel facility, the applied measurement techniques and introduces the wind tunnel correction factors. Additionally, a description of the wind tunnel model and the artificial ice shapes is provided. Finally, an error analysis is presented.

Chapter 5 - Numerical Methods: This chapter presents the numerical setup and the methodology used for the simulations conducted in this thesis. A short overview of the used software is given. Furthermore, the numerical setups of the clean and iced airfoil performance simulations are presented.

Chapter 6 - Results and Validation: This chapter presents the experimental results and validates the numerical results in comparison to the experimental data. The chapter also includes a thorough discussion of the obtained results and the observed features.

Chapter 7 - Conclusion and Outlook: The final chapter summarizes the key findings of the thesis. Lastly, an outlook for future work is given for this research topic.

2. Fundamentals and Background

This chapter is intended to give the reader more context of the principle topics of this thesis. First, an introduction to atmospheric icing and the three icing regimes of rime, glaze, and mixed ice is given. Fundamental aerodynamics are thereafter shortly discussed to establish key principles used throughout this thesis. Fundamental principles of computational fluid dynamics (CFD) and an introduction to turbulence modeling are also presented. As this chapter only discussed fundamental theory, it is mainly intended to give context for the main matter for a broader reading audience, and readers who already are familiar with these topics are encouraged to skip this chapter.

2.1. Atmospheric Icing

Atmospheric icing is a term that describes the accumulation of supercooled water droplets in the atmosphere that freeze upon impact with surfaces, such as an aircraft's wing. Supercooled water droplets are droplets that have a temperature below the freezing point, but are still in a metastable liquid phase. As an aircraft flies through conditions, where supercooled water droplets exist, the supercooled water droplets can collide with the aircraft's surface and freeze. This is called in-flight icing, as icing occurs mid-air. On the contrary, if icing occurs while the aircraft is on the ground, is called ground icing. As these two icing types differ greatly in their characteristics and mitigation strategies, they are often handled individually in research. This thesis is only concerned with in-flight icing.

The interest in aircraft icing research began in the late 1920s and early 1930s, but it was not before the 1940s and 1950s before the first icing wind tunnels were built and the groundwork of modern icing research was laid [24, 10]. The next revolution of icing research came with the development of computer technology in the 1970s and 1980s, as numerical methods accelerated research, allowing for the analysis of complex flows that were difficult to study experimentally. However, most of this research was conducted on manned aviation aircraft and is not directly transferable to unmanned aerial vehicles. There are key characteristics that fundamentally set apart manned aviation from UAVs, such as vehicle type, size, flight velocity, Reynolds number, weight, used materials, and propulsion technology [24]. In order to understand how these differences affect icing and its aerodynamic effects specific research must be conducted.

Various studies have focused on analyzing the frequency and geographical distribution of atmospheric icing conditions. Bernstein et al. investigated the spatial and temporal distribution of atmospheric icing conditions in Canada and the continental United States [9] as well as Europe, Asia, and the Globe [8], and concluded that atmospheric icing conditions are a global phenomenon that can occur all year around. In a more specific report, Sørensen et al. [48] analyzed frequencies of potential atmospheric icing conditions in the Norwegian airspace and surrounding areas, and came to the same conclusion, that icing can occur all year around. The analysis also showed that large geographical areas are exposed to an icing risk of as much as 50% from October through February, thus limiting the aircraft's operational envelopes drastically.

As already explained, in-flight icing occurs when aircraft fly through clouds of supercooled water droplets. When these supercooled water droplets collide with an aircraft's surface, the droplets impinge on- and freeze to the surface. The aircraft's surface promotes the nucleation of ice, as the contact between the supercooled droplet and the aircraft surface provides favorable conditions for the transition from the metastable liquid phase to solid ice. The freezing process significantly dependents on both the atmospheric conditions and the specifications of the aircraft. The ice accretion rate, which is defined as how much mass of ice is accreted over a time period, highly depends on the air temperature, the liquid water content (LWC), and the droplet size, which is often defined as the mean volume diameter (MVD). Additionally, the aircraft velocity and the aircraft size impact the ice accretion rate significantly [23]. The added mass of the ice accretion influences the aircraft with several effects. The added mass must be countered by increasing the lift force of the aircraft. This can be achieved by flying at a higher angle of attack or flying at a higher velocity. Both measures will affect the endurance, range, or stall margins [23]. Also, added mass changes the center of gravity, altering the stability and maneuverability of the aircraft. For smaller and lighter aircraft, like UAVs, the effects of added mass, caused by ice accretion, are more significant, because of low initial weight and size.

Additionally, to the added mass effects, ice accretion also leads to aerodynamic effects. Ice accretion on the aerodynamic surfaces changes the surface's geometry and roughness. This leads to a change in the aerodynamic characteristics, such as lift, drag, and pitching moment of the aircraft. The severity of these aerodynamic effects are highly dependent on the form of the ice accretion. Depending on the atmospheric and aircraft-specific conditions, ice accretion forms different icing morphologies or ice shapes. The Federal Aviation Administration (FAA) [15] distinguishes between three ice types based on the appearance and structure of the ice. These three ice types will be covered individually below, as the same characterization will be used throughout this thesis.

2.1.1. Rime Ice

Rime ice forms in an instantaneous or rapid freezing process. Rime ice shapes are generally streamlined since the supercooled water droplets freeze almost instantly upon impingement. Low temperatures, typically in the range of -15 °C to -30 °C, low aircraft velocities, low LWC, and small MVD are beneficial to rime ice formation [22]. Naturally, these conditions are more present in higher altitudes, which can explain the high frequency of rime ice formation in high altitudes. Due to the rapid freezing of the droplets, air can be trapped inside the ice, resulting in opaque and rough ice. The trapped air also contributes to a low density of the ice. An example of a rime ice shape is displayed in Figure 2.1a.

2.1.2. Glaze Ice

Glaze ice, also referred to as clear ice, forms in temperatures close to the freezing point. In these temperatures, the supercooled water droplets don't freeze instantly after impingement on a surface. The supercooled water droplets collide with the surface and may be partially transported toward the trailing edge before freezing. Due to this slow freezing process, glaze ice can build severe ice shapes from an aerodynamical point of view. High ice accretion may lead to the formation of characteristic horn-like protrusions, as seen in Figure 2.1b. Glaze ice is often denser and clearer compared to rime ice because less air is trapped inside the ice during the slower freezing process. High aircraft velocities, high LWC, and large MVD are beneficial to the formation of glaze ice.

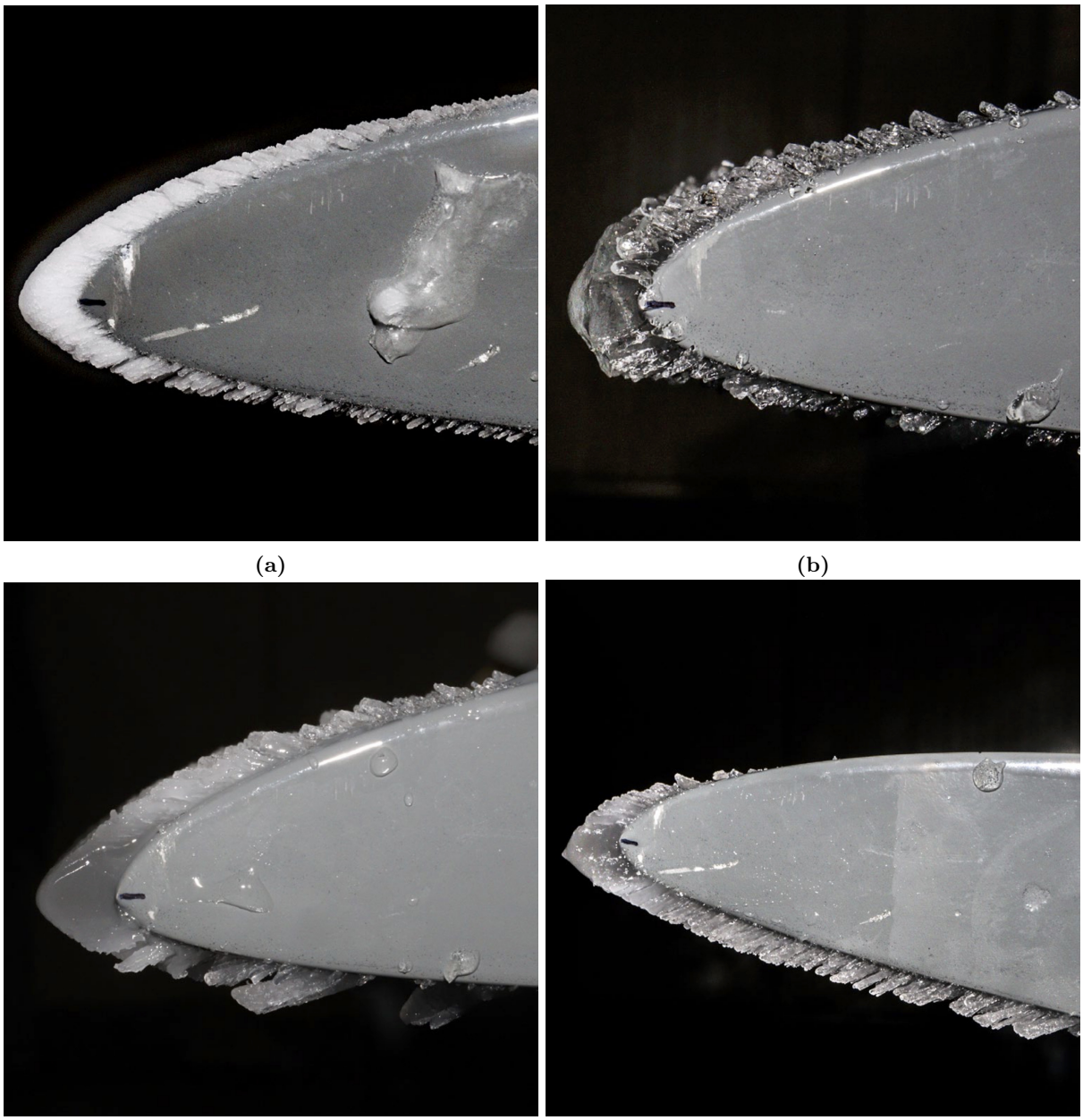

(a) **(b)**

(c) **(d)**

Figure 2.1.: Examples of ice types: (a) rime ice, (b,c) mixed ice, (d) glaze ice (images courtesy of Richard Hann [22]).

2.1.3. Mixed Ice

Mixed ice is a mixture of rime and glaze ice. It forms in between the icing conditions of rime and glaze ice. The freezing process for mixed ice is partially instantaneous. Parts of the supercooled water droplets freeze upon impact with the aircraft's surface, and parts will remain in a liquid state. This leads to a combination of rime and glaze ice. Mixed ice also tends to form severe ice shapes with horn-like protrusions if the ice accretion is high. The ice shapes of mixed ice are therefore comparable to glaze ice shapes, however generally with less significant horns. Two examples of a mixed ice shape can be seen in Figure 2.1c and Figure 2.1d.

2.2. Fundamentals of Aerodynamics

In aerodynamics, typically non-dimensional coefficients are used instead of forces. Non-dimensional coefficients allow for a comparison of different airfoils and their aerodynamic characteristics. For this thesis, the coefficient of lift, C_l, and the coefficient of drag, C_d, are of interest. The coefficient of lift is defined as the lift force, L, divided by the freestream dynamic pressure, $q\infty$ and the wing area, S.

$$C_l = \frac{L}{q_\infty \cdot S} \tag{2.1}$$

The coefficient of drag is defined analogously, but with the drag force, D, instead of the lift force.

$$C_d = \frac{D}{q_\infty \cdot S} \tag{2.2}$$

The dynamic pressure, which is used in the two equations above, is a function of the density, ρ, and the free stream velocity, U_∞.

$$q_\infty = \frac{\rho}{2} U_\infty^2 \tag{2.3}$$

Other key parameters used throughout this thesis are similarity parameters. They are also non-dimensional and enable comparison of similar flows. The aerodynamic results of scaled models are transferable when the scaled model and original model are geometrically and physically similar. The first similarity parameter is the Reynolds number, Re. The Reynolds number is a function of the density of the medium, ρ, the free stream velocity, U_∞, the characteristic length, L, and the kinematic viscosity, η as presented in Equation 2.4. For airfoils, the chord length is typically used as the characteristic length. In literature, the Reynolds number is often described as the ratio of inertial to viscous forces.

$$\mathrm{Re} = \frac{\rho \cdot U_\infty \cdot l}{\eta} \tag{2.4}$$

In viscous flows, two different types of flows exist. Laminar flow, in which streamlines are ordered and smooth and turbulent flow, in which streamlines are disordered and chaotic. If the critical Reynolds number is exceeded, the flow transitions from laminar to turbulent flow. In turbulent flow, the boundary layer is thicker than in laminar flow, and the velocity profile near the wall is fuller due to a higher transport of momentum. This results in an increase of the shear stress and, consequently, a higher skin friction. The higher momentum near the wall leads also to a boundary layer that is less prone to separate under adverse pressure gradients [41].

At low Reynolds numbers, laminar flow phenomena can be observed. One significant phenomenon is the laminar separation bubble (LSB). A LSB forms, when a laminar boundary layer is subjected to an adverse pressure gradient which cannot be overcome by the flow. The laminar boundary layer then separates and forms a laminar separation bubble. In contrast to turbulent separation, which is generally more stable and persistent, LSB's are inherently unstable and sensitive to disturbances. This characteristic often leads to a laminar-turbulent transition downstream of the separation point, and can further lead to a reattachment of the turbulent boundary layer. The presence of a LSB significantly influences the flow characteristics and affects the aerodynamic performance [41].

Another similarity parameter is the Mach number, Ma. The Mach number describes the ratio of the freestream velocity, U_∞, to the speed of sound, s, in a medium, as defined in Equation 2.5. The Mach number is often used to represent the compressibility effects of the flow. For Mach numbers, $\mathrm{Ma} < 0,3$, the flow can safely be assumed incompressible, which means that the density is assumed constant [5].

$$\mathrm{Ma} = \frac{U_\infty}{s} \tag{2.5}$$

2.3. Computational Fluid Dynamics

Computational Fluid Dynamics (CFD) plays a crucial role in modern engineering and science. CFD stands as a synonym for the numerical investigation of fluid flows [42]. Physical experiments are sometimes complex, time-consuming, and costly. CFD enables engineers and scientists to simulate and analyze fluid flow, heat transfer, and related physical phenomena using numerical methods. Conservation of mass, conservation of momentum, and conservation of energy stand as the three fundamental equations of classical mechanics and describe physical problems mathematically. With CFD, these fundamental equations are solved numerically in order to approximate the real flow solution. These three equations of conservation are collectively known as the Navier-Stokes equations.

2.3.1. Navier-Stokes Equations

The Navier-Stokes equations are a set of partial differential equations that describe the conservation of mass, momentum, and energy. The instantaneous, or exact compressible Navier-Stokes equations can be written as follows [52]:

$$\frac{\partial \rho}{\partial t} + \frac{\partial}{\partial x_i}(\rho u_i) = 0 \tag{2.6}$$

$$\frac{\partial}{\partial t}(\rho u_i) + \frac{\partial}{\partial x_j}(\rho u_j u_i) = -\frac{\partial p}{\partial x_i} + \frac{\partial \tau_{ji}}{\partial x_j} \tag{2.7}$$

$$\frac{\partial}{\partial t}\left[\rho(e + \frac{1}{2}u_i u_i)\right] + \frac{\partial}{\partial x_j}\left[\rho u_j(h + \frac{1}{2}u_i u_i)\right] = \frac{\partial}{\partial x_j}(u_i \tau_{ij}) - \frac{\partial q_j}{\partial x_j} \tag{2.8}$$

As stated, these equations are instantaneous, meaning they capture the exact state of the flow at each moment in time and every point in space. In CFD these equations can be solved with direct numerical simulations (DNS). However, this requires a very high resolution in both time and space in order to resolve all the spatial and temporal scales of turbulent flow. This results in considerable requirements of high computational effort, which makes DNS simulations impractical for most applications. To reduce the computational effort required, simplifications of the Navier-Stokes equations were introduced as approximations of the relevant physics. The most common approach is averaging the Navier-Stokes equations over time and/or space.

2.3.2. Turbulence Modeling

The Reynolds Averaged Navier-Stokes equations introduce a time-averaging approach. The variables of the Navier-Stokes equations are split into a mean, $\tilde{u_i}$, and a fluctuating part, u_i'', as Equation 2.9 demonstrates.

$$u_i = \tilde{u}_i + u_i'' \tag{2.9}$$

For compressible flow problems, the Favre-averaged Navier-Stokes equations are introduced, where a time- and density-averaged approach is used. The Favre-averaged Navier-Stokes equations can be written as follows:

$$\frac{\partial \bar{\rho}}{\partial t} + \frac{\partial}{\partial x_i}(\bar{\rho}\tilde{u}_i) = 0 \tag{2.10}$$

$$\frac{\partial}{\partial t}(\bar{\rho}\tilde{u}_i) + \frac{\partial}{\partial x_j}(\bar{\rho}\tilde{u}_j\tilde{u}_i) = -\frac{\partial \bar{p}}{\partial x_i} + \frac{\partial}{\partial x_j}\left[\bar{\tau}_{ji} - \overline{\rho u_j'' u_i''}\right] \tag{2.11}$$

$$\begin{aligned} &\frac{\partial}{\partial t}\left[\bar{\rho}(\tilde{e} + \frac{\tilde{u}_i\tilde{u}_i}{2}) + \frac{\overline{\rho u_i'' u_i''}}{2}\right] + \frac{\partial}{\partial x_j}\left[\bar{\rho}\tilde{u}_j(\tilde{h} + \frac{\tilde{u}_i\tilde{u}_i}{2}) + \tilde{u}_j\frac{\overline{\rho u_i'' u_i''}}{2}\right] \\ &= \frac{\partial}{\partial x_j}\left[-q_{L_j} - \overline{\rho u_j'' h''} + \overline{\tau_{ji} u_i''} - \overline{\rho u_j'' \frac{1}{2} u_i'' u_i''}\right] + \frac{\partial}{\partial x_j}\left[\tilde{u}_i(\bar{\tau}_{ij} - \overline{\rho u_i'' u_j''})\right] \end{aligned} \tag{2.12}$$

The difference between the conventional Navier-Stokes equations and the Favre-averaged Navier-Stokes equations is the appearance of the Favre-averaged Reynolds-stress tensor, τ_{ij}:

$$\bar{\rho}\tau_{ij} = -\overline{\rho u_i'' u_j''} \tag{2.13}$$

This stress tensor cannot be calculated due to the known closure problem [52], and must therefore be approximated with models. Joseph Boussinesq introduced the eddy viscosity hypothesis in 1877, where he postulated that the Reynolds stresses can be approximated by an eddy viscosity.

$$\bar{\rho}\tau_{ij} = -\overline{\rho u_i'' u_j''} = 2\mu_T(S_{ij} - \frac{1}{3}\frac{\partial \tilde{u}_k}{\partial x_k}\delta_{ij}) - \frac{2}{3}\bar{\rho}k\delta_{ij} \tag{2.14}$$

This concept reduces the number of unknowns of the Favre-averaged Navier-Stokes-Equations to one, the eddy viscosity, μ_T. Since the postulation of Boussinesq, different turbulence models have been introduced with various approaches on how to approximate μ_T. One way of characterizing the different turbulence models is by dividing them into the number of transport equations used to determine μ_T. There are one-equation turbulence models, like the Spalart-Allmaras, and two-equation turbulence models, like the k–ϵ or k–ω SST turbulence models. Both the Spalart-Allmaras and the k–ω SST turbulence models have been applied for iced-airfoil performance simulations, and will therefore be introduced with their advantages and disadvantages.

The Spalart-Allmaras model is a turbulence model that is based on one transport equation designed to calculate the eddy viscosity [46]. The Spalart-Allmaras model has been widely used for many applications since it offers high numerical stability and good results for clean airfoils at low Reynolds

numbers and low angles of attack. Aftab et al. [1] investigated the quality of the results of the turbulence model at low Reynolds numbers. They showed that the Spalart-Allmaras turbulence model showed good results, however fails to capture the flow physics, that occur at low Reynolds numbers.

The k–ω SST model is a two-equation turbulence model developed by Menter in 1994 [36], and is based on the original k–ω model developed by Wilcox [51]. The k–ω SST model combines the k–ϵ model and the k–ω model with the help of a blending function. The k–ϵ model is applied in the free stream, while the k–ω model is applied in the inner boundary layer near the wall. This strategy utilizes each model's strengths. The k–ω SST model is known to perform well at low Reynolds number regimes and low angles of attack [1], and is therefore, one of the most popular turbulence models for airfoil simulations.

Both discussed turbulence models have been applied in numerical studies of iced airfoils in literature [34, 45, 22]. Hann [22] concluded that the k–ω SST turbulence model had a better agreement with the experimental results of streamlined ice shapes compared to the Spalart-Allmaras model, while the Spalart-Allmaras model was more accurate for glaze ice shapes. Shim et al. [45] also concluded that the quality of the results of each turbulence model depends on the ice shape. For streamlined ice shapes, e.g. rime ice shapes, the k–ω SST model performs better, while for more rugged ice shapes, e.g. glaze ice shapes, the Spalart-Allmaras model performs better. Both models however fail to predict separated regions, just as the stall, correctly. These conclusions are supported by the findings of Martini et al. [34] and Shim et al. [45]. For this thesis, the k–ω SST turbulence model is chosen, because of the generally better performance of clean airfoils and streamlined ice simulations.

3. Baseline Airfoil and Definition of Ice Shapes

3.1. Baseline Airfoil

The baseline airfoil of this investigation is based on the RG-15 airfoil, designed by Rolf Girsberger in 1983. Rolf Girsberger designed the RG-15 airfoil using the Eppler program developed by Richard Eppler. The RG-15 airfoil was originally designed for RC sailplanes, as Girsberger tried to build his own high-performance RC sailplane. Girsberger succeeded with his design, and the RG-15 became one of the most successful RC sailplane airfoils of all time [17]. The original RG-15 airfoil has a maximum thickness of 8.9% at 30.2% chord with a maximum camber of 1.8% at 39.7% chord. Girsberger designed the RG-15 airfoil upper side, to ensure a gradual shift of the transition point toward the leading edge with an increasing angle of attack. On the lower side, Girsberger aimed for an almost constant laminar run length over the typical angles of attack during fast flight. This resulted laminar bucket with a more pronounced lower edge of the laminar bucket relative to the upper edge [19].

The experimental results of wind tunnel measurements conducted by Selig et al. [43] show the existence of a laminar separation bubble up to approximately a Reynolds number of Re = 200 000 for the RG-15 airfoil . The results also show that it is reasonable for the application of a turbulator on the upper side at approximately 60% chord for Reynolds number below this.

For this thesis, the original RG-15 airfoil with a blunt trailing edge was used. This blunt trailing edge has a width of 0.667% chord (1.334 mm). As a result of the blunt trailing edge, the airfoil geometry deviated from the original RG-15 airfoil. The new RG-15 airfoil has a maximum thickness of 9.11% at 0.324 % chord and a maximum chamber of 1.76 % at 0.398 % percent chord. The deviation from the original RG-15 with a sharp trailing edge is displayed in Figure 3.1. The airfoil coordinates of the RG-15 airfoil used throughout this work are attached to Appendix A.

3.2. Definition of Ice Shapes

Four different ice shapes were investigated in this thesis. Three of those were obtained by Hann et al. [26] in an experimental icing wind tunnel campaign at the VTT Technical Research Centre of Finland in the fall of 2022. These three ice shapes represent wet (glaze ice, -2°C), mixed (-4°C), and dry (rime ice, -10°C) icing conditions [26]. Table 3.1 shows the testing conditions in which the three ice shapes were produced. The fourth ice shape that was investigated in this thesis is a second rime ice shape, which was produced at a lower static temperature of -15°C, an angle of attack of 0°, and a liquid water content of 0.53g/m^3. In order to differentiate between the two rime ice shapes, they will from now on be called rime (-10°C) and rime (-15°C).

From the real ice shapes, digital three-dimensional models were obtained by a photogrammetry method [26]. Since the ice shapes originally were produced on an RG-15 airfoil with a chord length of 300 mm, the ice shape models had to be scaled down to fit the RG-15 airfoil with the shorter

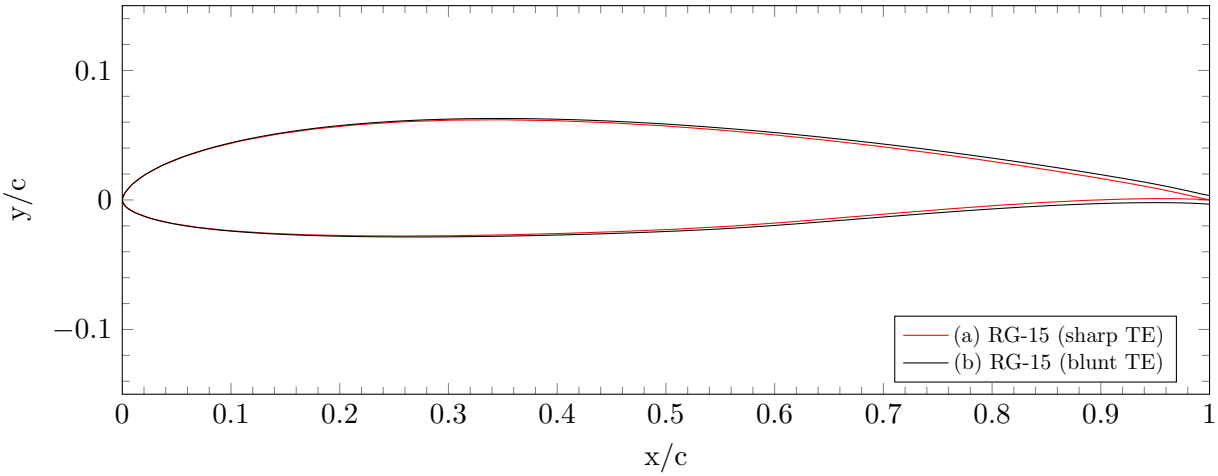

Figure 3.1.: Comparison of two RG-15 airfoil geometries: (a) original profile with a sharp trailing edge and (b) RG-15 profile with blunt trailing edge.

chord length of 200 mm investigated in this thesis. This scaling process reduces the absolute ice thickness of the ice shape. The relative ice thickness, which is defined as the absolute ice thickness normalized by the chord length, remains unchanged. Attention should be drawn to this relationship, as for natural ice accretion the relative ice thickness is dependent on the chord length [25, 47]. This means that the aerodynamic performance degradation cannot be directly coupled to the atmospheric conditions listed in Table 3.1, and must be viewed independently.

Test Parameters	**Value**
Airfoil	RG-15
Span	0.59 m
Chord	0.3 m
Angle of attack	$+4^{\circ}$
Liquid water content (LWC)	0.44 g/m^3
Median volume diameter (MVD)	23 μm
Duration	20 min
Static temperature (glaze, mixed, rime)	[-2, -4, -10]°C
Reynolds numbers	[5.7, 5.8, 6.0]·10^5
Relative humidity	95-100%

Table 3.1.: Test case conditions of ice shapes [26].

Post-processing the obtained three-dimensional models of the ice shapes involved multiple steps and was performed using Siemens NX. First, the meshes of the three-dimensional models were simplified in order to reduce file size while preserving the three-dimensional surface roughness features of the ice. Next, the edges were cut off, in order to remove any boundary artifacts of the real ice accretion. The resulting model had a span of 61.67 mm. In order to cover to whole wind tunnel model, this part was multiplied and combined six times, resulting in a symmetric ice shape model with a span of 370 mm.

In the wind tunnel measurement campaign, the glaze, mixed and rime (-10°C) ice shapes were tested as three-dimensional ice shapes. The rime (-15°C) ice shape was tested as a constant cross-section

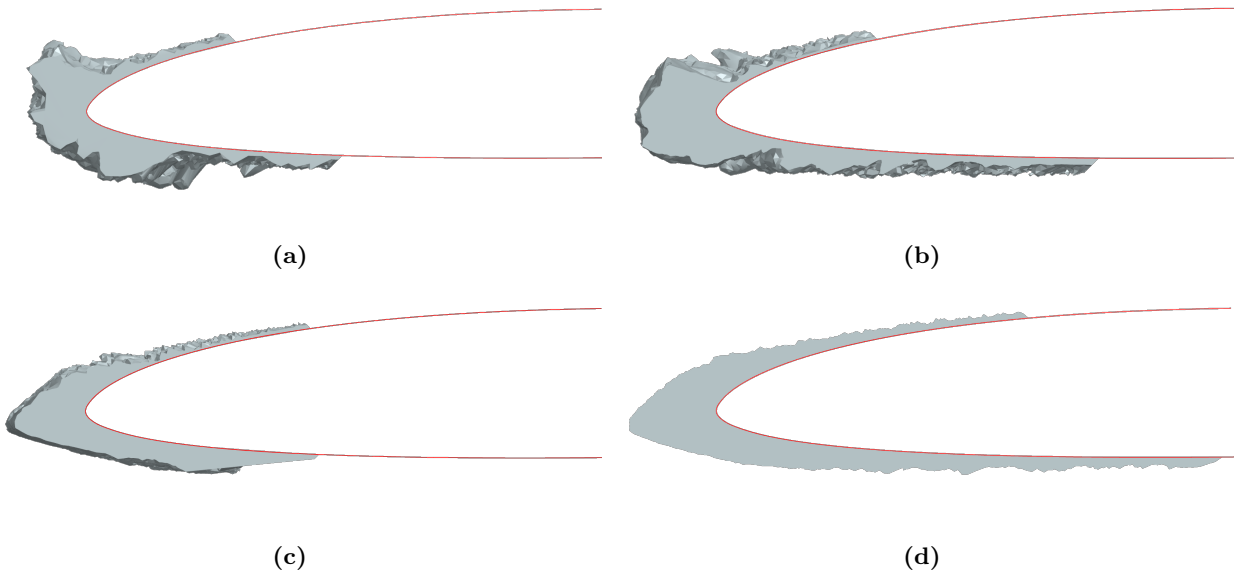

Figure 3.2.: Comparison of four ice shape geometries: (a) glaze, (b) mixed, (c) rime (-10°C), and (d) rime (-15°C).

ice shape (i.e. two-dimensional ice shape). For the simulations, all four ice shapes were simulated as constant cross-section ice shapes, since only two-dimensional simulations were performed. There are several methods to convert a three-dimensional geometry into a two-dimensional curve. One approach is called Maximum Combined Cross Section (MCCS). This method utilizes a finite number of sections, where the outer geometry is traced as section curves. All section curves can be projected onto a single plane. Adding the outermost parts of the section curves together results in the maximum combined cross-section curve. This method is explained thoroughly in [13]. For this method, the higher the number of sections used, the closer the result is to the true MCCS of the three-dimensional geometry. In this work, instead of using a finite number of sections to obtain the MCCS curve, the shadow function in Siemens NX was used, where only the outermost parts of a three-dimensional body are projected onto a plane. This results in the true maximum combined cross-section of the ice shapes. The four different ice shapes are displayed in Figure 3.2.

4. Experimental Methods

All measurements were performed in the experimental facilities of the Institute of Aerodynamics and Gas Dynamics (IAG) at the University of Stuttgart. The measurement campaign consisted of lift and drag measurements of the clean RG-15 airfoil, glaze ice, mixed ice, rime (-10°C) ice, and rime (-15°C) ice at the Reynolds number regimes Re = 100 000, 200 000, and 300 000 and angles of attack ranging from $\alpha = -6°$ up to $\alpha = +16°$. Additionally, lift and drag measurements of a clean Eppler E374 airfoil model were conducted for reference in the identical Reynolds number regimes and angle of attack range. This chapter gives a detailed presentation of the wind tunnel facility, the measurement techniques and correction factors applied in the measurements, the wind tunnel model, and the artificial ice shapes. The chapter also presents an error analysis, as well as a comparison of the E374 measurement results compared to existing data.

4.1. Wind Tunnel Facility

The experimental measurement campaign was performed at the Model Wind Tunnel at the University of Stuttgart. This wind tunnel is an open return wind tunnel (Eiffel-type) with a closed test section, as shown in Figure 4.1. The wind tunnel has a total length of 7 m, and has a contraction ratio of 19.8:1. The rectangular test section has an area of 0.22 m^2. From the 4 kW - three-phase motor, a maximum speed of 30 m/s can be reached in the test section. The wind tunnel supports models with a maximum chord length of 200 mm, which correlates to Reynolds numbers of up to Re = 400 000. The turbulence intensity of the Model Wind Tunnel ranges from $2 \cdot 10^{-4}$ to $8 \cdot 10^{-4}$ [39]. Wind tunnel models are mounted horizontally to freely rotating end plates, which are connected to a load cell below the test section. A traverser system is located behind the mounted wind tunnel model, carrying a wake rake. The angle of attack is can be adjusted manually with a motor, and is measured with a Megatron MCP 40 potentiometer. Data acquisition includes signal conditioning, A/D conversion, and data processing in Matlab. The wind tunnel facility supports lift, drag, and pressure distribution measurements. The lift- and drag measurement systems are explained individually below, as they are of interest for this thesis.

4.2. Measurement Techniques

4.2.1. Lift Measurement

As explained in section 4.1, was the model connected to a standard bending beam load cell (HBK Z6-2) below the test section, which measured the lift force. A mechanical scale, which was used in the calibration process of the lift force, connected the mounting plates of the model to the load cell. The output voltage of the load cell was then amplified with a signal amplifier (HBM-KWS 3072) and conditioned with a low-pass filter (IMD MS-210R). Further, an analog converter (NI USB-6218) converted the analog signal into a digital signal with a sample rate of 20,000 Hz and sample time of

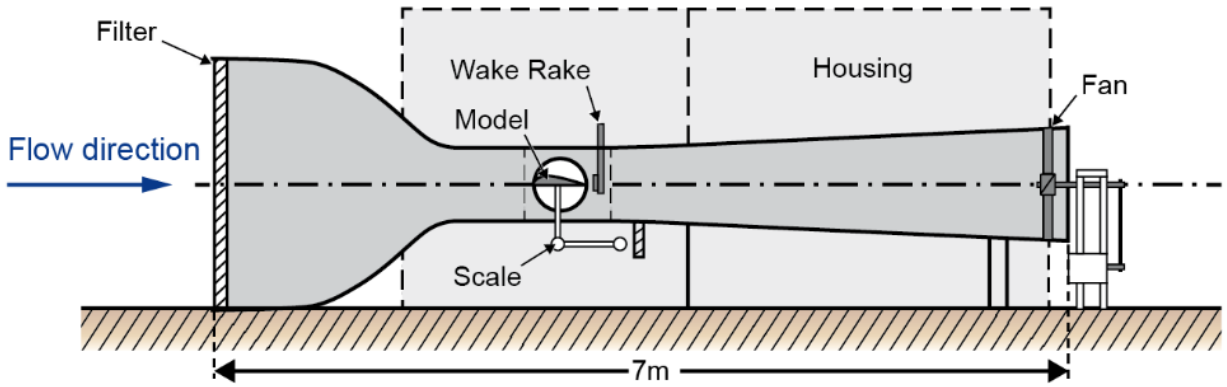

Figure 4.1.: Schematic of the Model Wind Tunnel facility at the University of Stuttgart [39].

0.01 s. The digital signal was then further processed by a Matlab program. From the conditioned and sampled signal, the uncorrected coefficient of lift was calculated directly with Equation 2.1. Figure 4.2 shows the different systems which are involved in the signal conditioning and acquisition process of the lift force measurement.

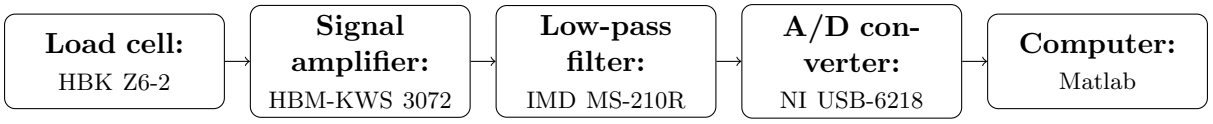

Figure 4.2.: Block diagram of the lift measurement chain.

Before each measurement run, the lift was calibrated using calibration weights. From the expected maximum coefficient of lift, the expected maximum lift force was calculated. This served as the calibration weight used in the calibration process. First, without any weight on the mechanical scale, the zero point of the lift force was measured. Then, the calculated maximum weight was placed onto the mechanical scale and measured by the load cell. From the two measurements, a linear correlation curve was calculated for the relationship between the output voltage of the load cell and the lift force. It was observed that the gradient of the curve changed when applying a negative lift force. To compensate for the non-linearity, a second correlation curve was calculated with the same procedure, but in the negative direction. The final step of the calibration process included the measurement of the calibration error. The average calibration error of the lift force of all measurements was $\epsilon_{lift} = -0.005488\%$ with a standard deviation of $\sigma_{lift} = 0.037354\%$.

The measurement procedure of the lift was conducted in parallel to the drag measurement, which will be described in detail in the next section. At each angle of attack, as the traversing system moved in the spanwise direction, 62 measurements of the lift force were automatically made. These 62 measurements were equally distributed over the travel distance of the traversing system and had the same spanwise positions as the drag measurements. At each measurement point, the coefficient of lift was then calculated, resulting in 62 values for the coefficient of lift. These were averaged, to obtain the value of the uncorrected coefficient of lift for the measured angle of attack.

4.2.2. Drag Measurement

The drag forces are often in the order of one magnitude lower than their lift counterparts, posing challenges in accurate measurements using a load cell. Therefore, the experimental setup for the drag measurement was based on the momentum deficit method developed by Jones [30]. The drag force can be calculated from the momentum loss in the wake of the airfoil, which can be obtained by integrating the momentum deficit over the width of the wake [30]. Figure 4.3 is a visualization of the principle of the momentum loss over an airfoil. Applying the equations of conservation of mass and momentum to the control volume shown in Figure 4.3, Equation 4.1 can be derived to calculate the drag force per unit span, d.

$$d = \rho \int_{-\infty}^{\infty} u(U_\infty - u)dy \tag{4.1}$$

The applied method used for the measurements at the Model Wind Tunnel was introduced by Althaus [2] and is also used in the larger Laminar Wind Tunnel at the University of Stuttgart. According to Althaus, the uncorrected coefficient of drag can be calculated as defined in Equation 4.2.

$$C'_d = K \cdot \int_{wake} g_c \cdot \frac{dy_w}{c} \tag{4.2}$$

The factor K is a function of the maximum total pressure in the wake, the static pressure difference, and the stagnation pressure of the freestream. The total integral pressure loss was obtained through experimental integration with a wake rake. For all measurements, a wake rake consisting of 20 pitot tubes spread equally over a wake rake width of 61 mm was used. The wake rake was mounted on the traversing system approximately 45% of the chord length downstream of the trailing edge of the wing model. Utilizing the experimental integration simplifies Equation 4.2 to Equation 4.3.

$$C'_d = K \cdot \frac{P_\infty - P_{wake}}{q_\infty} \cdot \frac{w}{c} \tag{4.3}$$

Here, $P_\infty - P_{wake}$ is the total pressure difference between the freestream and the wake, q_∞ is the stagnation pressure of the freestream, w is the width of the wake rake, and c is the chord length. In total, four pressure measurements were needed for the calculation of the uncorrected coefficient of drag: the total pressure difference, the static pressure difference, the maximum total pressure in the wake, and the stagnation pressure of the freestream. The stagnation pressure was measured with a Furness Controls Ltd. MDC FC001 micromanometer, with a maximum range of 1000 Pa and five different range settings (1%, 3%, 10%, 30%, and 100%). The maximum total pressure in the wake was also measured with a Furness Controls Ltd. MDC FC001 with five different range settings and a maximum range of 1000 Pa. The total pressure difference and the static pressure difference were measured with a Furness Controls Ltd. MDC FC014 micromanometer [18]. The MDC FC014 micromanometer has three different range settings (1%, 10%, and 100%). The maximum range is ±100 Pa, which corresponds to an approximate velocity range of 0-12 m/s. The MDC FC014 micromanometer has an accuracy of ±0.5% full scale, and a resolution of 1% each range.

At each angle of attack, the wake rake was positioned manually into the center of the wake. This was done visually with a multi-tube liquid manometer, which was connected to the wake rake pitot tubes, or by observing the maximum pressure reading of the micromanometer measuring the maximum total pressure in the wake. As three of the ice shapes were three-dimensional, the center position

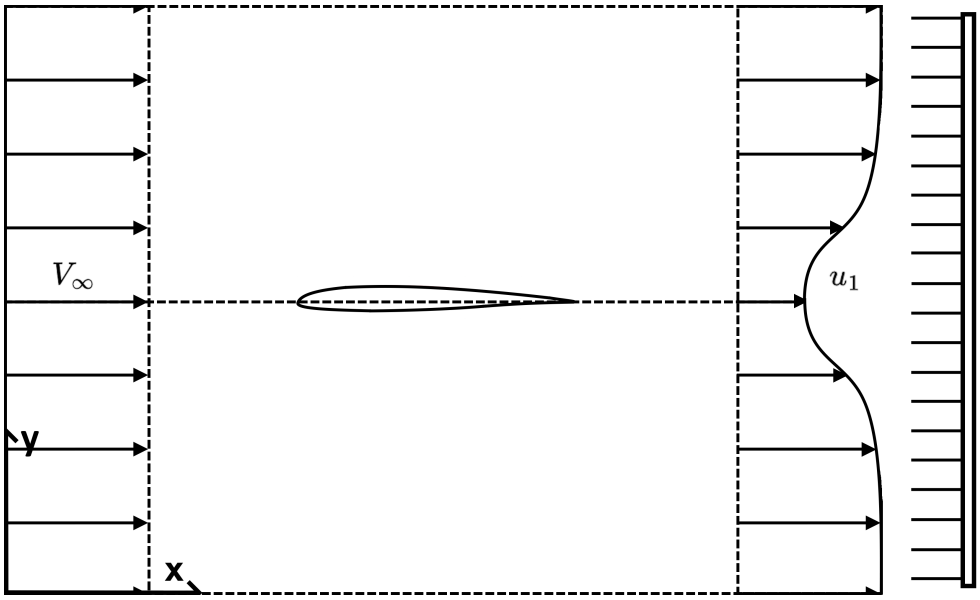

Figure 4.3.: Schematic of the principle of the momentum deficit method.

and the shape of the wake changed since the cross-section of the ice shape changes in the spanwise direction. To ensure accurate values for the coefficient of drag for the complete wing model, 62 single measurements were taken over the span of 123 mm. The 62 single measurements were then averaged, to calculate the uncorrected coefficient of drag for the measured angle of attack. This was done in order to mitigate the influence of the spanwise non-uniformity of the wake, which is also a well-known phenomenon for constant cross-section wings [4]. The drag measurements were stopped as soon as the width of the wake was larger than the wake rake.

The measurement signals of the micromanometers were conditioned in a low pass filter of the type IMD MS-210R. Then the analog signals was converted to a digital signals with the same analog to digital converter (NI USB-6218), as for the lift measurements. The signals of the pressure measurements were also sampled with a sample rate of 20,000 Hz and a sample time of 0.01 s. Lastly, the digital signals were processed in Matlab, where the coefficient of drag was calculated.

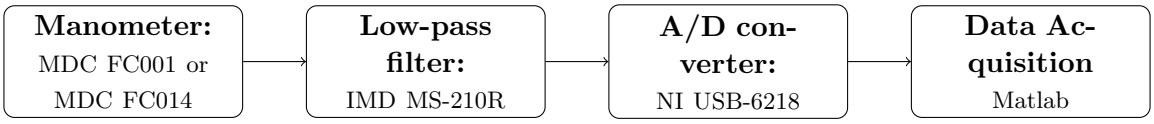

Figure 4.4.: Block diagram of the pressure measurement chain.

4.3. Wind Tunnel Correction Factors

Due to the restriction of the wind tunnel walls of a closed test section, the measured aerodynamic forces include extraneous forces that must be subtracted out [44]. Glauert [20] presented the Standard-Tunnel-Wall corrections, that are based on four effects of the wind tunnel walls on the flow over a model. These Standard-Tunnel-Wall corrections are applied in the Model Wind Tunnel of the University of Stuttgart and are therefore presented below. This section will however not cover the derivation of these correction factors. A detailed description of the derivation of the correction

factors can be found in [3].

Solid blockage A object present in a closed test section obstructs the flow, and reduces the effective flow area of the freestream. From the continuity and Bernoulli's equation, this obstruction must lead to an increase of the velocity around the model. This effect is called solid blockage.

Wake blockage The wake behind a model will also lead to a change in the velocity, as the wake also reduces the effective flow area of the freestream. Since the velocity in the wake is lower than the freestream velocity, it has to lead to an increase of the velocity outside of the wake to satisfy the continuity equation. This effect is called wake blockage. The effects of wake blockage are typically small compared to the other factors when the wake is small, and were therefore neglected.

Streamline curvature The wind tunnel walls obstruct the flow and prevent normal curvature of the streamlines around the wing model. The obstruction leads to an excessive curvature, compared to free flight conditions. The result of a higher curvature of streamlines is an increase in the effective camber of the airfoil. This results in a higher lift, a higher pitching moment about the quarter-chord point, and a higher angle of attack than the airfoil would have in free air conditions [44]. This effect is called streamline curvature.

Buoyancy Buoyancy describes the effects of the growing boundary layer over the test section length. As the boundary layer thickens along the test section walls, the effective area of the freestream jet decreases. This results in a static pressure change along the test section length. This effect can be mitigated with a slightly diverging test section, which counteracts the thickening boundary layer.

The corrected aerodynamic coefficients and the corrected angle of attack were calculated according to Equation 4.4 through Equation 4.6. For details on the derivation of the correction factors, see [3].

$$C_l = K_{C_l} \cdot C_l' \tag{4.4}$$

$$C_d = K_{C_d} \cdot C_d' \tag{4.5}$$

$$\alpha = K_a \cdot \alpha' \tag{4.6}$$

4.4. Wind Tunnel Model

For the wind tunnel measurements, a rectangular wing model with a chord length of 200 mm and a span of 370 mm was manufactured. The wind tunnel model was machined out of a solid block of polyurethane with a 5-axis CNC machine. This allowed for high geometric precision and a stiff wind tunnel model. The surface was gradually polished by hand up to 5000 grit sandpaper, to ensure an aerodynamically smooth surface. Two screw threads were tapped in each side for mounting to the side plates of the wind tunnel. The finished model is displayed in Figure 4.5a. Figure 4.5b shows the wing model mounted inside of the Model Wind Tunnel during transition location measurements.

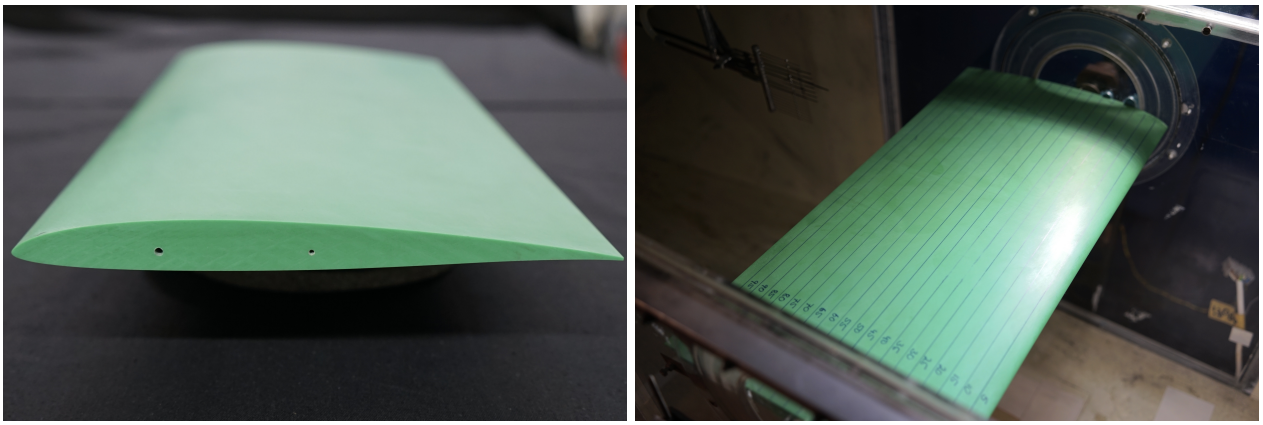

(a) **(b)**

Figure 4.5.: Photographs of the physical wind tunnel model: (a) frontal view of the model and (b) model installed in the wind tunnel test section during experimentation.

4.5. Artificial Ice Shapes

As presented in section 3.2, four different ice shapes were tested in the experimental wind tunnel campaign. The four artificial ice shapes were manufactured out of polyamide 12 with a selective laser sintering (SLS) 3D printer at the Institute of Aircraft Design (IFB) at the University of Stuttgart. The SLS 3D printing method was explicitly favored and chosen over the more common fused deposition modeling (FDM) 3D printing method, because of a superior surface detail quality and accuracy. The SLS 3D printer of the IFB has a minimum layer height of 100 μm, and a working area of 340x340 mm. The artificial ice shapes were produced in two parts because of the size limitation of the working area of the 3D printer. In order to include as much of the ice roughness features in the chordwise direction, the ice shape models from section 3.2 were uniformly scaled up individually before manufacturing. The scaling factors used are given in Table 4.1. The glaze, mixed, and rime (-10°C) ice shapes were manufactured and tested as three-dimensional ice shapes. The rime (-15°C) ice shape was manufactured and tested as a constant cross-section ice shape. For this conversion from three-dimensional to two-dimensional, the Maximum Combined Cross section approach was used. This method is already explained in section 3.2. The manufactured glaze and rime (-15°C) ice shapes are displayed in Figure 4.6. This figure shows the clear difference between the constant cross-section rime (-15°C) ice shape and the three-dimensional glaze ice shape.

Ice Shape	Scaling Factor
Glaze	+10%
Mixed	+15%
Rime (-10°C)	+10%
Rime (-15°C)	+5%

Table 4.1.: Scaling factors of the artificial ice shapes.

The manufactured ice shapes were attached to the leading edge of the wing model using double-sided tape. A wide double-sided tape was used on the leading edge. Additionally, a thin double-sided tape was used for the upper and lower sides of the wing model directly at the chordwise edge of the ice shape. This method of attaching the ice shape to the leading edge resulted in a marginal increase in

the overall ice thickness due to the thickness of the tape. Furthermore, plasticine was used to seal the interfaces between the two artificial ice shape models and the interface of the wind tunnel end plates and the ice shape models fully.

(a) **(b)** **(c)** **(d)**

Figure 4.6.: Comparison of two artificial ice shapes: (a, c) 3D glaze ice shape and (b, d) MCCS rime (-15°C) ice shape.

4.6. Error Analysis

An error analysis is an important part in order to assess the validity and quality of experimental results. Typically, a quantitative uncertainty analysis is done to assess the error made in a measurement. For properly calibrated measurement equipment that is well-suited for the measurement task, the uncertainties of the measurement chain are typically low compared to other external factors, such as the expertise and competence of the technician conducting the experiments. Also, the environmental conditions, such as turbulence intensity, noise, or vibrations, significantly influence the test results of wind tunnel measurements [4]. Therefore, a qualitative approach for evaluating the sources of error was conducted, focusing on typical factors known to influence measurement accuracy. This chapter highlights the factors that were considered in order to mitigate and minimize test result errors.

The first relevant factor is the airflow within the wind tunnel room. Given that the wind tunnel was situated within an industry hall, which was also used for other projects, some level of airflow and air movement was expected. The air should be as still as possible while conducting experiments to minimize change in the ambient conditions. To ensure this, the outside doors were checked to ensure

they were always closed when measurements were conducted.

Temperature, pressure, and humidity stability were also considered throughout the measurements. The expected variations in these parameters for the measurement facility have a negligible effect on the final results. Therefore, the temperature, pressure, and humidity were assumed to be constant for the calculations of the aerodynamic coefficients. Changing conditions would have violated this assumption, and would have resulted in an error. The industry hall was equipped with a temperature control system, and pressure as well as the humidity were observed to remain close to constant throughout individual measurement runs. During the entire measurement campaign, the external conditions (temperature, pressure, and humidity) were recorded and remained sufficiently stable to be considered insignificant to the measurements.

As previously mentioned, the industry hall was shared with other machines and projects. Occasionally, ground shocks or vibrations were observed. Ground shocks and vibrations would influence the force transducer, especially in the calibration process, altering the results. This would lead to systematic errors in following lift measurements. Accordingly, measurements and calibration were avoided in such conditions and repeated if disturbances were observed during experiments or calibration.

As a method to reduce errors and changes in the external conditions, regular calibration was performed. Before each measurement, the lift force and the angle of attack were calibrated. Additionally, all micromanometers were regularly calibrated in order to reduce the impact of changing conditions throughout measurements. Furthermore, the ranges of the micromanometers were adjusted accordingly to ensure measurement accuracy.

It is known that model surface quality and surface contamination influence the aerodynamic results at low Reynolds numbers significantly [44, 53]. Dust particles or other contaminants on the surface act as roughness and can, if large enough, lead to the generation of significant turbulence. The dust particles or other contaminants that settled onto the wing model surface in between measurements were removed with regular cleaning of the wing model surfaces.

4.7. Comparison to Existing Data

Measurements conducted in other facilities can provide a valuable comparison for the results of this study. Three reference measurements with an Eppler E374 airfoil model were performed at the Model Wind Tunnel. The results of these measurements were then compared to existing data in order to validate the measurement methods applied in this thesis. The E374 airfoil model has a chord length of 180 mm, a maximum thickness of 10.9% at 34.3% chord, and a maximum camber of 2% at 38.9% chord. Comparisons of the measured aerodynamic coefficients to existing data from Selig et al. [44] are displayed in Figure 4.7.

The comparisons show good agreement in the Reynolds number regimes Re = 200 000 and Re = 300 000. At Re = 100 000, there are noticeable differences in the drag curve between the results from the Model Wind Tunnel and the measurements of Selig et al. The deviations at this low Reynolds number are not surprising, as freestream conditions in different wind tunnel facilities can influence the low Reynolds number results considerably [38, 43]. Additionally, model surface quality and the model accuracy can affect the results significantly. Overall, the level of agreement between the measurement results of the two facilities is satisfactory.

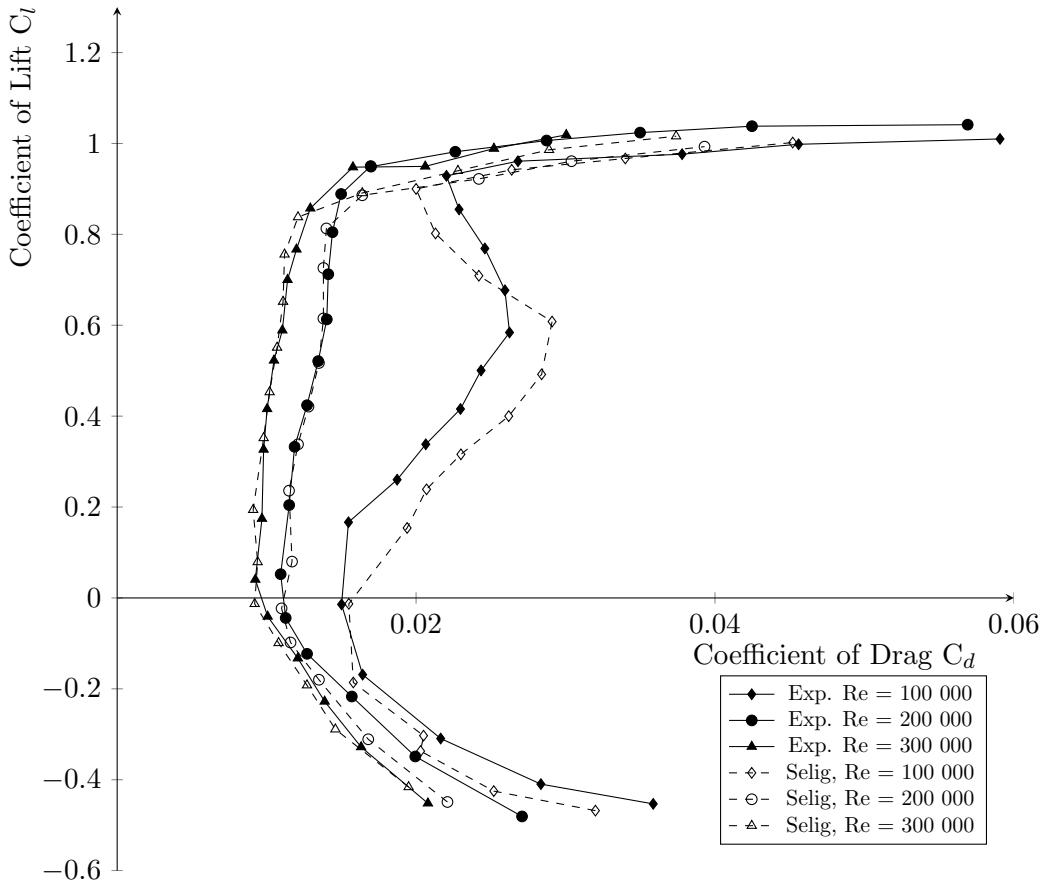

Figure 4.7.: Comparison of experimental data of E374 measurements with existing data of Selig [44].

5. Numerical Methods

For the numerical investigation, the simulation software FENSAP-ICE was used for all simulations. The simulations were performed as two-dimensional steady-state RANS simulations. Different setups were used for the performance simulations of the clean and the iced airfoils. This chapter presents an overview of the numerical methods for the simulations. First, the software and the CFD ice shape models are briefly presented. Then, the simulation setup for the clean airfoil performance simulations is presented. This includes the mesh generation, the mesh dependency study, and the input parameters for FENSAP-ICE. Thereafter, the simulation setup for the iced airfoil simulations is presented, covering the equivalent topics.

5.1. Software

Several software tools were used throughout the numerical part of this thesis. All of the 3D CAD work was conducted in Siemens NX (release 2023). Fidelity Pointwise (version 2023.2.2) was used to generate all meshes used in the simulations. All simulations were performed in Ansys FENSAP-ICE (release 2023 R2). FENSAP is a finite element Navier-Stokes solver with second-order accuracy [6]. It offers different modules designed for the complete analysis of ice accretion and performance penalties [21]. For the current simulations, only the flow calculation module FENSAP was used.

5.2. CFD Ice Shape Models

As a consequence of the two-dimensional simulations, all three-dimensional ice shapes were converted to two-dimensional curves using the MCCS approach described in section 3.2. The resulting MCCS curves of the four ice shapes are displayed in Figure 5.1, where they are normalized by the clean airfoil chord length.

5.3. Clean Airfoil Performance Setup

5.3.1. Mesh Generation for Clean Airfoil Simulation

The mesh for the clean airfoil simulations was created with the commercial meshing software Pointwise. The two-dimensional mesh was built up as an O-type mesh, with structured inflation layers near the airfoil contour and an unstructured mesh as far-field. The far-field diameter was $80 \cdot c = 16$ m and was discretized with 200 points, equally distributed along the diameter. A variable layer number approach was used for the inflation layers, similar to approaches from Fajt [16] and Hann [22]. The height of the initial cells near the wall was chosen to satisfy the condition $y^+ \leq 1$ for the highest simulated Reynolds number of Re = 300 000. For the current inflation layers of the clean airfoil, an initial cell height of $\Delta s = 2.5 \cdot 10^{-6}$ m with a constant growth rate of 1.1 was sufficient to

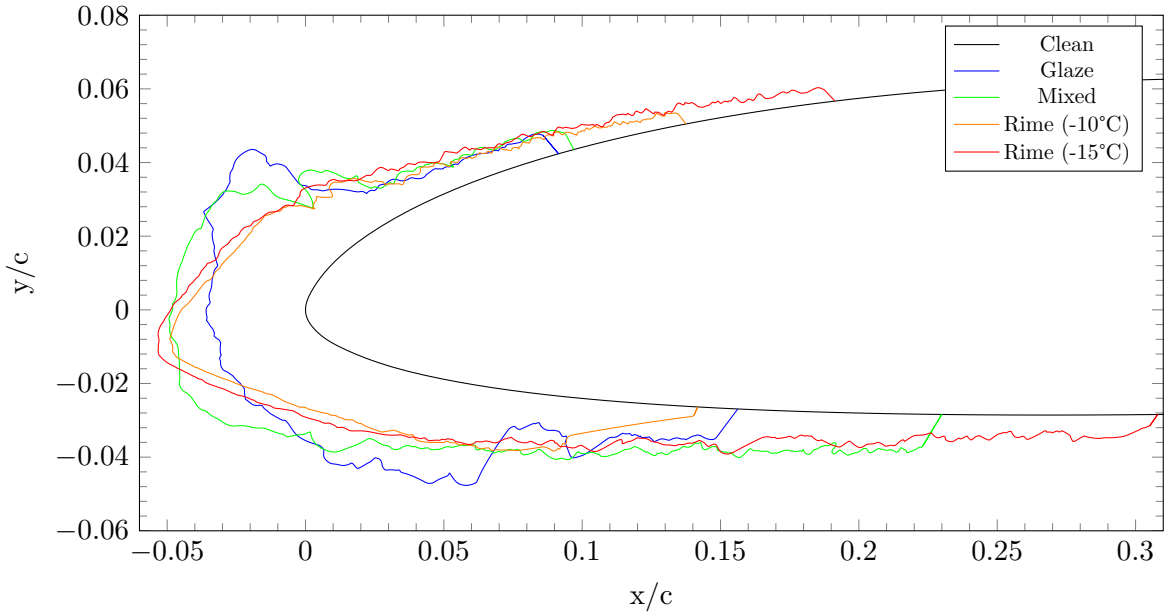

Figure 5.1.: Comparison between the two-dimensional MCCS ice shapes used in the simulations.

satisfy the y^+ condition. The upper and lower sides of the airfoil were discretized with 200 points each. Towards the leading edge and trailing edge, the spacing between points was reduced towards $5.0 \cdot 10^{-5}$ m in order to retain the curvature of the leading edge. The trailing edge was discretized with 15 points, and the spacing between points was decreased towards the upper and lower sides. This resulted in cells with similar edge lengths near the corners. The total number of cells of the clean airfoil performance mesh was approximately 119 000. A detailed view of the clean airfoil mesh is displayed in Figure 5.2. All the relevant mesh settings are summarized in Table 5.1.

Pointwise Settings	**Value**
Mesh dimension	2D
Far-field	O-type grid
Far-field diameter	$80 \cdot c$
Points far-field	200
Points lower/upper side airfoil	200
Points trailing edge	15
Initial cell height	$2.5 \cdot 10^{-6}$
Growth rate of inflation layers	1.1
Number of cells	$\approx$ 119 000

Table 5.1.: Mesh settings for clean airfoil performance meshes.

5.3.2. Mesh Dependency Study of Clean Airfoil

A mesh dependency study was conducted in order to assess the influence of the mesh resolution on the accuracy of the numerical solution. The aim of the mesh dependency study was to evaluate the convergence behavior of the numerical solutions as the mesh is refined, and to evaluate which

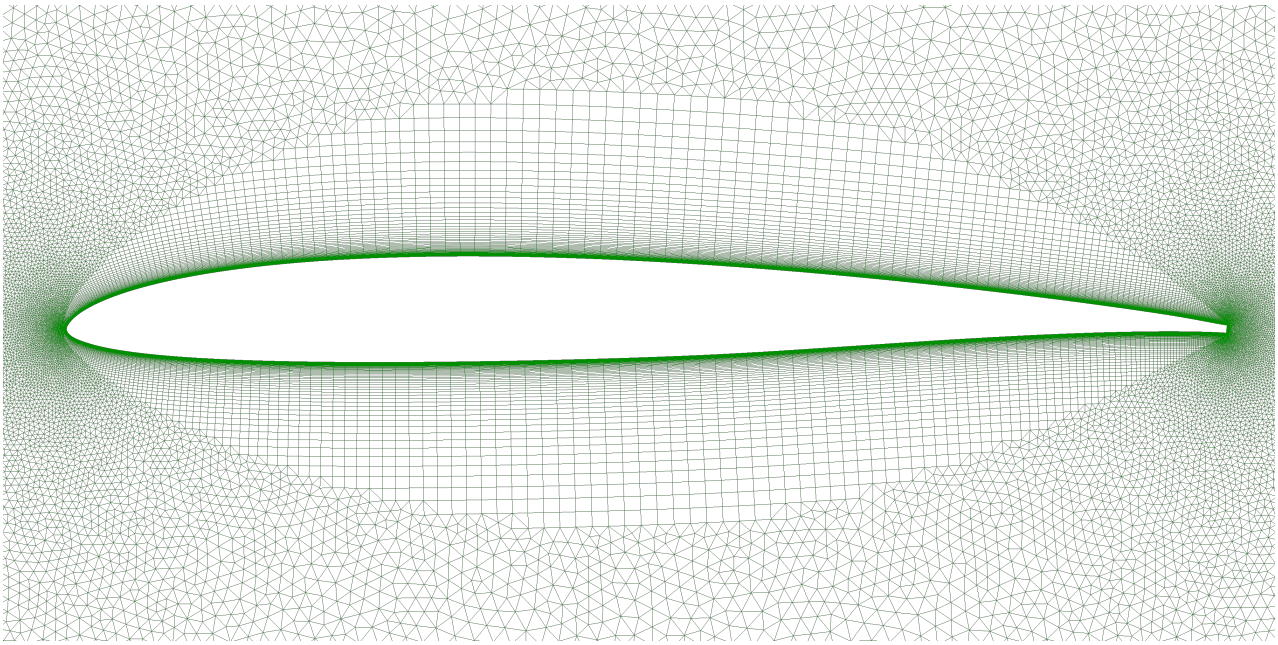

Figure 5.2.: Numerical grid for the clean airfoil performance simulation.

discretization is a good trade off between computational effort needed and accuracy of the solution. For the mesh dependency study, three different meshes with different spatial resolutions were created. The difference in the spatial resolution was achieved by increasing the number of points on the upper and lower sides of the airfoil. The base mesh (A) had a resolution of 100 points each on the upper and lower sides. Mesh (B) and mesh (C) had 200 and 400 points each, respectively, on the upper and lower sides. All other mesh parameters, already described in subsection 5.3.1, were left unchanged for the three meshes. For each mesh, the coefficient of lift and drag at an angle of attack of $\alpha = 0°$ and a Reynolds number of Re = 300 000 was computed. The simulations were run on a Windows 11 based system with an Intel i7-1165G7 processor with four cores and 16 GB of RAM.

In order to evaluate the accuracy of the results, a Richardson extrapolation was conducted. The Richardson extrapolation is only valid if the solution converges monotonously. For the clean airfoil performance simulations both aerodynamic coefficients converged monotonously, and the Richardson extrapolation was applied. The order of convergence was calculated according to Equation 5.1 with f_1, f_2, and f_3, which are the solutions of mesh (A), mesh (B), and mesh (C), respectively.

$$p_{Richardson} = ln(\frac{f_3 - f_2}{f_2 - f_1})/ln(r) \tag{5.1}$$

The Richardson extrapolation was performed using the following equation.

$$Pr_{h=0} = f_3 + \frac{(f_3 - f_2)}{2^r - 1} \tag{5.2}$$

The solutions of the three meshes are displayed in Figure 5.3 normalized by the theoretical true numerical solution of the Richardson extrapolation. For both coefficients, the base mesh (A) deviates just over 0.5% from the extrapolated solution. The medium mesh (B) offers already improvements in terms of accuracy. The finest mesh (C) is as expected the closest to the extrapolated solution with

only marginally deviations to the extrapolated value. The better accuracy comes with the drawback of higher computational power requirements. The required computational power for calculating 5000 time steps in terms of CPU hours were 0.73, 1.10 and 1.71 for the mesh (A), mesh (B), and mesh (C). The converging behavior was similar for all three meshes. With respect to the accuracy and the required computational power, mesh (B) was chosen for all further simulations, as it offered an accurate solution with acceptable computational power requirements.

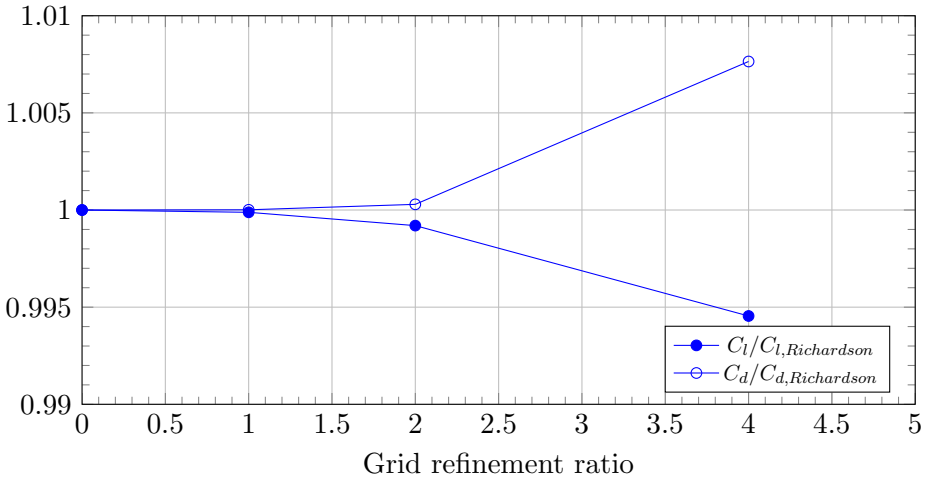

Figure 5.3.: Mesh dependency study of clean airfoil at $\alpha = 0°$ and Re = 300 000.

5.3.3. CFD Input Parameters for Clean Airfoil Simulations

In this section the input parameters for the clean airfoil performance simulations are presented. The clean airfoil simulations were all run with the k–ω SST turbulence model. The k–ω SST model is introduced in subsection 2.3.2. For the boundary layer transition, the intermittency based model which is implemented in FENSAP-ICE was used. This transition model uses a one-equation local correlation-based intermittency transition model [6]. The predicted laminar-turbulent transition of the clean airfoil was predicted within reasonable accuracy, as comparisons to experimental transition location measurements showed. The surface roughness was set to zero, as the model is assumed to be aerodynamically smooth. For the static temperature and static pressure, standard atmospheric conditions according to the International Civil Aviation Organization (ICAO) [27] were assumed. All settings and parameters for the clean simulations are summarized in Table 5.2 and Table 5.3.

FENSAP-ICE Settings	**Value**
Turbulence model	k–ω SST
Transition	Intermittency (natural transition)
Artificial viscosity	Second order streamline upwind scheme and cross-wind dissipation $1 \cdot 10^{-7}$
Surface roughness	No roughness
CFL number	300
Max. number of time steps	5000

Table 5.2.: FENSAP-ICE settings for clean airfoil simulations.

FENSAP-ICE Input Parameters	Value
Chord length c	0.20 m
Reynolds number Re	[100 000, 200 000, 300 000]
Static pressure p	101 325 Pa
Air temperature T	293.15 K
Angles of attack α	$-6°$–$16°$

Table 5.3.: FENSAP-ICE input parameters for clean airfoil simulations.

5.4. Iced Airfoil Performance Setup

5.4.1. Mesh Generation for Iced Airfoil Simulations

The meshes for the iced airfoil simulations were created in a similar manner to the clean airfoil mesh explained in subsection 5.3.1. The mesh was also created as an O-type mesh with an unstructured far-field with a diameter of $80 \cdot c = 16$ m and a structured inflation layer with a variable number of cells. The condition of $y^+ \leq 1$ was also set for the iced airfoil simulations. The initial cell height of the inflation layer was decreased to $\Delta s = 1.25 \cdot 10^{-6}$ m, compared to the clean airfoil due to a higher velocity around the leading edge. For the discretization of the upper and lower side of the clean airfoil, the 200 points, that were used in the clean case, were reduced relative to the clean airfoil surface (i.e. the airfoil surface that is not covered by the ice shape). For the ice shape at the leading edge, a constant spacing of approximately $100\mu m$ was used in order to capture all relevant roughness features of the ice shapes. In order to have a good transition between the clean airfoil and the ice shape, the spacing between points on the upper and lower sides was reduced towards $100\mu m$. The spacing between points towards the leading edge was set to $5 \cdot 10^{-5}$ m. The blunt trailing edge had the same discretization of 15 points as the clean airfoil. The mesh of the glaze ice shape can be seen in Figure 5.4. The total cell count of the iced airfoil meshes depended heavily on the ice shape due to the high resolution of the leading edge. The meshes for the glaze, mixed, rime (-10°C), and rime (-15°C) ice shapes respectively had approximately 210 000, 224 000, 214 000, and 229 000 number of cells. The settings for the iced airfoil meshes are summarized in Table 5.4.

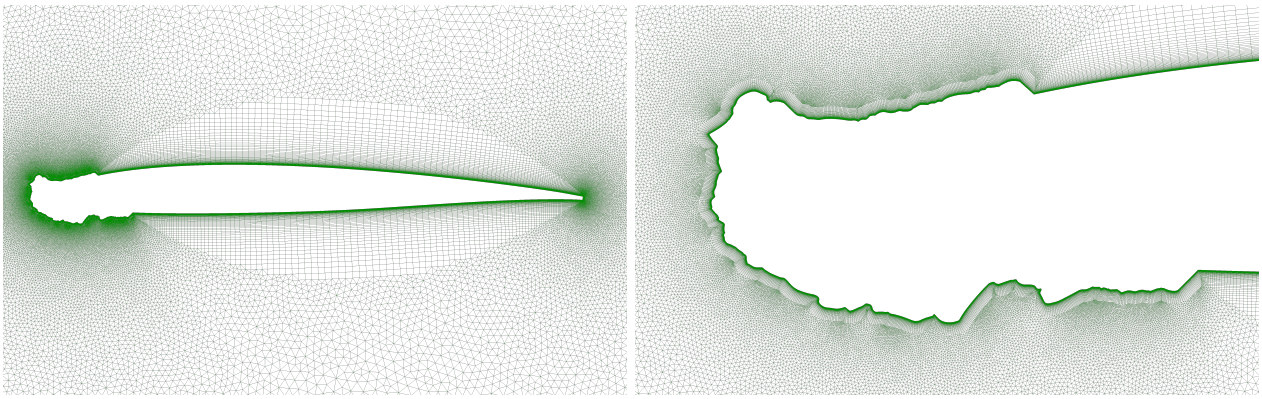

(a) **(b)**

Figure 5.4.: Image of the glaze ice performance mesh: (a) mesh with variable number inflation layers and (b) detailed view of leading edge mesh.

Pointwise Settings	Value
Mesh dimension	2D
Far-field	O-type grid
Far-field diameter	$80 \cdot c$
Points far-field	200
Points lower/upper side airfoil	$200 \cdot (0.2 - x_{ice})$
Constant point spacing ice	$100\mu m$
Points trailing edge	15
Initial cell height	$1.25 \cdot 10^{-6}$ m
Growth rate of inflation layers	1.1
Cells (glaze/ mixed/ rime (-10°C)/ rime (-15°C))	$\approx$ 210 000/ 224 000/ 214 000/ 229 000

Table 5.4.: Pointwise settings for iced airfoil performance meshes.

5.4.2. Mesh Dependency Study of Iced Airfoil

In order to assess the meshes for the iced airfoils, another mesh dependency study was conducted. For this, the convergence behavior and the computational effort was investigated with four different meshes of the glaze ice shape. The glaze ice shape was chosen for the mesh dependency study, since it had the most complex geometry of the different ice shapes. As for the clean airfoil mesh dependency study, a mesh (A) was created as the baseline mesh of the mesh dependency study. The baseline mesh (A) had a discretization of the leading edge ice of a point spacing of $200\mu m$. The point spacing was halved with each refinement for the three finer meshes. The clean airfoil- and far-field discretization was kept constant for all meshes. For the four meshes, the coefficient of lift and drag were computed with the same system as mentioned above. The coefficients were computed at an angle of attack of $\alpha = 0°$ and Re = 300 000. To assess the accuracy of the solutions, a Richardson extrapolation was performed for both coefficients. Figure 5.5 presents the coefficients normalized by the extrapolated solutions.

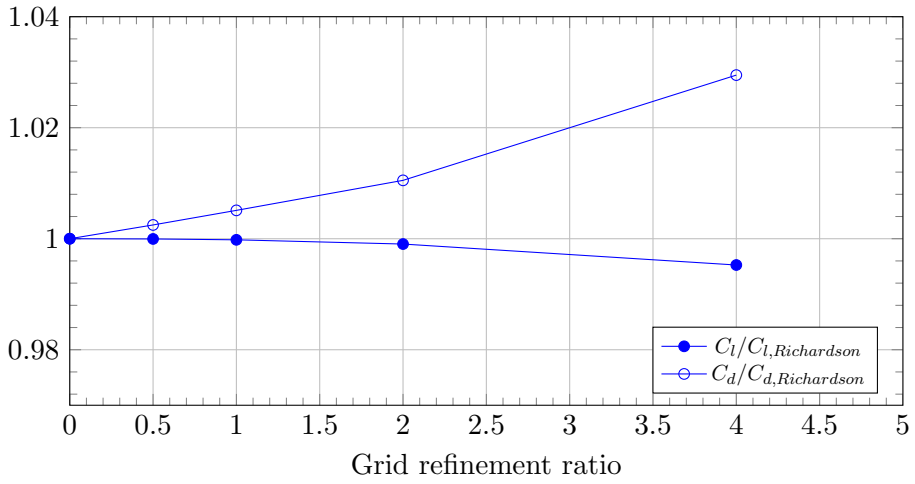

Figure 5.5.: Mesh dependency study of glaze ice shape at $\alpha = 0°$ and Re = 300 000.

Both coefficients converged monotonously towards the extrapolated solution, resulting in increased accuracy with higher mesh resolution. The required computational power for calculating 5000 time

steps in terms of CPU hours were 1.44, 1.93, 2.71, and 4.25 for mesh (A), mesh (B), mesh (C), and mesh (D). As a trade off between solution accuracy and required computational effort, mesh (B) with a constant point spacing of $100\mu m$ of the leading edge ice was chosen for all further simulations.

5.4.3. CFD Input Parameters for Iced Airfoil Simulations

The input parameters for the iced airfoil performance simulations are mostly similar to the clean airfoil simulation input parameters. As for the clean airfoil simulations, the k–ω SST turbulence model was used. However, instead of using the intermittency based transition model, a fully turbulent flow is assumed, since the ice shape geometry is expected to trigger a laminar-turbulent transition of the boundary layer [10]. The surface roughness of the ice shape surface was set to the resolution of the SLS 3D printing process, specified at 100 μm. The remaining clean airfoil was set to a roughness of zero. As for the clean airfoil simulations, standard atmospheric conditions were assumed. For the determination of the aerodynamic coefficients, the clean airfoil chord length was used. All settings and parameters for the iced airfoil performance simulations are summarized in Table 5.5 and Table 5.6.

FENSAP-ICE Settings	**Value**
Turbulence model	k–ω SST
Boundary layer flow	No transition (fully turbulent)
Artificial viscosity	Second order streamline upwind scheme and cross-wind dissipation $1 \cdot 10^{-7}$
Surface roughness	Sand grain roughness on ice, no roughness on airfoil
CFL number	300
Max. number of time steps	5000

Table 5.5.: FENSAP-ICE settings for clean airfoil simulations.

FENSAP-ICE settings for iced airfoil simulations	**Value**
Chord length c	0.20 m
Reynolds number Re	[100 000, 200 000, 300 000]
Static pressure p	101 325 Pa
Air temperature T	293.15 K
Angles of attack α	$-6°$–$16°$
Ice roughness	100 μm

Table 5.6.: FENSAP-ICE input parameters for iced airfoil simulations.

6. Results and Validation

This chapter presents a thorough review and discussion of the experimental and numerical results obtained throughout the experimental and numerical studies. First, the experimental results are presented for each Reynolds number regime. The performance degradation will be considered as ΔC_l and ΔC_d at an angle of $\alpha = +4°$, since this is a typical angle of attack for straight and level flight [16]. The numerical results of each leading edge geometry are presented and compared to the experimental results. The final part of this chapter is a discussion of the results and the features or effects observed. In addition to this chapter, a full overview of the experimental data can be found in Appendix B.

6.1. Experimental Results

6.1.1. Experimental Results at Re = 100 000

The experimental results of the Reynolds number regime of Re = 100 000 are displayed in Figure 6.1. The results of the clean RG-15 airfoil showed a baseline performance of $C_l = 0.637$ and $C_d = 0.0150$ at a typical cruise flight angle of attack of $\alpha = +4°$. A laminar bucket was clearly prominent from proximately $C_l = -0.16$ to $C_l = 0.90$. Furthermore, an untypical increase in drag was visible in the range $0° \leq \alpha \leq 3°$, which could be an indication of a local laminar separation bubble. This matched well with the experimental data of Selig et al. [44], although a small deviation to the existing data in the size and position of the drag increase was noticeable. Near the stall region, an unusual behavior was observed, as the lift curve began to flatten at $\alpha = +8°$, suggesting an onset of stall. Then, however, exhibited an increase up until $\alpha = +11°$ with $C_{l,max} = 1.08$. Increasing the angle of attack above this, an abrupt decrease of the coefficient of lift was visible, indicating relatively hard stall characteristics. This was also in good agreement with the findings of Selig et al. [44].

The glaze ice shape showed the largest performance penalties of the four ice shapes for Re = 100 000. At $\alpha = +4°$ the coefficient of lift was reduced by $\Delta C_l = -10\%$, while the coefficient of drag increased with $\Delta C_d = +289\%$. The stall angle was reduced to $\alpha = +8°$, with a reduction of $\Delta C_{l,max} = -8\%$ and an increase of $\Delta C_d = +378\%$. The highest performance penalty in the form of a drag increase was observed at $\alpha = +7°$ with an increase of drag of approximately $\Delta C_d = +406\%$. At this point, the flow of the glaze ice was already stalled, while the clean airfoil still performed slightly above its laminar bucket.

The mixed ice shape showed smaller performance degradation at $\alpha = +4°$ compared to glaze ice. At this angle, lift decreased with $\Delta C_l = -9\%$, while drag increased with $\Delta C_d = +168\%$. The stall angle for the mixed ice shape was delayed to $\alpha = +13°$. The maximum coefficient of lift was decreased with $\Delta C_{l,max} = -3.6\%$. The lift curve was flattening at high angles of attack, creating a plateau-like shape, which caused the late stall angle. An increase above the stall angle was followed by a very rapid decrease of lift. This indicates a very aggressive stall behavior for the mixed iced shape.

The two rime ice shapes induced the least performance penalties. At $\alpha = +4°$ the lift reduction

and drag increase were $\Delta C_l = -10\%$ with $\Delta C_d = +89\%$ and $\Delta C_l = -8\%$ with $\Delta C_d = +31\%$ for the rime (-10°C) and rime (-15°C) ice shapes respectively. The maximum coefficient of lift increased for both rime ice shapes, compared to the clean airfoil, with approximately the same increase of $\Delta C_{l,max} = +10\%$. The mechanisms of this unexpected rise of the maximum lift will be discussed in detail in section 6.3. The stall angle of the rime (-10°C) ice shape was delayed to $\alpha = +13°$. In the stall region, an unusual behavior was observed, which appears to be similar to the behavior observed of the clean airfoil. The lift curve flattens, before rising to higher coefficients of lift, creating an indent in the lift curve. This will also be discussed in section 6.3. The rime (-15°C) ice shape did not have such a feature. The lift curve is nearly linear up until the stall region, with a stall angle of $\alpha = +12°$. However, another interesting feature was observed in the drag curve of the rime (-15°C) ice shape. In the range $0.048 \leq C_l \leq 0.590$, the drag is nearly as low as for the clean airfoil, with $\Delta C_d = +8$–10% at $\alpha = +1°$–$2°$. This third feature will also be considered in detail in section 6.3.

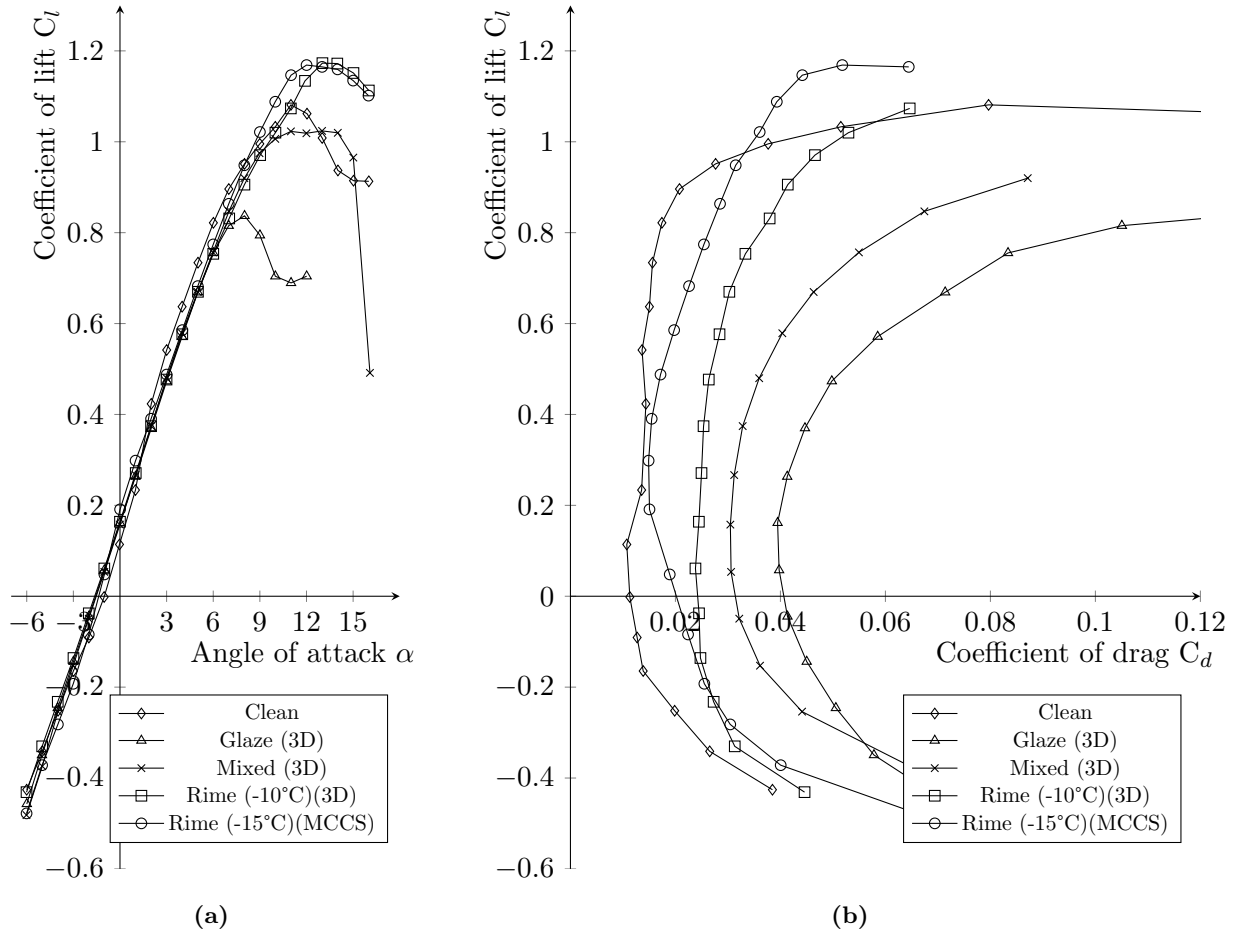

Figure 6.1.: Comparison of the experimental data at Re = 100 000.

6.1.2. Experimental Results at Re = 200 000

For the Reynolds number regime of Re = 200 000, the experimental results are presented in Figure 6.2. The clean airfoil at this Reynolds number regime had a better performance at $\alpha = +4°$ with $C_l = 0.637$ and $C_d = 0.0109$. A contribution to the better performance was a reduction of the laminar separation bubble, which was mentioned above. The drag curve only had a minimal local increase

at $\alpha = 0°$, as an indication for a minor laminar separation bubble. The unusual behavior observed near the stall region at Re = 100 000 was still visible but less distinctive. Stall appeared to occur at approximately $\alpha = +11°$ with a $C_{l,max} = 1.093$. The stall characteristics were less aggressive compared to the lift curve at Re = 100 000. Furthermore, drag decreased at all angles of attack, as expected for higher Reynolds numbers [33].

The glaze ice shape induced again the highest performance penalties of the four different ice shapes. At $\alpha = +4°$, the performance decreased with $\Delta C_l = -8\%$ and $\Delta C_d = +415\%$. The stall angle was decreased to $\alpha = +8°$, while the maximum achievable lift was reduced with $\Delta C_{l,max} = -21\%$. The stall behavior was slightly less aggressive than at Re = 100 000, with a more gradual decrease of lift when increasing the angle of attack beyond the stall angle. For negative lift, the drag curve was almost coincident with the drag curve at Re = 100 000. At positive lift, drag was marginally lower than for Re = 100 000, suggesting a reduction of the Reynolds number dependency on the coefficient of drag, as seen for the clean airfoil.

For the mixed ice shape, the performance penalties were smaller than for the glaze ice shape. Lift decreased with $\Delta C_l = -8\%$ and drag increased with $\Delta C_d = +264\%$ at $\alpha = +4°$. The lift curve exhibited a plateau-like shape near the stall region similarly to the lift curve at Re = 100 000. The stall angle was increased to $\alpha = +15$ and the maximum coefficient of lift was reduced by $\Delta C_{l,max} = -2\%$. The stall characteristics at this Reynolds number regimes cannot be determined since the stall was not fully captured within the maximum measured angle of attack of $\alpha = +16°$. However, one could assume that the stall behavior is similar to characteristics at Re = 100 000, as the stall behavior typically does not change significantly for iced airfoils [22]. The drag curve had a similar shape and size to the drag curve at Re = 100 000, was however shifted to lower drag values.

Similar to the lower Reynolds number case, the two rime ice shapes caused the lowest performance penalties. The rime (-10°C) ice shape induced a lift reduction of $\Delta C_l = -9\%$ and a drag increase of $\Delta C_d = +158\%$, while the rime (-15°C) ice shape decreased lift by $\Delta C_l = -6\%$ and increased drag by $\Delta C_d = +131\%$ at $\alpha = +4°$. The drag curves of both rime ice shapes overlapped at negative lift and diverged with increasing lift. It can be observed that the drag of the rime (-15°C) ice shape barely changed over positive coefficients of lift up until the stall region, while the drag of the rime (-10°C) shape considerably increased over the same range of angles of attack. In the stall region, the same unusual behavior described above occurred for the rime (-10°C) ice shape. At this Reynolds number regime, the behavior was even more distinct. The stall of the rime (-10°C) ice shape was also delayed beyond $\alpha = +16°$, while the stall angle of the rime (-15°C) ice shape was identical to the stall angle of the clean airfoil. The rime (-10°C) ice shape achieved higher maximum lift than the rime (-15°C) ice shape. However, both ice shapes increased the maximum coefficient of lift from the clean airfoil. The coefficient of lift increased with $\Delta C_{l,max} = +10\%$ and $\Delta C_{l,max} = +5\%$ for the rime (-10°C) and rime (-15°C) ice shapes. The stall behavior of the rime (-15°C) ice shape was soft since lift was gradually decreased with increasing angles of attack. The drag curve of the rime (-15°C) ice shape showed an increase of drag at this Reynolds number compared to Re = 100 000. This was not expected, as the center drag levels typically reduce with increasing Reynolds numbers [33].

6.1.3. Experimental Results at Re = 300 000

The results of the Reynolds number regime of Re = 300 000 are presented in this section. The lift and drag curves for this Reynolds number regime are shown in Figure 6.3. The clean airfoil showed a baseline performance of $C_l = 0.650$ and $C_d = 0.00958$ for $\alpha = +4°$. The lift curve showed a maximum achievable lift of $C_{l,max} = 1.11$ at $\alpha = +12°$. The stall was less aggressive than for Re = 200 000

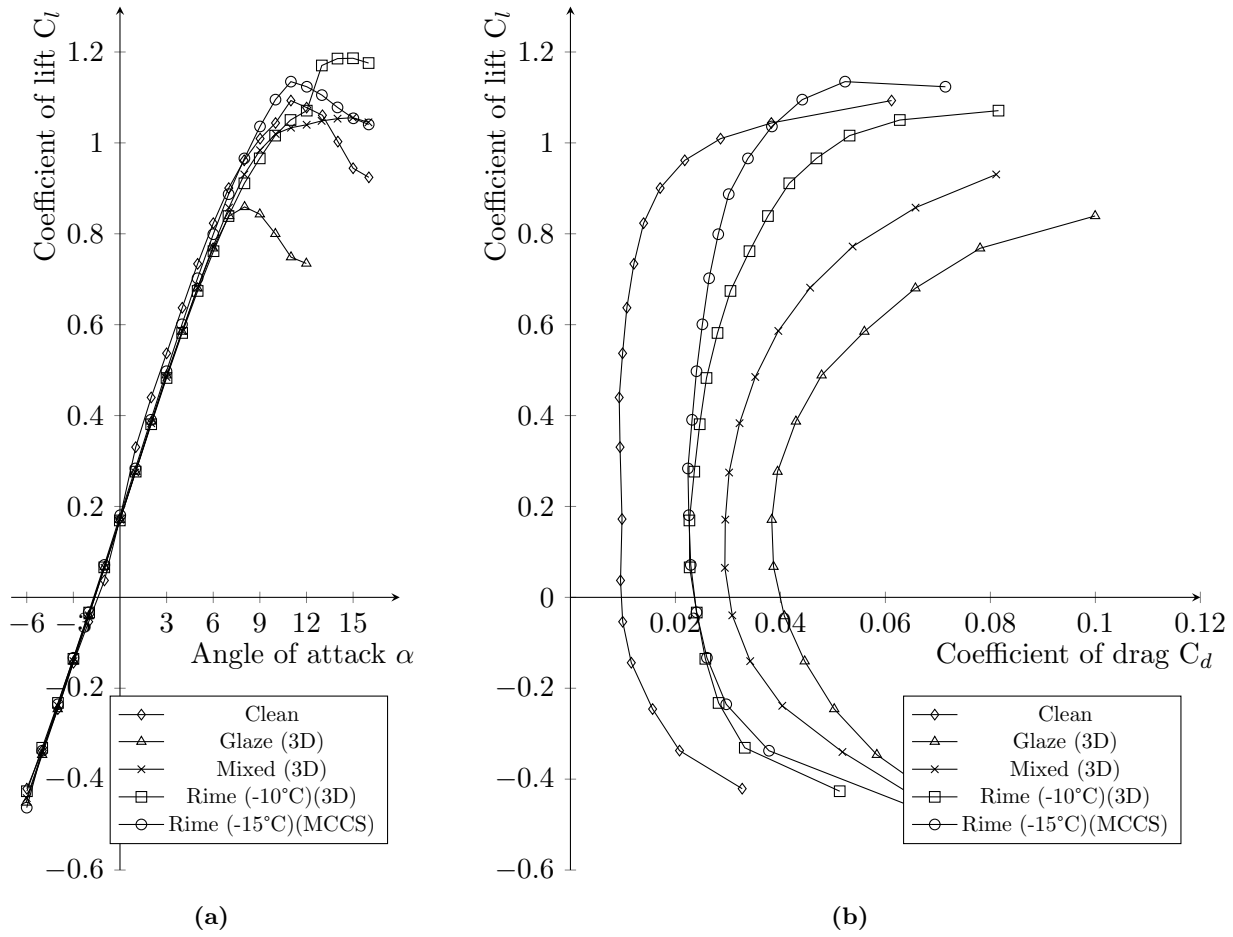

Figure 6.2.: Comparison of the experimental data at Re = 200 000

and Re = 100 000. Furthermore, the unusual behavior near stall, that was observed for both lower Reynolds number regimes, was no longer visible. The lift curve of this Reynolds number regime had a linear section, which lead right into the stall region. The stall angle was increased to $\alpha \approx +13°$. The drag was the lowest across all three Reynolds numbers. The shape of the drag curve shifted moderately into a more rounded shape, which had the effect of reducing the width of the laminar bucket. This decrease of the width of the laminar bucket was only marginal, but observable.

For the glaze ice shape the performance penalties were again the highest of all ice shapes, with $\Delta C_l = -8\%$ and $\Delta C_d = +483\%$ at $\alpha = +4°$. This was also the highest performance degradation across all Reynolds number regimes. Stall occurred already at $\alpha = +8°$ with an unchanged stall behavior compared to Re = 200 000. Furthermore, the reduction of the maximum achievable coefficient of lift was $\Delta C_{l,max} = -22\%$. The drag curve can be observed to be overlapping with the drag curve of Re = 200 000. A possible explanation for this is an identical separation point induced by the ice shape for both Reynolds number regimes. This will part of the discussion in section 6.3.

The mixed ice shape had a performance degradation of $\Delta C_l = -9\%$ and $\Delta C_d = +307\%$ at an angle of attack of $\alpha = +4°$. From the lift curve, the same plateau-like shape, as explained for Re = 200 000, was observed. The stall angle of the mixed ice shape at Re = 300 000 was $\alpha = +14°$. The maximum coefficient of lift was reduced by $\Delta C_{l,max} = -4\%$ compared to the clean case. The drag curve of the mixed ice shape at Re = 300 000 was almost coincident with the drag curve at Re =

200 000. This behavior of the drag curves was similar to what was also discovered for the glaze ice shape.

The rime ice shapes experienced the least performance penalties of the four ice shapes, as for the previous Reynolds number regimes. At $\alpha = +4°$ lift decreased with $\Delta C_l = -8/-4\%$ and drag increased with $\Delta C_d = +191/+160\%$ for the rime (-10°C) and rime (-15°) ice shapes. Both rime ice shapes increased the maximum coefficient of lift compared to the clean airfoil. The stall region differed again for the two different rime ice shapes. The rime (-10°C) had the same behavior as described for Re = 200 000, but less distinctive. However, at this Reynolds number, no stall was reached within the maximum angle of attack of $\alpha = +16°$. The lift curve flattened but rose until this angle was reached. Therefore, the maximum coefficient of lift could not be defined for this ice shape. However, the coefficient of lift at $\alpha = +16°$ is $C_l = 1.23$, which was 11% higher than the maximum coefficient of lift for the clean airfoil. The rime (-15°C) ice shape had a stall angle of $\alpha = +11°$, which was earlier than for the clean airfoil. The maximum coefficient of lift for this ice shape increased with $\Delta C_{l,max} = +6\%$ compared to the clean airfoil. The stall behavior for the rime (-15°C) was observed to be more aggressive than at Re = 200 000. The drag curves showed a similar behavior as for Re = 200 000. At low lift values, the drag curves of both rime ice shapes appeared to overlap. With increasing lift, the drag curves diverged, with the rime (-10°C) ice shape having a larger increase in drag than the rime (-15°C).

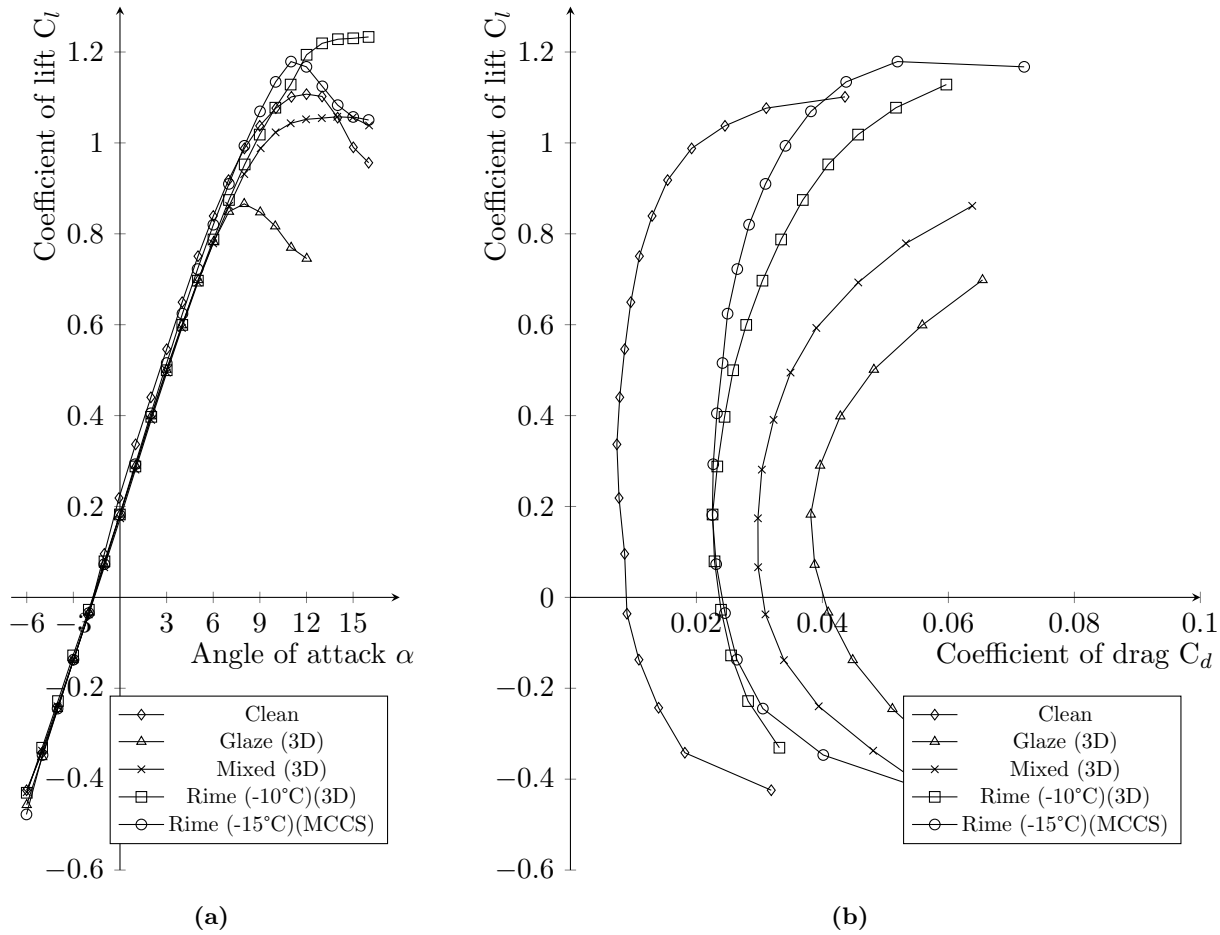

Figure 6.3.: Comparison of the experimental data at Re = 300 000

6.2. Numerical Results and Validation

6.2.1. Clean Airfoil Results

This section presents the simulation results of the clean airfoil of all three Reynolds number regimes. Figure 6.4 shows the comparison of the simulation and the experimental results for the clean airfoil. The results show good agreement between the simulation and experimental results in the linear section of the lift curve at all three Reynolds number regimes. The biggest difference in this section was observed near the laminar separation bubble at Re = 100 000. In addition to this, deviations between the simulations and experimental results were discovered in the stall region. The simulations generally predicted an earlier stall with a lower maximum coefficient of lift than the experiments. The drag was captured well for the Reynolds number regimes Re = 200 000 and Re = 300 000, only with minor differences to the experimental data. The simulations however underestimated the drag of the lowest Reynolds number regime of Re = 100 000. The drag curve shows that the laminar separation region was predicted by the simulations, as there is a local region of drag increase. However, the size, position, and the magnitude of the drag increase of the laminar separation bubble differed compared to the experimental data. Furthermore, the CFD simulations did not converge within the maximum number of iterations for high angles of attack. As a consequence, simulation results were limited up to $\alpha = +11°$ for the Reynolds numbers of Re = 300 000 and Re = 200 000, and $\alpha = +10°$ for Re = 100 000.

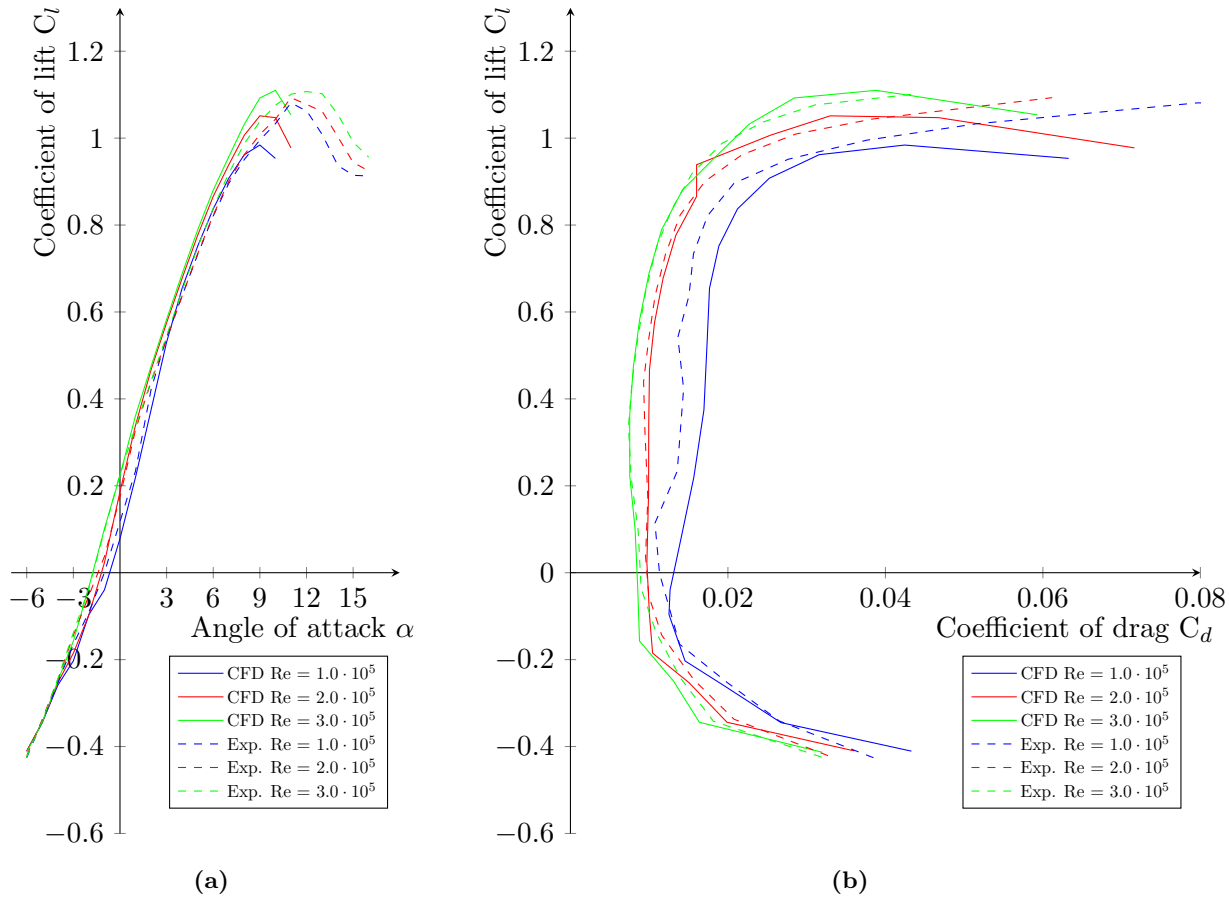

Figure 6.4.: Comparison between experimental and simulation results of clean airfoil.

6.2.2. Glaze Ice Results

The simulation and experimental results for the glaze ice shape are compared in Figure 6.5. The linear section of the lift curve was captured to a great extent by the simulations. Approximately up until $C_l = 0.5$, the lift curves of the simulations were marginally offset to lower angles of attack compared to the experimental data. Thereafter, the deviation to the experimental lift curve increased. The simulation results exhibited a common maximum coefficient of lift of $C_{l,max} = 0.63$ for the three Reynolds number regimes. This common maximum coefficient of lift was predicted at an earlier angle of attack by the simulations. As expected, the stall was also predicted earlier by approximately 2°. The stall behavior differed, as the simulations suggested a more gradual stall. Furthermore, the drag in the center of the drag curve was estimated to be significantly lower than the experimental data indicated. At $\alpha = 0°$, drag was lower with $\Delta C_d = -18\%$ to -22%. As the drag levels and the maximum coefficient of lift were lower for the simulations than the experimental data, the upper and lower sides of the drag curves were more pronounced. The simulations of the glaze ice shape also struggled to converge at high angles of attack. For the three Reynolds number regimes, angles of attack greater than $\alpha = +9°$, did not converge sufficiently within the defined maximum time steps.

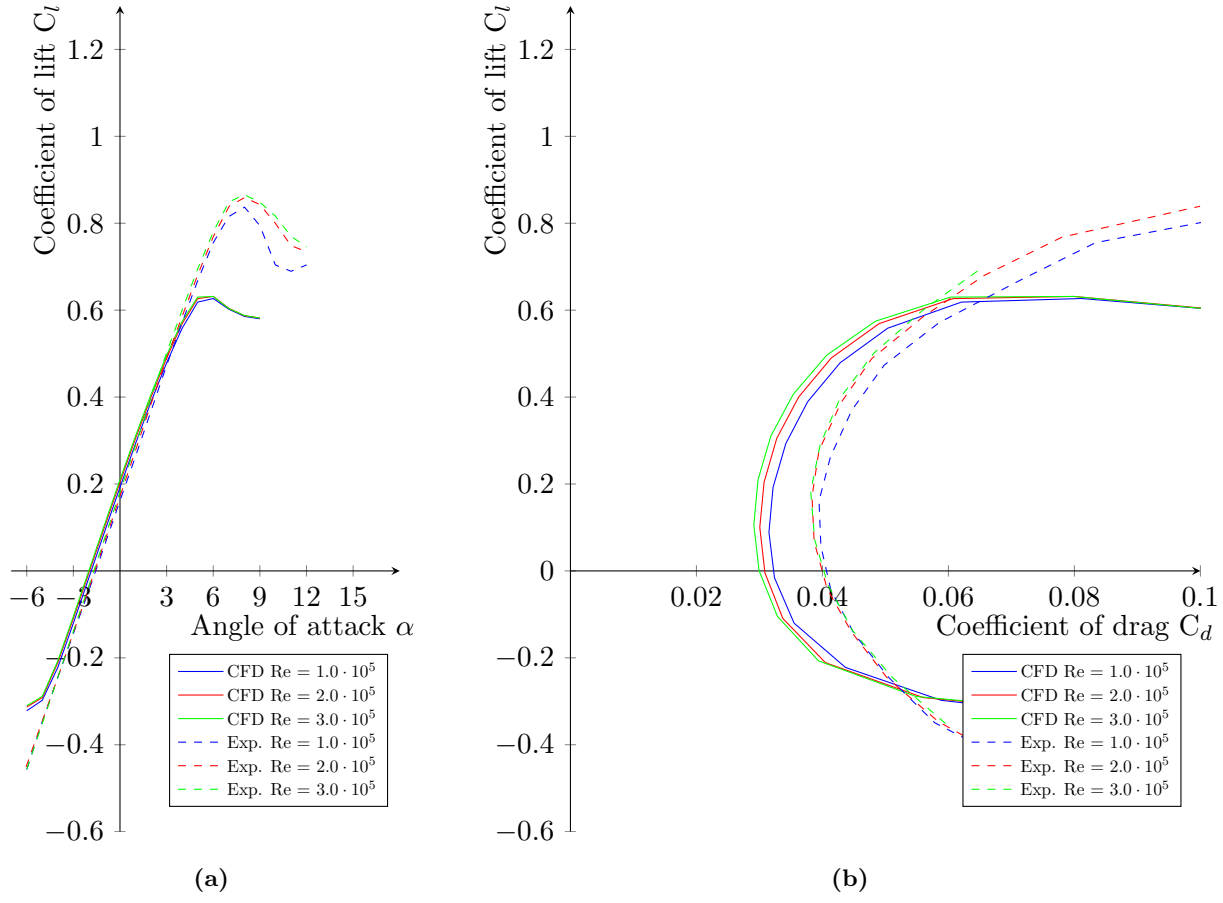

Figure 6.5.: Comparison between experimental and simulation results of the glaze ice shape.

6.2.3. Mixed Ice Results

The simulation results of the mixed ice shape had similar characteristics to the simulation results of the glaze ice shape. The comparison between the simulation and experimental results of the mixed ice shape is displayed in Figure 6.6. The linear lift section showed good agreement between simulation and experimental data until $C_l \approx 0.65$. Increasing the lift beyond this, resulted in greater deviations between the simulation and experimental results. The simulations predicted a maximum coefficient of lift of $C_{l,max} = 0.71$–0.73 for three Reynolds number regimes. The maximum coefficient of lift was predicted at lower angles of attack, similarly as for the glaze ice shape. However, with a significantly larger deviation of $\Delta\alpha = 7$–$9°$. A difference in the stall behavior between the simulation and experimental data was observed. Stall was, as for the glaze ice shape, predicted as a gradual decrease of lift, contrary to the very aggressive stall behavior that the experimental data exhibited. Drag levels were estimated to be considerably lower compared to the experimental data. The drag at $\alpha = 0°$ was under-estimated with $\Delta C_d = -21\%$ to -28%. The drag curve showed a shift of better performance to lower angles of attack. For Re = 300 000 and Re = 200 000, the simulations had no problems converging at high angles of attack. The simulations were stopped after $\alpha = +12°$, since stall occurred earlier, and the higher angles of attack were regarded as insignificant for the investigation. At Re = 100 000, convergence was not reached within the time step limit above $\alpha = +9°$.

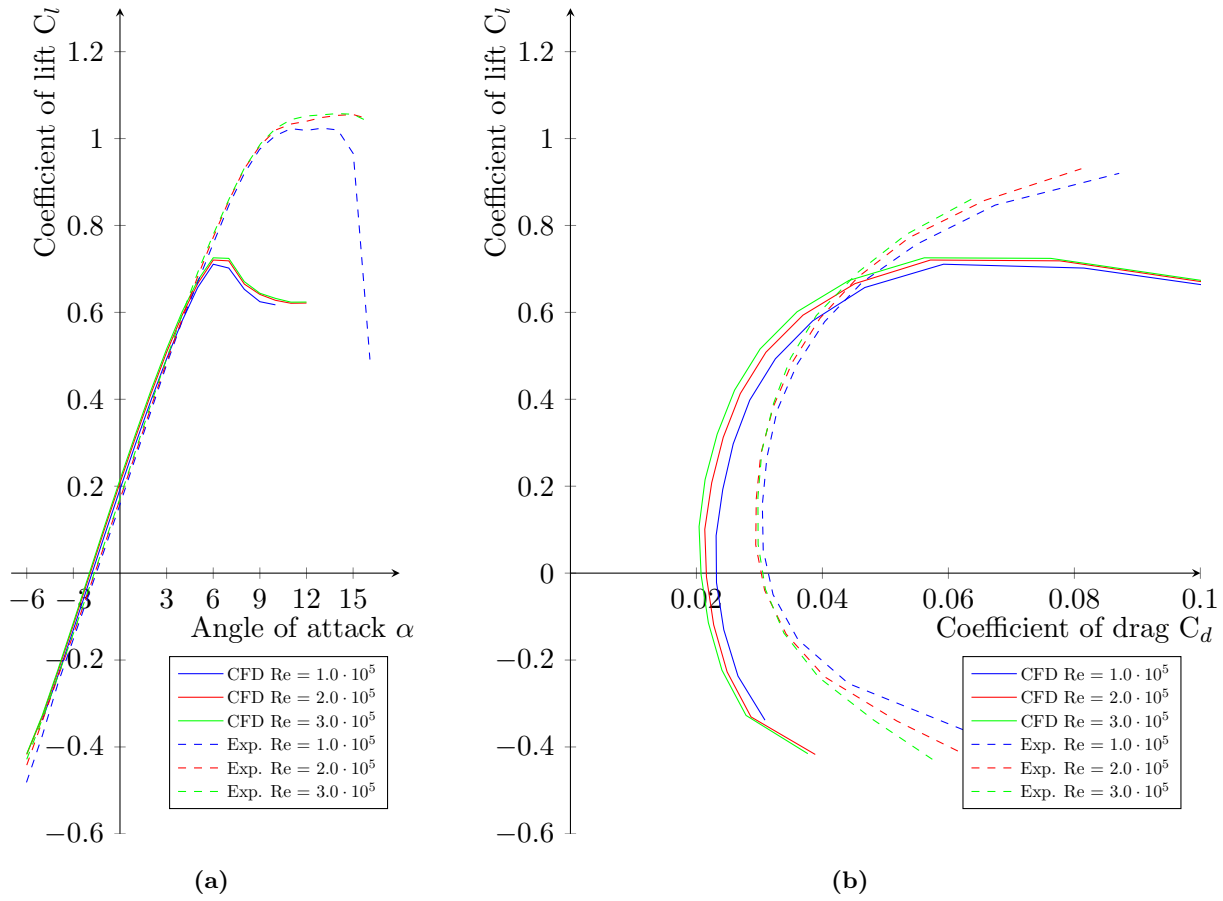

Figure 6.6.: Comparison between experimental and simulation results of the mixed ice shape.

6.2.4. Rime Ice (-10°C) Results

For the rime (-10°C) ice shape, the simulation results showed better agreement of the drag than the glaze and mixed ice shapes. Agreement of the lift curve was, however, worse than that of the two cases above. The linear section of the lift curve showed a minor difference in the gradient compared to the experimental data. The magnitude of the difference was most significant for Re = 100 000 and Re = 200 000. The maximum coefficient of lift was predicted at $\alpha = +11°$ with $C_{l,max} = 1.10$–1.12 for the three Reynolds number regimes. There were significant differences between the simulation and the experimental results in the stall region. The simulation results showed no sign of the unusual stall behavior of the experimental data, which was explained in section 6.1. Additionally, Figure 6.7 showed a very aggressive stall behavior, with a rapid loss of lift, for all three Reynolds number regimes, which differed from the more gradual stall behavior that the experimental data exhibited. The drag curves showed better agreement with the experimental data. The drag at $\alpha = 0°$ was predicted to be $\Delta C_d = -16\%$ to -19% lower than the experimental drag. The overall shape of the drag curves of the simulations displayed similarities in position and shape with the experimental drag curves. For the rime (-10°C) simulations, angles of attack greater than $\alpha = +14°$ were not computed. Convergence was reached within the time step limit for all three Reynolds number regimes and all angles of attack.

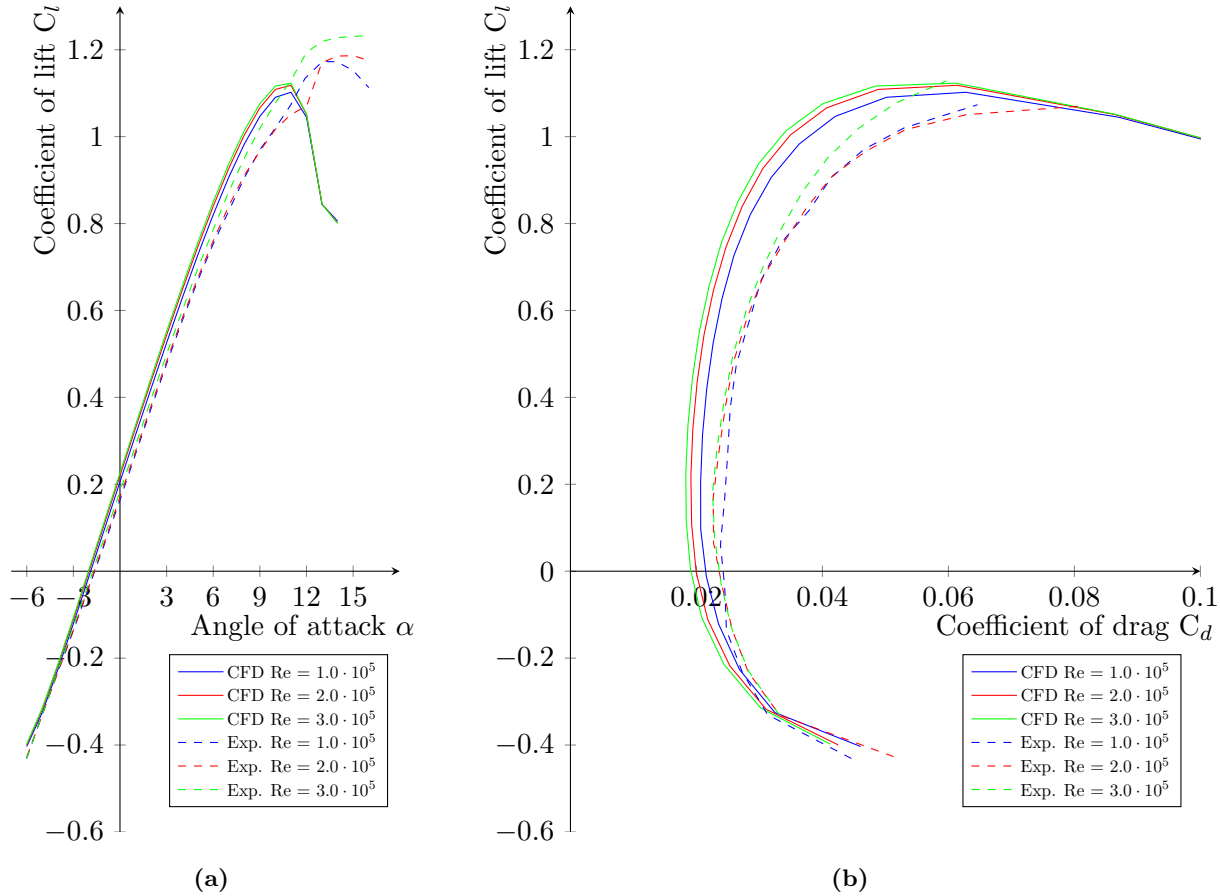

Figure 6.7.: Comparison between experimental and simulation results of the rime ice (-10°C) shape.

6.2.5. Rime Ice (-15°C) Results

The comparison of the simulation and experimental results of the rime (-15°) ice shape can be seen in Figure 6.8. The linear section of the lift curve showed very good agreement between the simulation results and the experimental results, with minimal deviations between the two curves. One exception of the good agreement was discovered for negative angles of attack at Re = 100 000. The simulation did not predict the laminar flow regime discussed in subsection 6.1.1, which occurred only at Re = 100 000. Therefore, lift performance was over-predicted significantly by the simulation in this region. The maximum coefficient of lift was predicted at $\alpha = +11°$ for all three Reynolds number regimes. This matched the experimental results for the two higher Reynolds number regimes. For Re = 100 000, this was only off by $\Delta\alpha = 1°$. However, there was no agreement in the stall behavior between simulation and experimental results. The simulation results suggested a very aggressive stall behavior, while the experimental data exhibited a more gradual decrease of lift.

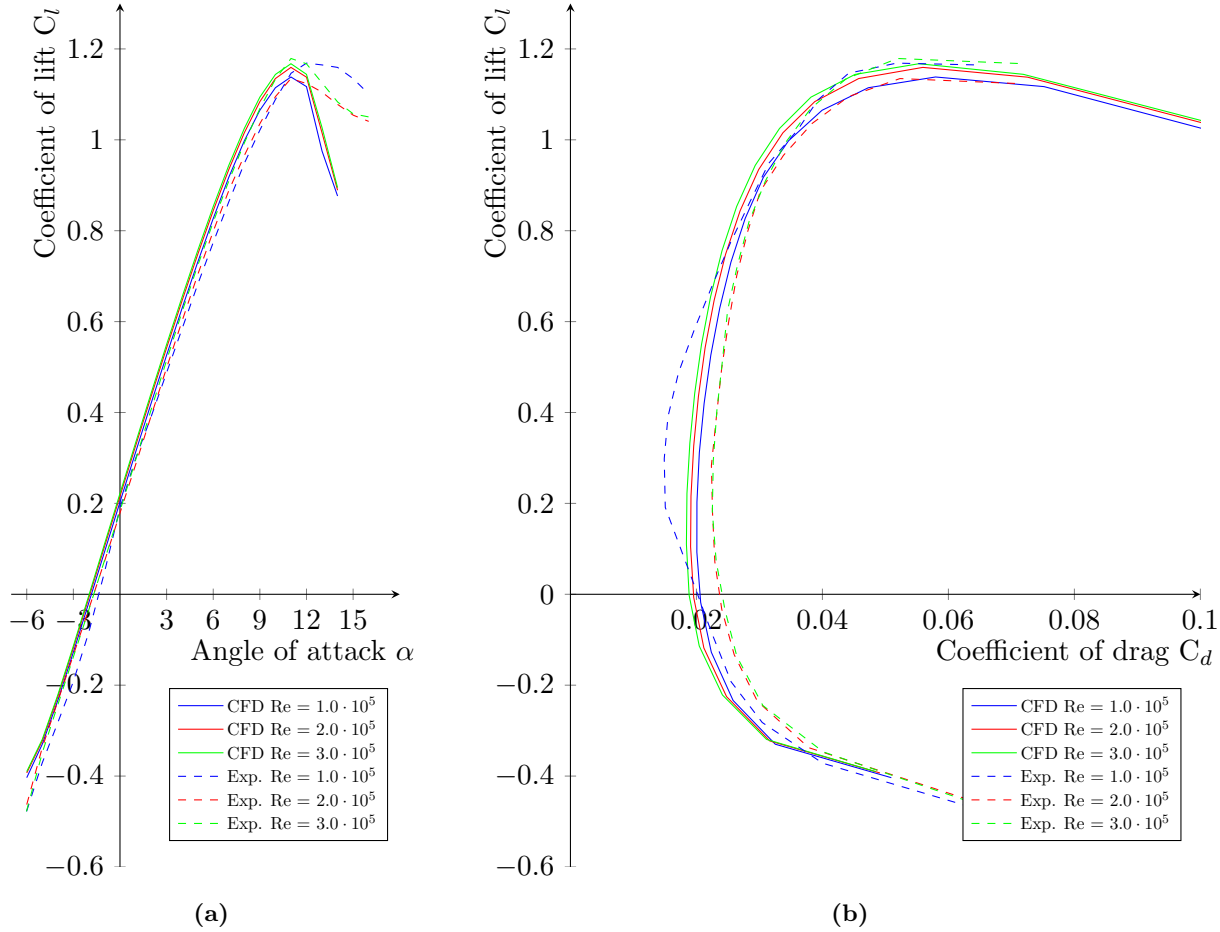

Figure 6.8.: Comparison between experimental and simulation results of the rime ice (-15°C) shape.

The drag curves showed, similarly to the lift curves, good agreement between simulation and experimental data. The overall shape and position of the drag curves had the best agreement of all ice shapes. The drag at $\alpha = 0°$ had a deviation of $\Delta C_d = -18$ to $+33\%$ at Re = 300 000 and Re = 200 000. The deviation was significantly larger for Re = 100 000 with $\Delta C_d = +20\%$, as the laminar flow region, as mentioned above, was not predicted by the simulation. This was notably the only case where the drag was over-predicted by the simulations. Simulations were only run until $\alpha = +14°$

for the rime (-15°C) ice shape, similarly to the rime (-10°C) ice shape. All simulations did converge sufficiently within the time step limit for the current range of angles of attack.

6.3. Discussion of Results

This section provides a discussion of the results presented above. First, a discussion about the experimental findings is presented. Thereafter, a discussion of the numerical results and the numerical methods will be presented.

6.3.1. Experimental Results

For the three Reynolds number regimes investigated, the glaze ice shape showed the highest performance degradation of the four ice shapes. This result agrees with existing literature on aerodynamic performance penalties of iced airfoils at low Reynolds numbers [23, 32]. Lindner et al. [32] investigated numerically the influence of different ice shapes on a wing and an empennage with respect to the aerodynamic penalties and concluded that ice shapes from glaze conditions have the highest performance degradation. The horn-like geometry is the main driver of the aerodynamic performance degradation of glaze ice. The horns induce a separation bubble, which forms near the outermost point of the ice. The flow cannot overcome the adverse pressure gradient caused by the horns, resulting in boundary layer separation [10]. Kim and Bragg [31] investigated the dependency of geometry features of horns on aerodynamic performance degradation. They found that the dominant factors are the horn height and location, as they drive the separation bubble. The shape and the roughness of the ice are of less importance with respect to aerodynamic performance degradation. Furthermore, Kim and Bragg [31] investigated the effect of the Reynolds number on the maximum lift. They found that the Reynolds number in the range Re = 500 000 up to Re = 1 800 000 had little effect on the maximum coefficient of lift of an airfoil with simulated glaze ice horns. The results of this thesis show a difference in the maximum coefficient of lift between the lowest Reynolds number Re = 100 000 and the higher Reynolds numbers of Re = 200 000 and Re = 300 000. It can be observed from the experimental results in Figure 6.5a that the maximum coefficient of lift at Re = 100 000 is notably lower than at Re = 200 000 and Re = 300 000. The difference of the maximum coefficient of lift from the highest and lowest Reynolds number is 3.4%. This suggests that the maximum coefficient of lift for airfoils with glaze ice shapes is dependent on the Reynolds number, as one would expect for clean airfoils [43]. Hann et al. [23] observed the same dependency on the Reynolds number in the Reynolds number range of Re = 200 000 to 600 000 for a glaze ice shape.

In terms of drag, the clear trend of decreasing drag with increasing Reynolds number observed for the clean airfoil is less evident for the glaze ice case. There is a clear decrease of drag visible from Re = 100 000 to Re = 200 000, as displayed in Figure 6.5b. Increasing the Reynolds number from Re = 200 000 to Re = 300 000 has no significant effect on the drag curve. This suggests that the transition locations and the laminar run length are very similar at these two Reynolds numbers. This would be supported by the theory from [10], who proposed that the horns of glaze ice shapes define the separation location. The drag increase for the lowest Reynolds number of Re = 100 000 can be explained by an earlier laminar-turbulent transition or a larger separation region because of an earlier separation.

The mixed ice shape had the second highest aerodynamic performance degradation across the three Reynolds number regimes, which is expected, as the geometry of the mixed ice shape can be inter-

preted as a combination of glaze and mixed ice. The mixed ice shape is more streamwise than the glaze ice shape but also shows horn-like features. The height of the horns is lower, and they are further back than the horns of the glaze ice. Therefore, the separation bubble is most likely smaller than for the glaze ice shape, and performance degradation is expected to be smaller [10]. Also, for the mixed ice, the performance degradation seems to be dependent on the Reynolds number. The same behavior as for glaze ice is observable, where the drag curves of Re = 200 000 and Re = 300 000 are almost coincident, while the drag curve of Re = 100 000 is shifted to higher drag values. As this behavior is similar to the glaze ice shape, the explanation which was used above is also reasonable for the mixed ice shape.

Another feature of the mixed ice shape that must be discussed is the plateau-like shape of the lift curve near the stall region. For the three Reynolds numbers investigated, the lift curves of the mixed ice shape exhibit a plateau-like shape near the stall region. The three lift curves have approximately the same angle of attack, where stall is onset, and the lift curve flattens. Increasing the angle of attack beyond this point does not immediately lead to a loss of lift. The lift values are almost constant for the following angles of attack. This behavior is unexpected, and, to the author's knowledge, has not been documented in the existing literature on low Reynolds number aerodynamics of iced airfoils. It is therefore difficult to explain this behavior in terms of flow characteristics. Only for the lowest Reynolds number regime of Re = 100 000, the stall is captured within the maximum measured angle of attack of $\alpha = +16°$. The stall behavior can be described as aggressive, as lift approximately halves over one angle of attack. For the two higher Reynolds number regimes, the stall behavior is unfortunately not captured, thus restricting the explanation to the lowest Reynolds number regime. The abrupt stall behavior suggests leading edge stall, which is contradictory, since separation at the leading edge is already expected for low angles of attack because of the ice geometry. Also, the plateau-like shape of the stall region is considered not typical for leading edge stall [35]. Given that this behavior was only documented for a single Reynolds number, and no supporting literature has been found, no conclusion could be made.

An important consideration when interpreting the experimental results at high angles of attack is the high blockage of the wind tunnel. The maximum blockage, which occurs at $\alpha = +16°$, was calculated for the clean airfoil and the four ice shapes, and is displayed in Table 6.1. The blockage is for all configurations considered to be at the higher limit of a reasonable wind tunnel blockage, which is typically defined as 5-10% [7]. A high blockage due to a high angle of attack of a wing model results in a high downward deflection of the incoming freestream. This results in an unnatural pressure increase on the lower side of the wing, affecting the measured coefficient of lift.

Leading Edge Shape	**Value**
Clean	9.27%
Glaze (3D)	9.61%
Mixed (3D)	9.73%
Rime (-10°C)(3D)	9.73%
Rime (-15°C)(MCCS)	9.77%

Table 6.1.: Solid blockage values of the different leading edge configurations at $\alpha = +16°$.

The two rime ice shapes induced the lowest performance degradation of the four ice shapes across the three Reynolds number regimes. This was also expected, as the rime ice geometries are significantly more streamlined, and do not feature horn-like protrusions as the glaze and mixed ice shape. Therefore, flow separation is less significant compared to ice shapes with horns [10]. The aerodynamics

of the rime ice shapes are quite different from the glaze ice shapes. As rime ice shapes are more streamlined, they do not necessarily lead to separation [50]. A drag increase compared to the clean airfoil is then introduced by the ice roughness and/or an earlier laminar-turbulent transition induced by the ice shape. If rime ice shapes lead to flow separation, deviations in the flow characteristics of glaze ice shapes can still be defined. The separation point might not be fixed, as for glaze ice with significant horns, but can move upstream or downstream depending on the angle of attack of the incoming flow [10]. Oo et al. [40] found that an ice-induced separation bubble for streamwise ice shapes at low Reynolds numbers acts similarly to a laminar separation bubble with a transition region and downstream reattachment. This ice-induced separation bubble grows in size as the attack angle increases until no reattachment is achieved and the flow is fully separated.

Table 6.2 summarizes the performance degradation of the four ice shapes.

Leading edge shape	ΔC_l **at 4°**	ΔC_d **at 4°**	$\Delta C_{l,max}$
Glaze (3D)	-10/-8/-8%	+289/+415/+483%	-21/-21/-22%
Mixed (3D)	-9/-8/-9%	+168/+264/+307%	-4/-2/-4%
Rime (-10°C)(3D)	-10/-9/-8%	+89/+158/+191%	+10/+10/+11%
Rime (-15°C)(MCCS)	-8/-6/-4%	+31/+131/+160%	+10/+5/+6%

Table 6.2.: Summary of performance degradation of the different ice shapes at Re = 100 000/200 000/300 000.

Distinguishing between flow with and without an ice-induced separation bubble solely with the lift and drag data is difficult. However, it is possible to give a qualitative explanation of the flow characteristics based on the geometrical differences of the rime (-10°C) and rime (-15°C) ice shapes. Considering the two ice shape geometries in Figure 3.2, it can be noted that the the leading edge shapes and the surface roughness features are quite similar for both rime cases. However, the rime (-15°C) ice shape extends longer in the chordwise direction on the upper and lower side and has, therefore, a more gradual transition to the clean airfoil than the rime (-10°C) ice shape. In this transition region, an adverse pressure gradient may exist [10]. As the transition region is smoother for the rime (-15°C) ice shape, this adverse pressure gradient may be smaller and will consequently have less influence on flow separation. If flow separation occurs, it is therefore likely that the separation bubble is larger for the rime (-10°C). This theory is supported by the bigger drag increase of the rime (-10°C) ice shape with increasing angles of attack.

At the lowest Reynolds number of Re = 100 000, an interesting feature was observed for the rime (-15°C) ice shape that needs further discussion. A local region of lower drag values can be seen in Figure 6.8b. As this only occurs at the lowest Reynolds number, indicates that this is an effect of laminar flow. A possible explanation for this effect is that the rime (-15°C) ice shape has a region where laminar flow extends beyond the rough ice shape. The instability induced by the ice shape on the boundary layer is not enough to trigger an instant transition to turbulence of the boundary layer. This leads to a longer laminar run and consequently lower drag due to lower skin friction of the laminar boundary layer [41]. At higher Reynolds numbers, no such region of low drag can be observed. Considering the theory above, for the higher Reynolds numbers, it is reasonable to believe that the instability of the ice shape is enough to trigger a transition to turbulence, and the length of the laminar run is reduced. This implies that it is incorrect to assume a rapid laminar-turbulent transition for all ice shapes at low Reynolds numbers. This phenomenon will be investigated further in subsection 6.3.2 with the aid of the numerical results.

Another feature of the rime (-10°C) ice shape is the unusual stall behavior that was described in the

sections above. An onset of stall can be observed in the lift curve for all three Reynolds number regimes. However, with increasing the angle of attack, the coefficient of lift rises further to higher values before stalling. This feature was also observed for the clean airfoil, however less significant. Hann [22] observed a similar feature for a mixed, a rime, and a glaze ice shape. He proposed the idea that the initial break in the lift curve is caused by the onset of trailing-edge separation, and the lift increase is caused by the ice shape acting as a nose droop or a localized separation bubble. Jasinski et al. [28] also observed similar results and argued that the effects are similar to what one would expect from a leading edge flap.

Another feature at high angles of attack that was observed for both rime ice shapes was an increase in the maximum coefficient of lift compared to the clean airfoil. The maximum coefficient of lift increased as much as $\Delta C_{l,max} = +11\%$ for the rime (-10°C) ice shape and $\Delta C_{l,max} = +10\%$ for the rime (-15°C) ice shape. No clear trend of this increase could be observed for the investigated Reynolds number range. In order to investigate this behavior further, the aerodynamic coefficients were normalized by the total chord length, consisting of the clean airfoil chord length and the ice thickness. These polars are attached in Appendix C. Considering the normalized lift curve, one can observe that the maximum coefficient of lift for most cases still exceed the clean airfoil cases. This phenomenon of an increase of the maximum coefficient of lift induced by leading-edge ice has been observed by researchers before. Jasinski et al. [28] discovered this behavior when investigating an S809 wind turbine airfoil with rime ice accretions. Their study was, however, conducted at higher Reynolds numbers of Re = 1–2 $\cdot 10^6$. Bragg et al. [11] also discovered this feature while doing an experimental study of the aerodynamic performance of an iced airfoil at Re = 5–6 $\cdot 10^6$. They used the explanation of the similarities to a leading-edge flap for this behavior. This explanation is also reasonable for the low Reynolds number results of this study, as leading-edge flaps have the same effect at lower Reynolds numbers [29]. As this feature occurs at high angles of attack, the consideration of the wind tunnel blockage, which was mentioned above, should be considered.

6.3.2. Numerical Results

The review of the simulation results showed clear limitations of the numerical methods applied. For all simulations, the linear section of the lift curves was reproduced within an acceptable margin compared to the experimental data. However, clear shortcomings are observable in the stall region. Apart from the rime (-15°C) ice shape, the simulations predicted an earlier stall with a significantly lower maximum coefficient of lift for all remaining cases. No clear trend is observable for the deviations of the stall angle and the maximum coefficient of lift for the different cases. There is also no evidence of a dependency on the Reynolds number. In addition to the preliminary stall prediction, the numerical methods showed limitations in predicting the stall behavior. The general limitations of Reynolds-averaged Navier-Stokes simulations with the k–ω SST turbulence model are known for stalled airfoil aerodynamics [37]. These limitations of RANS could be eliminated by using another turbulence modeling approach, like Large Eddy Simulations (LES) or Detached-Eddy Simulations (DES) . Thompson and Mogili [49] compared results of Detached-Eddy Simulations with RANS simulations for separated flow around iced wings. They concluded that for flows with large detached areas, DES simulations exhibit a better agreement with experimental lift and drag data. Additionally, they believe that DES simulations can be advantageous over RANS simulations for flow fields that exhibit extensive three-dimensional features. However, DES requires more computational resources than RANS simulations. It is therefore uncertain, if the increased accuracy of DES simulations is considered is worth the increased computational requirements.

Generally, drag underestimated by the simulations compared to the experimental data. It is well known that RANS turbulence models struggle with an under-prediction of the turbulent stresses in the detached shear layer [37]. This can explain the consistent under-prediction of the drag, as separation regions are assumed to exist for the ice shapes for the majority of angles of attack. There seems to be a correlation of the deviation to the ice shape, where the glaze and mixed ice shape experience a larger deviation compared to the two rime ice shapes. This is reasonable, since the glaze and mixed ice are expected to have larger separation regions. The limitation of inaccurate drag predictions of iced airfoils with horn ice has been well-documented in literature (e.g. [22] [12]), and is also considered for the streamwise ice shapes.

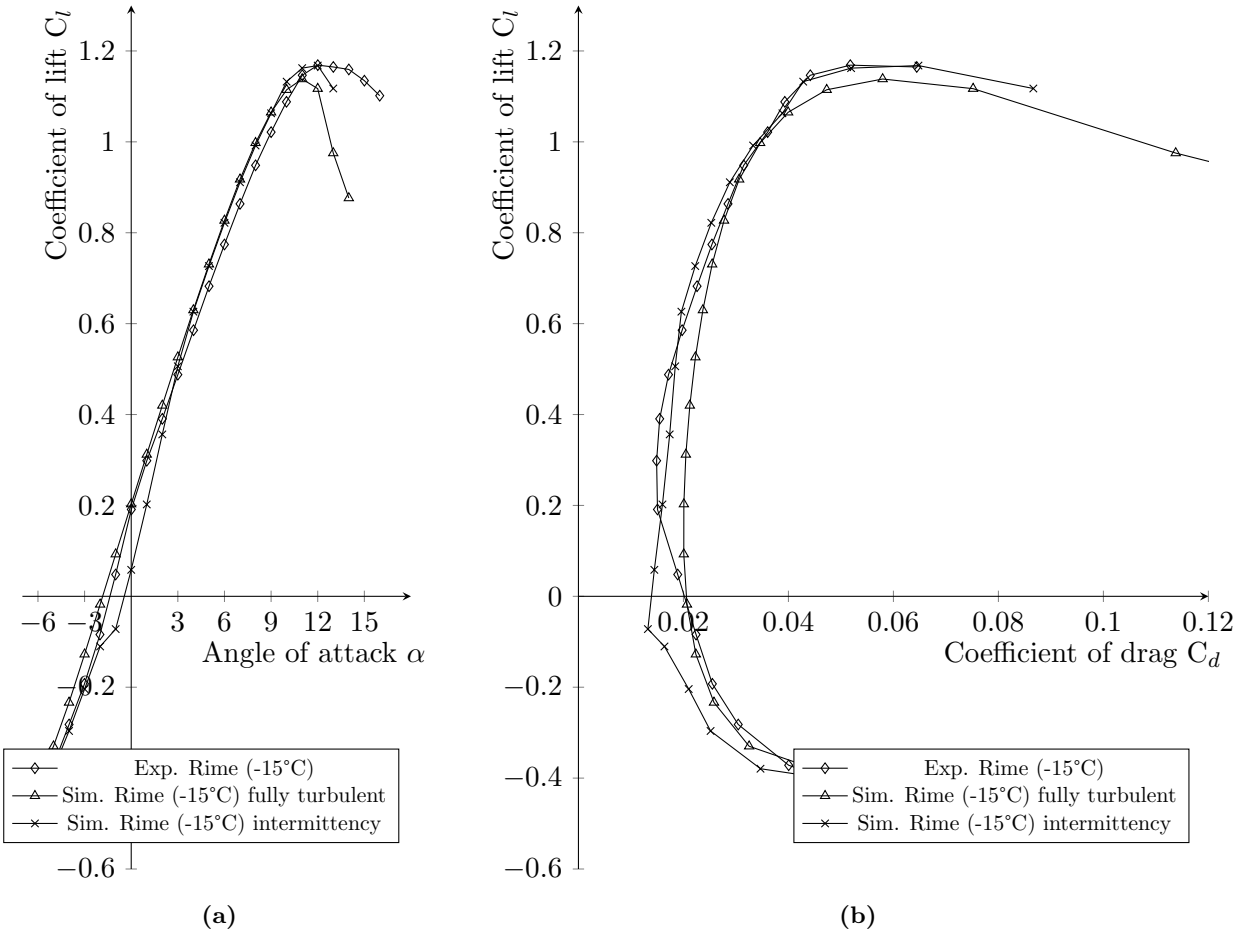

Figure 6.9.: Comparison of rime (-15°C) ice shape experimental data to simulation results with and without intermittency.

It is also necessary to discuss the validity of the comparison between the experimental results of the three-dimensional ice shapes and the simulation results of the two-dimensional MCCS ice shapes. The best agreement between the simulation and experimental results was for the rime (-15°C) ice shape. This was the only case where the identical geometry was investigated in the simulations as in the experiments. For the other three ice shapes, three-dimensional ice shapes were investigated experimentally and the two-dimensional MCCS ice shapes were analyzed numerically. For these comparisons, agreement was less favorable. This could indicate that the two-dimensional MCCS ice shapes do not fully represent all the features of the three-dimensional ice shapes in terms of aerodynamic performance degradation. It is, however, challenging to isolate the contribution of the

discrepancies, originating from the conversion of the three-dimensional ice shape to a two-dimensional MCCS ice shape. Other factors (e.g., CFD limitations) might contribute to the discrepancies between the experimental and numerical results. Direct comparisons between three-dimensional ice shapes and their two-dimensional MCCS shapes must be conducted experimentally to investigate the possible error made due to the conversion process.

As discussed in subsection 6.3.1, the experimental drag curve suggests a local region of laminar run beyond the ice shape at Re = 100 000 for the rime (-15°C) ice shape. Consequently, the assumption of an instant laminar-turbulent transition of the boundary layer used in the simulations is questionable for low Reynolds numbers. In order to investigate this further, additional simulations of the rime (-15°C) ice shape with the intermittency transition model were performed at the Reynolds number of Re = 100 000. These additional results are displayed in Figure 6.9. The drag curves with and without the intermittency transition model show significant differences, which supports the theory of the presence of increased laminar run for this case. Figure 6.10 displays the turbulence viscosity of the flow field around the iced airfoil for both simulations at an angle of attack of $\alpha = +2°$.

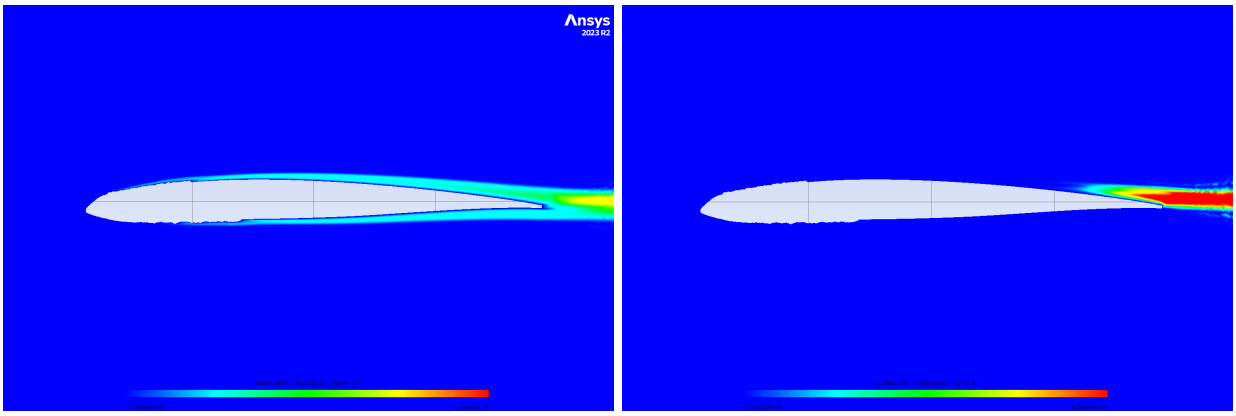

(a) **(b)**

Figure 6.10.: Comparison of turbulent viscosity distribution of rime (-15°C) ice shape simulation results: (a) fully turbulent and (b) with the intermittency transition model.

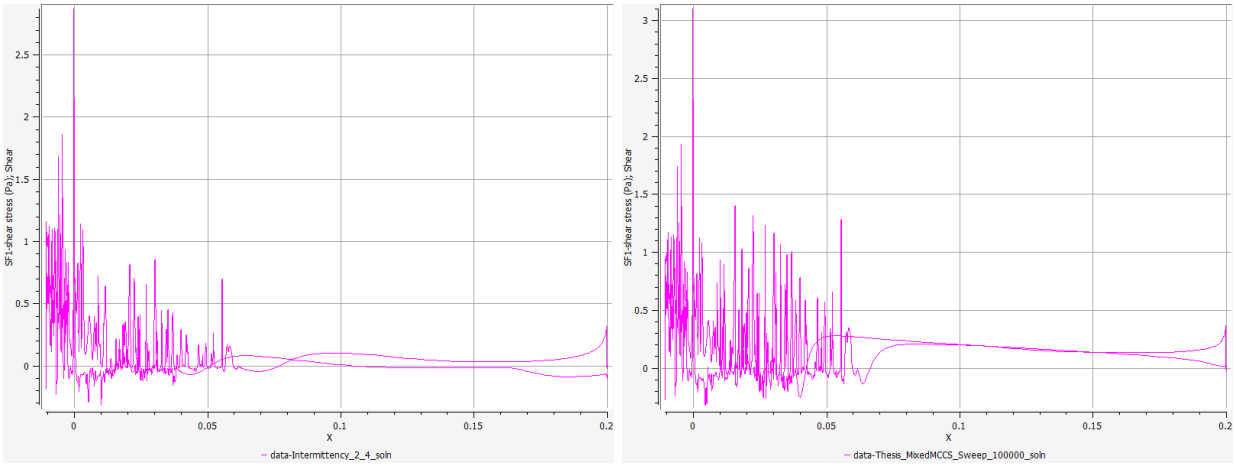

(a) **(b)**

Figure 6.11.: Comparison of wall shear stress of rime (-15°C) ice shape simulation results with (b) and without (a) intermittency.

The simulation with the intermittency transition model shows long laminar run lengths on both sides of the airfoil. This is not the case for the fully turbulent simulation, as the boundary layer is modeled to be fully turbulent. The change of the boundary layer characteristics influences the overall flow characteristics around the iced airfoil. Figure 6.11 shows the shear stress distribution of the upper and lower sides at $\alpha = +2°$. Small separation regions with a negative wall shear stress can be observed for the fully turbulent case over the ice shape on both the upper and lower sides. Behind the ice shape flow is however attached for the majority of the remaining chord length. On the contrary, the intermittency results show flow separation without reattachment on the upper side from about 0.5% chord. This reflects the laminar boundary layer characteristics, being more prone to separate compared to a turbulent boundary layer [41]. Interestingly, the simulation predict that the drag increase, produced by the separation bubble, is less than the drag reduction due to longer laminar runs on the upper and lower sides. The results should however be viewed with caution, as the RANS simulations struggled to predict laminar and/or turbulent separation correctly. To conclude, these results indicate that the assumption of a fully turbulent boundary layer for low Reynolds numbers is not valid for the rime (-15°C) ice shape, This also raises the question of whether the assumption of a fully turbulent boundary layer is valid for the other ice shapes investigated numerically in this thesis. Further investigation would be required to address that question.

7. Conclusion and Outlook

In this thesis, an experimental and numerical study has been conducted in order to investigate the aerodynamic performance degradation of a RG-15 airfoil with artificial ice shapes at low Reynolds numbers. The aerodynamic performance degradation was investigated in terms of drag increase and lift decrease for four different ice shapes.

The investigated ice shapes were obtained in the icing wind tunnel of the VTT Technical Research Centre of Finland by Hann et al. [26]. The four ice shapes represent the typical ice types defined by the Federal Aviation Administration, which are wet (glaze, -2°C), mixed (-4°C), and dry (rime, -10°C), and dry (rime, -15°C) icing conditions. The investigation was conducted at three low Reynolds number regimes of Re = 100 000, Re = 200 000, and Re = 300 000, and a range of angles of attack of $\alpha = -6°$ up to $\alpha = +16°$.

The experimental study consisted of a wind tunnel measurement campaign in the Model Wind Tunnel at the University of Stuttgart. The Model Wind Tunnel is an open loop wind tunnel with a closed test section able to produce Reynolds numbers of up to Re = 400 000. For the experiments, a solid wing model out of polyurethane was produced. The rectangular wing model had a chord length of 200 mm and was based on the RG-15 airfoil with a blunt trailing edge. The artificial ice shapes were manufactured from polyamide 12 using the selective laser sintering (SLS) 3D printing method. For the experimental study, the glaze, mixed and rime (-10°C) ice shapes were manufactured as three-dimensional ice shapes. The rime (-15°C) was manufactured as a constant cross-section ice shape, which was created using the Maximum Combined Cross Section (MCCS) method. Lift and drag measurements were conducted to investigate the aerodynamic performance degradation induced by the ice shapes. First, measurements of the clean wind tunnel model were conducted to serve as the baseline performance data of the RG-15 airfoil. Then, measurements of the wing model with the attached artificial ice shapes were conducted. The angular resolution of the measurements was $\alpha = 1°$. The lift measurements were performed using a load cell measurement system. The drag measurements were performed using the momentum deficit method and a wake rake behind the wing model.

The numerical study was performed using FENSAP-ICE (release 2023 R2). Only the module FENSAP was used for all simulations, which was set up to calculate the two-dimensional steady-state Reynolds-averaged Navier-Stokes (RANS) equations. For the turbulence modeling, the two-equation k–ω SST turbulence model was used. For the clean airfoil performance simulations, the intermittency transition model is used for the prediction of the transition point. All iced airfoil simulations were run with a fully turbulent boundary layer. The three-dimensional ice shape models were converted to two-dimensional MCCS ice shapes for the simulations. All meshes were created in Pointwise (version 2023.2.2). Different setups were used for the clean airfoil performance meshes and the iced airfoil performance meshes. For both setups, a mesh dependency study was conducted applying a Richardson extrapolation.

The experimental results of the clean airfoil performance showed good agreement with existing experimental data of the RG-15 airfoil. For the experimental results of the airfoil with artificial ice

shapes, a trend of the aerodynamic performance degradation was observed for the different ice shape geometries. The aerodynamic performance degradation was higher for the ice shapes that exhibited horn-like features. Also, a trend of increasing performance penalties with increasing Reynolds number was observed. These observed trends are in agreement with existing literature on the aerodynamics of iced airfoils.

The glaze ice had the highest performance degradation at all three Reynolds number regimes. The mixed ice shape was less severe, however, had higher aerodynamic performance degradation than both rime ice shapes. From the two rime ice shapes, the rime (-10°C) ice shape, investigated as a three-dimensional ice shape, showed higher performance degradation than the rime (-15°C), which was investigated as a MCCS ice shape. At the highest investigated Reynolds number of Re = 300 000, and an angle of attack of $\alpha = +4°$, the coefficient of drag increased by +483% for the glaze ice shape, +307% for the mixed ice shape, +191% for the rime (-10°C) ice shape, and +160% for the rime (-15°C) ice shape. For the same conditions, the coefficient of lift decreased by -8% for the glaze ice shape, -9% for the mixed ice shape, -8% for the rime (-10°C) ice shape, and -4% for the rime (-15°C) ice shape.

Several interesting and unexpected features have been observed from the experimental results. The mixed ice shape showed a plateau-like behavior in the stall region of the lift curve across all three Reynolds numbers investigated. The onset of stall occurred at a similar angle of attack for each case, after which the lift remains nearly constant over a range of angles. At Re = 100,000, an abrupt loss of lift is observed beyond the plateau-like region, suggesting leading-edge stall characteristics. This is, however, inconsistent with expected early separation due to the mixed ice shape. High wind tunnel blockage at large angles of attack may contribute to the results by artificially increasing lift and altering the results. Given these factors, no definitive explanation can be given, and further investigation is recommended.

Another unexpected feature was observed for the rime (-10°C) ice shape near in the stall region. The lift curve exhibited an unusual shape at high angles of attack. A clear onset of stall was observed for all three Reynolds numbers. However, increasing the angle of attack resulted in another rise of the coefficient of lift, before experiencing a final decrease. This secondary rise in lift is atypical and was also observed, though to a lesser extent, for the clean airfoil. Similar behavior has been documented in existing literature before, where it has been suggested that the effects resemble those of leading-edge flaps. However, the aerodynamic mechanisms remain uncertain and require further investigation.

The maximum achievable coefficient of lift was reduced for the glaze and the mixed ice shapes across all investigated Reynolds numbers. Surprisingly, for the two rime ice shapes, the maximum coefficient of lift was increased compared to the clean airfoil. The increase did not show a consistent trend across the Reynolds numbers. Even after normalizing the coefficient of lift by the total chord length of the airfoil plus the artificial ice shape, the maximum coefficient of lift remained higher than for the most cases of the clean airfoil. Similar lift-increasing effects have been documented before for iced airfoil aerodynamics at higher Reynolds numbers. The current literature considers this behavior similar to the induced effects of leading-edge flaps. This is considered reasonable for the current results at low Reynolds numbers. However, for this feature, the uncertainty of the relevance of the high blockage at large angles of attack must also be acknowledged.

The last unexpected behavior was observed for the rime (-15°C) ice shape at the lowest Reynolds number of Re = 100 000. A local region of reduced drag was observed at low angles of attack. This behavior suggests a laminar flow effect, wherein the boundary layer remains laminar beyond

the rough surface of the ice shape. The induced instabilities on the boundary layer seem insufficient to trigger an immediate transition to turbulence, resulting in a longer laminar run and thus lower drag. At higher Reynolds numbers, this effect disappeared, which supports the presented theory. These findings suggest that laminar-turbulent transition location can play a key role in the drag characteristics of iced airfoils at low Reynolds numbers.

The results of the simulations highlight several key findings. While the linear section of the lift curves had reasonable agreement with the experimental data for all cases, the stall region revealed significant shortcomings. The simulations consistently predicted an earlier stall and a lower maximum coefficient of lift compared to the experimental data. These results highlight the known limitations for separated or stalled flow regimes of the k–ω SST turbulence model in Reynolds-averaged Navier-Stokes simulations. The review of the general drag results supported these limitations, as drag was generally under-predicted significantly by the simulations. A trend of increasing deviations between the simulation and experimental drag results was observed with more complex ice shapes, such as the glaze and mixed ice shapes.

This study highlighted several complex aerodynamic effects caused by ice accretion on an RG-15 airfoil at low Reynolds numbers. While the experimental data showed valuable features, further investigation at low Reynolds numbers with different measurement or visualization methods is needed to understand the underlying flow phenomena better. The limitations of RANS simulations with the k–ω SST turbulence model suggest that other approaches, such as Detached-Eddy simulations or Large-Eddy simulations, could be investigated for regions of separated flow. Furthermore, additional work is needed to assess how the aerodynamic performance degradation behaves for a broader range of Reynolds numbers and a broader range of ice shapes.

Bibliography

[1] S. M. Aftab, A. S. Mohd Rafie, N. A. Razak and K. A. Ahmad: *Turbulence Model Selection for Low Reynolds Number Flows*. 04 2016.

[2] D. Althaus: *Measurement of Lift and Drag in the Laminar Wind Tunnel*. `https://www.iag.uni-stuttgart.de/dateien/pdf/laminarwindkanal_messtechniken/althaus_2.pdf`. Accessed: 2025-03-26.

[3] D. Althaus: *Tunnel-Wall Corrections at the Laminar Wind Tunnel*. `https://www.iag.uni-stuttgart.de/dateien/pdf/laminarwindkanal_messtechniken/althaus_1.pdf`. Accessed: 2025-03-26.

[4] D. Althaus, ed.: *Recent Wind Tunnel Experiments at Lower Reynolds Numers*. Proceedings of the Aerodynamics at Low Reynolds Numbers $10^4 < Re < 10^6$, London, England, October 1986, Interantional Conference.

[5] J. D. Anderson: *Fundamentals of Aerodynamics*. McGraw-Hill Education, 2017.

[6] ANSYS, Inc.: *Ansys FENSAP-ICE User Manual*, Canonsburg, PA, 2023.

[7] J. B. Barlow, W. H. Rae and A. Pope: *LOW-SPEED WIND TUNNEL TESTING*. John Wiley & Sons, Third Avenue, New York, 1999.

[8] B. C. Bernstein and C. Le Bot: *An inferred climatology of icing conditions aloft, including supercooled large drops. Part II: Europe, Asia, and the Globe*. 2009.

[9] B. C. Bernstein, C. A. Wolff and F. McDonough: *An inferred climatology of icing conditions aloft, including supercooled large drops. Part I: Canada and the continental United States*. 11 2007.

[10] M. B. Bragg, A. P. Broeren and L. A. Blumenthal: *Iced-airfoil aerodynamics*. 2005.

[11] M. B. Bragg, R. J. Zaguli and G. M. Gregorek: *WIND TUNNEL EVALUATION OF AIRFOIL PERFORMANCE USING SIMULATED ICE SHAPES*. tech. rep., The Ohio State University, Columbus, Ohio, November 1982.

[12] L. Brandrud and J. Krøgenes: *Aerodynamic Performance of the NREL S826 Airfoil in Icing Conditions*. Master's thesis, Norwegian University of Science and Technology, June 2017.

[13] A. P. Broeren, M. G. Potapczuk, S. Lee, A. M. Malone, B. P. Paul Jr. and B. S. Woodard: *Ice-Accretion Test Results for Three Large-Scale Swept-Wing Models in the NASA Icing Research Tunnel*. Tech. Rep. NASA/TM—2016-219137, NASA, Cleveland, Ohio, September 2016.

[14] Y. Cao, W. Tan and Z. Wu: *Aircraft icing: An ongoing threat to aviation safety*. 4 2018.

[15] FAA: *Pilot Guide: Flight in Icing Conditions*. Advisory Circulars, No. AC 91-74B, October 2015. Accessed: 2025-02-27.

[16] N. Fajt: *The Influence of Meteorological Conditions on the Icing Performance Penalties on a*

UAV Airfoil. Master's thesis, University of Stuttgart, July 2019.

[17] R. Fiolka: *Memories of the RG 15 Airfoil Development*. `https://f3b-league.blogspot.com/2007/08/`. Accessed: 2025-04-30.

[18] Furness Controls Limited: *Pressure and Flow Measurements*, Bexhill, United Kingdom. Data Sheet.

[19] R. Girsberger: *New Airfoils for R/C-Gliders*. Accessed: 2025-04-30.

[20] H. Glauert: *Wind Tunnel Interference on Wings, Bodies and Airscrews in a Two-Dimensional-Flow Wind Tunnel with Consideration of the Effect of Compressibility*. British A. R. C., No. 1566, 1938.

[21] W. G. Habashi, M. Aube, G. Baruzzi, F. Morency and P. Tran, eds.: *FENSAP-ICE: A FULLY-3D IN-FLIGHT ICING SIMULATION SYSTEM FOR AIRCRAFT, ROTORCRAFT AND UAVS*. 24th International Congress of the Aeronautical Sciences, 2004.

[22] R. Hann: *Atmospheric Ice Accretions, Aerodynamic Icing Penalties, and Ice Protection Systems on Unmanned Aerial Vehicles*. PhD thesis, Norwegian University of Science and Technology, July 2020.

[23] R. Hann, J. R. Hearst, L. R. Sætran and T. Bracchi: *Experimental and Numerical Icing Penalties of an S826 Airfoil at Low Reynolds Numbers*. April 2020.

[24] R. Hann and T. A. Johansen: *Unsettled Topics in Unmanned Aerial Vehicle Icing*. 03 2020.

[25] R. Hann and T. A. Johansen: *UAV icing: the influence of airspeed and chord length on performance degradation*. Aircraft Engineering and Aerospace Technology, Vol. 93, No. 5, pp. 832–841, 2021.

[26] R. Hann, N. Müller, M. Lindner and J. Wallisch: *UAV Icing: Experimental Validation Data for Predicting ice Shapes at Low Reynolds Numbers*. 06 2023.

[27] International Civil Aviation Organization: *Manual of the ICAO Standard Atmosphere*, Montreal, Canada, 1993. Release 3.

[28] W. J. Jasinski, S. C. Noe, M. S. Selig and M. B. Bragg: *Wind Turbine Performance Under Icing Conditions*. 1998.

[29] A. Jones, N. Bakhtian and H. Babinsky: *Low Reynolds Number Aerodynamics of Leading-Edge Flaps*. 01 2008.

[30] B. M. Jones: *The measurement of profile drag by the pitot traverse method*. ARC RM, No. 1688, 1936.

[31] H. S. Kim and M. B. Bragg: *Effects of leading-edge ice accretion geometry onairfoil performance*. In: 17th Applied Aerodynamics Conference, American Institute of Aeronautics and Astronautics Inc, AIAA, 1999, pp. 379–391.

[32] M. Lindner, J. Wallisch and R. Hann: *UAV Icing: Numerical Simulation of Icing Effects on Wing and Empennage*. 06 2023.

[33] T. Lutz: *Airfoil Design*. 2020. Script for lecture and seminar.

[34] F. Martini, H. Ibrahim, L. T. Contreras Montoya, P. Rizk and A. Illinca: *Turbulence Modeling of Iced Wind Turbine Airfoils*. Energies, Vol. 15, No. 8325, 2022.

[35] M. A. McVeigh and E. Kisielowski: *A Design Summary of Stall Characteristics of Straight*

Wing Aircraft. Tech. Rep. NASA CR—1646, NASA, Washington D.C., June 1971.

[36] F. R. Menter: *Two-Equation Eddy-Viscosity Turbulence Models for Engineering Applications*. 1994.

[37] F. R. Menter, M. Kuntz and R. Langtry: *Ten Years of Industrial Experience with the SST Turbulence Model*. October 2003.

[38] T. J. Mueller, L. J. Pohlen, P. E. Conigliaro and B. J. Jansen: *The Influence of Free-Stream Disturbances on Low Reynolds Number Airfoil Experiments*. 1983.

[39] University of Stuttgart: *Model Wind Tunnel*. `https://www.iag.uni-stuttgart.de/en/institute/test-facilities/model-wind-tunnel/`. Accessed: 2025-01-09.

[40] N. L. Oo, P. J. Richards and R. N. Sharma: *Ice-Induced Separation Bubble on RG-15 Airfoil at Low Reynolds Number*. 2020.

[41] H. Schlichting and K. Gersten: *Boundary-Layer Theory*. Springer-Verlag, Berlin, Germany, 2017.

[42] R. Schwarze: *CFD-Modellierung*. Springer Berlin Heidelberg, 2013.

[43] M. S. Selig, J. F. Donovan and D. B. Fraser: *AIRFOILS AT LOW SPEEDS*. Vol. 1, H. A. Stokely, Virginia Beach, Virginia, 1989.

[44] M. S. Selig, J. J. Guglielmo, A. P. Broeren and P. Giguère: *Summary of Low-Speed Airfoil Data*. Vol. 1, SoarTech Publications, Virginia Beach, Virginia, 1995.

[45] J. Shim, J. Chung and K. Lee: *A comparison of turbulence modeling in flow analysis of iced airfoils*. 08 2000.

[46] P. Spalart and S. Allmaras, eds.: *A one-equation turbulence model for aerodynamic flows*. in 30th aerospace science meeting and exhibit, Reno, USA, January 1992.

[47] K. Szilder and S. Mcllwain: *In-Flight Icing of UAVs - The Influence of Reynolds Number on the Ice Accretion Process*. SAE Technical Paper, No. 2011-01-2572, 2011.

[48] K. L. Sørensen, K. T. Borup, R. Hann, B. C. Bernstein and M. Hansbø: *UAV ATMOSPHERIC ICING LIMITATIONS - CLIMATE REPORT FOR NORWAY AND SURROUNDING REGIONS*. tech. rep., UBIQ Aerospace and Leading Edge Atmospherics and The Norwegian Defence Research Establishment, May 2021.

[49] D. Thompson and P. Mogili: *Detached-Eddy Simulations of Separated Flow Around Wings With Ice Accretions: Year One Report*. Tech. Rep. NASA/CR—2004-213379, NASA, Cleveland, Ohio, November 2004.

[50] M. K. Vinnes and R. J. Hearst: *Aerodynamics of an airfoil with leading-edge icing*. December 2020.

[51] D. C. Wilcox: *Reassessment of the Scale-Determining Equation for Advanced Turbulence Models*. 1988.

[52] D. C. Wilcox: *Turbulence Modeling for CFD*. DCW Industries, January 2006.

[53] F. X. Wortmann, ed.: *Über eine Möglichkeit zur Veermeidung der Insektenrauhigkeit*. Presentation at the 9th. OSTIV-Congress, Junin, Argentina, 1963.

A. RG-15 Airfoil Coordinates

RG-15, blunt trailing edge, 320 points, x, y

1.000371 0.003310	0.746897 0.038304	0.481959 0.059474	0.218638 0.058852
0.997636 0.003744	0.739930 0.039052	0.474991 0.059797	0.211800 0.058361
0.992823 0.004580	0.732962 0.039791	0.468024 0.060105	0.204971 0.057837
0.987191 0.005629	0.725993 0.040521	0.461056 0.060398	0.198152 0.057278
0.980981 0.006801	0.719024 0.041242	0.454089 0.060676	0.191345 0.056683
0.974504 0.008010	0.712054 0.041953	0.447123 0.060940	0.184551 0.056051
0.967955 0.009196	0.705085 0.042654	0.440157 0.061188	0.177771 0.055380
0.961360 0.010345	0.698115 0.043346	0.433193 0.061421	0.171007 0.054670
0.954710 0.011458	0.691144 0.044029	0.426230 0.061638	0.164260 0.053918
0.948002 0.012536	0.684173 0.044701	0.419268 0.061839	0.157531 0.053124
0.941232 0.013584	0.677201 0.045364	0.412309 0.062023	0.150820 0.052284
0.934404 0.014610	0.670228 0.046017	0.405351 0.062191	0.144127 0.051398
0.927529 0.015621	0.663255 0.046661	0.398396 0.062341	0.137452 0.050464
0.920621 0.016621	0.656282 0.047294	0.391442 0.062473	0.130794 0.049479
0.913699 0.017610	0.649308 0.047917	0.384491 0.062588	0.124156 0.048441
0.906772 0.018587	0.642334 0.048530	0.377541 0.062685	0.117545 0.047348
0.899846 0.019551	0.635360 0.049133	0.370593 0.062762	0.110970 0.046199
0.892921 0.020503	0.628387 0.049725	0.363647 0.062821	0.104444 0.044993
0.885995 0.021444	0.621414 0.050306	0.356704 0.062861	0.097976 0.043730
0.879064 0.022374	0.614441 0.050877	0.349762 0.062881	0.091568 0.042404
0.872128 0.023295	0.607469 0.051436	0.342823 0.062881	0.085212 0.041010
0.865186 0.024206	0.600496 0.051984	0.335886 0.062860	0.078891 0.039538
0.858240 0.025108	0.593524 0.052521	0.328951 0.062819	0.072588 0.037979
0.851289 0.026000	0.586551 0.053046	0.322020 0.062756	0.066319 0.036325
0.844337 0.026884	0.579578 0.053560	0.315092 0.062671	0.060148 0.034587
0.837383 0.027758	0.572603 0.054062	0.308168 0.062564	0.054172 0.032789
0.830428 0.028623	0.565628 0.054552	0.301247 0.062434	0.048474 0.030952
0.823472 0.029480	0.558652 0.055031	0.294331 0.062281	0.043039 0.029068
0.816516 0.030327	0.551676 0.055498	0.287420 0.062104	0.037765 0.027096
0.809559 0.031165	0.544700 0.055953	0.280514 0.061902	0.032502 0.024962
0.802601 0.031995	0.537725 0.056397	0.273614 0.061675	0.027261 0.022635
0.795642 0.032815	0.530750 0.056828	0.266719 0.061422	0.022512 0.020316
0.788681 0.033626	0.523777 0.057246	0.259831 0.061141	0.018659 0.018256
0.781720 0.034429	0.516804 0.057651	0.252948 0.060833	0.015606 0.016476
0.774758 0.035222	0.509833 0.058043	0.246072 0.060497	0.013072 0.014862
0.767794 0.036006	0.502864 0.058422	0.239203 0.060132	0.010854 0.013319
0.760829 0.036781	0.495895 0.058787	0.232340 0.059736	0.008824 0.011770
0.753864 0.037547	0.488927 0.059138	0.225485 0.059310	0.006911 0.010153

0.005198 0.008525
0.003817 0.007048
0.002763 0.005793
0.001953 0.004735
0.001328 0.003820
0.000849 0.003000
0.000489 0.002237
0.000231 0.001506
0.000067 0.000785
0.000001 0.000056
0.000046 -0.000696
0.000227 -0.001451
0.000549 -0.002210
0.001020 -0.002979
0.001650 -0.003764
0.002450 -0.004571
0.003429 -0.005404
0.004589 -0.006264
0.005971 -0.007149
0.007634 -0.008056
0.009639 -0.008981
0.012029 -0.009930
0.014842 -0.010941
0.018152 -0.012032
0.022025 -0.013189
0.026468 -0.014373
0.031445 -0.015540
0.036903 -0.016658
0.042740 -0.017705
0.048840 -0.018680
0.055126 -0.019587
0.061544 -0.020424
0.068052 -0.021190
0.074624 -0.021892
0.081252 -0.022535
0.087933 -0.023124
0.094661 -0.023663
0.101429 -0.024160
0.108231 -0.024617
0.115058 -0.025037
0.121907 -0.025423
0.128773 -0.025777
0.135653 -0.026102
0.142546 -0.026400
0.149450 -0.026673
0.156366 -0.026922
0.163292 -0.027149
0.170227 -0.027355
0.177170 -0.027541
0.184120 -0.027708
0.191077 -0.027858
0.198039 -0.027991
0.205007 -0.028109
0.211980 -0.028211
0.218958 -0.028299
0.225940 -0.028373
0.232927 -0.028435
0.239917 -0.028484
0.246911 -0.028521
0.253909 -0.028548
0.260909 -0.028563
0.267911 -0.028569
0.274916 -0.028565
0.281922 -0.028551
0.288929 -0.028528
0.295938 -0.028496
0.302948 -0.028455
0.309960 -0.028405
0.316973 -0.028347
0.323987 -0.028282
0.331002 -0.028208
0.338018 -0.028126
0.345036 -0.028037
0.352054 -0.027941
0.359073 -0.027837
0.366093 -0.027727
0.373114 -0.027610
0.380136 -0.027486
0.387157 -0.027355
0.394179 -0.027217
0.401202 -0.027074
0.408224 -0.026923
0.415246 -0.026767
0.422269 -0.026604
0.429290 -0.026434
0.436312 -0.026258
0.443333 -0.026076
0.450354 -0.025887
0.457374 -0.025692
0.464393 -0.025490
0.471412 -0.025281
0.478429 -0.025064
0.485445 -0.024841
0.492459 -0.024609
0.499470 -0.024369
0.506477 -0.024121
0.513478 -0.023865
0.520474 -0.023598
0.527463 -0.023322
0.534445 -0.023035
0.541422 -0.022735
0.548392 -0.022423
0.555358 -0.022097
0.562322 -0.021757
0.569285 -0.021401
0.576250 -0.021032
0.583218 -0.020650
0.590190 -0.020254
0.597168 -0.019847
0.604153 -0.019430
0.611144 -0.019001
0.618144 -0.018564
0.625151 -0.018118
0.632165 -0.017665
0.639187 -0.017206
0.646215 -0.016742
0.653248 -0.016274
0.660286 -0.015804
0.667327 -0.015332
0.674369 -0.014860
0.681412 -0.014388
0.688453 -0.013917
0.695491 -0.013447
0.702527 -0.012979
0.709560 -0.012513
0.716589 -0.012050
0.723615 -0.011591
0.730637 -0.011136
0.737655 -0.010685
0.744671 -0.010240
0.751683 -0.009800
0.758693 -0.009367
0.765700 -0.008940
0.772705 -0.008521
0.779709 -0.008110
0.786710 -0.007707
0.793710 -0.007312
0.800707 -0.006927
0.807701 -0.006551
0.814692 -0.006185
0.821680 -0.005830
0.828664 -0.005486
0.835644 -0.005155
0.842621 -0.004836
0.849595 -0.004530
0.856566 -0.004239
0.863534 -0.003962
0.870500 -0.003700
0.877463 -0.003453
0.884422 -0.003224
0.891375 -0.003011
0.898320 -0.002817
0.905257 -0.002642
0.912185 -0.002489
0.919104 -0.002358
0.926015 -0.002252
0.932917 -0.002170
0.939810 -0.002114
0.946691 -0.002086
0.953555 -0.002085
0.960388 -0.002116
0.967155 -0.002182
0.973807 -0.002285
0.980260 -0.002431
0.986376 -0.002622
0.991993 -0.002856
0.996864 -0.003124
0.999629 -0.003310

B. Experimental Data

α [°]	$\mathbf{C}_l$ [-]	$\mathbf{C}_d$ [-]
-6.0039468	-0.4257569	0.03848234
-5.0040373	-0.3412285	0.02653079
-3.9855325	-0.2519655	0.01985464
-2.9976936	-0.1644987	0.01385956
-2.0015965	-0.0908013	0.01270549
-1.0186092	-0.0016648	0.01131424
-0.031047	0.11396759	0.01073511
0.99530845	0.23366727	0.01356384
2.01050842	0.42329682	0.01437225
3.0035979	0.54177488	0.01364288
3.99752272	0.6370707	0.01504989
5.01920815	0.73393207	0.01562811
6.00940942	0.82167172	0.0174235
7.00114765	0.89600171	0.02077103
8.01165511	0.95136208	0.02765274
8.99678783	0.99542194	0.03766983
9.99269201	1.03286607	0.05150841
10.9993454	1.0811825	0.07965379
12.0333084	1.06183603	0.13268486
13.0094868	1.00833738	
14.0223784	0.93686136	
15.0254546	0.91436019	
16.0107684	0.91295509	

Table B.1.: Experimental data for clean RG-15 at Re = 100 000.

α [°]	$\mathbf{C}_l$ [-]	$\mathbf{C}_d$ [-]
-5.993554245	-0.420999422	0.032718379
-4.997218247	-0.337218144	0.020781279
-3.999137517	-0.245795931	0.015654139
-2.995749217	-0.143869882	0.011595127
-2.013753079	-0.053697639	0.009956501
-1.001278795	0.037208677	0.009540044
-0.015744977	0.172248044	0.009826774
1.012638844	0.330481795	0.009448928
2.007594692	0.439821006	0.00928974
2.999866656	0.536958894	0.009933913
4.004417394	0.637193881	0.010749377
4.995527991	0.733838974	0.012086141
6.004927774	0.82333839	0.013942084
6.99805932	0.90057276	0.01709252
7.990739837	0.961652447	0.021778509
9.016059018	1.009316483	0.028595246
10.00823958	1.043749669	0.038271508
10.99689584	1.093155228	0.061178381
12.00926311	1.077642059	
13.02664666	1.060768582	
14.02039326	1.002824978	
14.99924856	0.944222925	
16.01414019	0.924186647	

Table B.2.: Experimental data for clean RG-15 at Re = 200 000.

α [°]	$\mathbf{C}_l$ [-]	$\mathbf{C}_d$ [-]
-6.010052224	-0.424346413	0.031880013
-5.016544372	-0.341890343	0.018165763
-3.987094416	-0.242918303	0.013996461
-2.988625855	-0.137118018	0.01086715
-2.002635187	-0.036008906	0.008973927
-1.008536205	0.095715729	0.00860594
-0.063778893	0.218694335	0.007715089
1.003962791	0.336721165	0.007370272
1.989762956	0.440216195	0.007823953
3.004483538	0.546077942	0.008612204
4.000488552	0.649542125	0.00958474
5.018759306	0.750739877	0.010949929
6.003974648	0.839255175	0.012957931
6.98544995	0.918156137	0.015427489
8.005004656	0.98790901	0.019237496
8.990051011	1.037508736	0.024533053
10.03092139	1.076520282	0.031090478
11.03043414	1.101311768	0.0435882
12.00010113	1.107255353	
13.00317614	1.10225711	
14.00591076	1.055545748	
15.01392153	0.990245339	
16.00187373	0.956295885	

Table B.3.: Experimental data for clean RG-15 at Re = 300 000.

α [°]	$\mathbf{C}_l$ [-]	$\mathbf{C}_d$ [-]
-5.996486576	-0.45696644	0.072147484
-5.020848247	-0.349360306	0.057818447
-4.006971349	-0.245770122	0.050564171
-2.994842456	-0.143806376	0.045010569
-1.996550021	-0.044369718	0.041346047
-1.004693435	0.057566432	0.039755888
0.000788219	0.161607969	0.039463773
0.997170234	0.263272116	0.041293774
2.017032367	0.369995825	0.044677899
3.003334178	0.473288916	0.049790759
3.995306654	0.571278496	0.058527814
5.010923354	0.668866973	0.071389118
6.002703309	0.75535727	0.083360891
6.997344938	0.815369458	0.105046782
8.014921605	0.837046833	0.126278799
9.004420727	0.794303307	0.138683101
9.996422353	0.704103178	
11.00743093	0.689480578	
12.01133751	0.704171014	

Table B.4.: Experimental data for RG-15 with glaze ice at Re = 100 000.

α [°]	$\mathbf{C}_l$ [-]	$\mathbf{C}_d$ [-]
-6.042967499	-0.451265037	0.071232301
-5.00779066	-0.34634978	0.058372245
-4.00805341	-0.245716554	0.050252754
-2.988400248	-0.140559942	0.044623346
-2.008295649	-0.04114668	0.040751647
-0.987110521	0.067526828	0.038687153
-0.004399006	0.170935888	0.038349349
0.994959087	0.276714738	0.039453208
2.023040311	0.387153161	0.04295253
3.000614731	0.488705579	0.047845815
3.989805991	0.584854942	0.055994346
4.989883808	0.680205859	0.065717338
5.990652717	0.768065129	0.078036004
7.02706552	0.839216952	0.099956713
8.017622776	0.859110194	
8.997548014	0.843047408	
9.996787357	0.799889811	
11.00495153	0.748573207	
11.99011446	0.734672437	

Table B.5.: Experimental data for RG-15 with glaze ice at Re = 200 000.

α [°]	$\mathbf{C}_l$ [-]	$\mathbf{C}_d$ [-]
-6.000742674	-0.456563306	
-5.000270609	-0.351166025	0.059549492
-4.002245756	-0.245332922	0.051109669
-2.988800983	-0.13767422	0.044813796
-1.990526127	-0.032932397	0.040912851
-1.014708962	0.072035998	0.038768681
0.007258474	0.18248233	0.038142286
1.014070554	0.29021507	0.039633993
2.001470876	0.398620465	0.042840415
2.990810811	0.501190929	0.048170689
3.984757934	0.598937457	0.055848999
5.035894509	0.69845775	0.065420279
6.028984221	0.782427659	
7.009323728	0.848830597	
7.993709681	0.865890744	
9.025281263	0.84753761	
9.991199118	0.816675188	
11.01430442	0.769674808	
12.01653638	0.745519625	

Table B.6.: Experimental data for RG-15 with glaze ice at Re = 300 000.

α [°]	$\mathbf{C}_l$ [-]	$\mathbf{C}_d$ [-]
-6.016528984	-0.481534312	
-4.997486236	-0.374038092	0.064673963
-3.991424754	-0.253900385	0.044123375
-3.009769945	-0.152776199	0.036115921
-2.007987728	-0.049338454	0.032162764
-1.005152744	0.053578184	0.030602954
-0.00473813	0.157595306	0.030464931
1.005764118	0.266658599	0.031193121
2.011404993	0.37439029	0.032810708
3.00006989	0.479730739	0.035954408
3.985702577	0.578704968	0.040361745
4.999161573	0.669456556	0.046329311
5.980331621	0.756606357	0.054948568
7.009799198	0.84690103	0.067424568
8.002394787	0.919968158	0.087113237
8.97814086	0.97494039	
9.992103126	1.006395997	
10.99718446	1.022822188	
11.99442028	1.018686564	
13.00184254	1.023928195	
14.01475899	1.019722244	
15.01287252	0.965213688	
16.08249895	0.491483806	

Table B.7.: Experimental data for RG-15 with mixed ice at Re = 100 000.

α [°]	$\mathbf{C}_l$ [-]	$\mathbf{C}_d$ [-]
-5.998644979	-0.441835444	0.066040685
-4.995031759	-0.340233908	0.051815032
-3.990514723	-0.23859853	0.040354501
-2.993687495	-0.140352181	0.034243733
-2.007511045	-0.039580963	0.030830287
-0.996440315	0.065022542	0.029415008
0.007713986	0.171051386	0.029500085
0.991926355	0.274659284	0.0302223
2.008399089	0.383220187	0.032214874
2.988620385	0.484895444	0.035209304
4.01020847	0.586240869	0.039603786
4.991322136	0.681393735	0.045664708
5.990948271	0.771959703	0.053758211
7.009163717	0.857555519	0.0657417
8.000407975	0.930510642	0.081108093
9.009923468	0.983786662	
10.01491591	1.019658328	
11.00237205	1.033396599	
12.00996106	1.039883524	
12.97450863	1.048368939	
13.99739658	1.053275645	
14.98747896	1.055398414	
15.98561935	1.04526091	

Table B.8.: Experimental data for RG-15 with mixed ice at Re = 200 000.

α [°]	$\mathbf{C}_l$ [-]	$\mathbf{C}_d$ [-]
-6.001335728	-0.428467231	0.057451965
-5.012839129	-0.337378599	0.048054809
-4.018369735	-0.239715568	0.039411239
-2.990585887	-0.138111103	0.033891492
-2.013577351	-0.037389283	0.030959553
-1.014430846	0.06633176	0.029793541
0.013641034	0.173991281	0.029762264
0.995396419	0.281084956	0.030388112
2.006432463	0.390591412	0.032249188
3.012858506	0.494684268	0.034941235
3.979022108	0.592880595	0.039036637
5.013576648	0.692933121	0.045689968
5.994908103	0.778913984	0.053256003
7.02659683	0.861509554	0.063787105
7.995927261	0.931478629	
9.051420239	0.988278954	
10.0126705	1.023202191	
10.98276768	1.04321121	
11.97287446	1.051831368	
12.98599075	1.054548788	
13.98047099	1.057437529	
14.97574688	1.055945713	
16.02697127	1.038376404	

Table B.9.: Experimental data for RG-15 with mixed ice at Re = 300 000.

α [°]	$\mathbf{C}_l$ [-]	$\mathbf{C}_d$ [-]
-6.012639236	-0.431060282	0.044600345
-5.005997029	-0.330230819	0.031303598
-4.003264252	-0.232282257	0.02728057
-2.991471974	-0.135919289	0.024764
-2.006211601	-0.037555968	0.024495072
-1.009012893	0.061097902	0.02381576
-0.000498879	0.163927514	0.024467848
1.014193325	0.271068286	0.024968275
1.999588187	0.37419666	0.025358105
2.995487794	0.476773379	0.026352681
4.007878797	0.576484071	0.028401594
5.01641348	0.669865793	0.030270756
6.001436198	0.753449287	0.033328292
7.027495876	0.831279288	0.037947564
8.00657082	0.905698647	0.04140594
9.018755559	0.970606781	0.046576575
10.00043636	1.020010058	0.052958774
10.99267104	1.073396548	0.064628307
11.90471287	1.134006071	
13.02466065	1.173028702	
13.98164908	1.172120847	
15.02104835	1.151284265	
16.01078427	1.112811656	

Table B.10.: Experimental data for RG-15 with rime (-10°C) ice at Re = 100 000.

α [°]	$\mathbf{C}_l$ [-]	$\mathbf{C}_d$ [-]
-5.988622752	-0.426563053	0.051296699
-5.003447005	-0.330963055	0.033215246
-3.990089277	-0.23231296	0.028226756
-2.995202034	-0.135210788	0.025700386
-1.983351856	-0.033426576	0.02406372
-1.012291688	0.065999721	0.02271167
-0.010001917	0.169262232	0.022664552
1.011477126	0.276632161	0.023590035
2.007607367	0.380985366	0.024628435
2.994995205	0.482690774	0.025920106
3.999669815	0.58176204	0.028017538
4.997852611	0.674181964	0.030485928
6.018127437	0.761708369	0.034108008
6.981390285	0.839009212	0.037626028
8.004447081	0.911047283	0.04169023
8.992296321	0.96593365	0.046856974
9.980687247	1.01601516	0.05317322
10.97347375	1.050336343	0.062744183
12.01771692	1.070951271	0.081545995
12.98711025	1.170317126	
13.9958249	1.185483758	
14.99328779	1.186203066	
15.99664882	1.175670451	

Table B.11.: Experimental data for RG-15 with rime (-10°C) ice at Re = 200 000.

α [°]	$\mathbf{C}_l$ [-]	$\mathbf{C}_d$ [-]
-5.997013223	-0.429939736	
-5.008339534	-0.33083308	0.033168456
-3.990048654	-0.228181777	0.028201164
-3.014351613	-0.127683607	0.025503734
-2.004803199	-0.027228937	0.023901089
-0.997106764	0.079367341	0.022873301
-0.007165107	0.182381507	0.022563058
0.991646839	0.288063765	0.02331153
2.013472635	0.397230536	0.024467807
3.006905876	0.499812048	0.025830967
4.008467001	0.599532793	0.027904606
5.012361093	0.696895068	0.030481588
6.014518806	0.787497778	0.033444895
7.012502186	0.874428487	0.036888987
8.023209908	0.952632441	0.040925432
8.992537287	1.018279812	0.045661693
9.995632713	1.077471956	0.051681762
10.98050773	1.128360026	0.05967648
12.00631071	1.193923968	
13.00424768	1.219067634	
14.02455842	1.228188628	
15.00722358	1.230164644	
15.99506882	1.233143931	

Table B.12.: Experimental data for RG-15 with rime (-10°C) ice at Re = 300 000.

α [°]	$\mathbf{C}_l$ [-]	$\mathbf{C}_d$ [-]
-6.010110841	-0.477774267	0.065935735
-5.010346742	-0.371713438	0.040052059
-3.997239633	-0.282044033	0.030444062
-3.00676702	-0.192590658	0.02551081
-2.01068646	-0.084095147	0.022404878
-1.001536558	0.047976216	0.018914705
0.006727982	0.191136393	0.015056975
1.00226418	0.298360157	0.014891917
2.00091558	0.390500566	0.01547828
3.000191433	0.487750595	0.017159873
4.009565457	0.585548326	0.019754885
5.006880629	0.682362184	0.022598651
5.999408006	0.774143042	0.025425774
7.000622498	0.863511705	0.028495061
8.001966004	0.948328962	0.031481554
9.001572847	1.021415661	0.036050575
9.989608093	1.088051299	0.039311148
11.00757524	1.146542059	0.044169108
12.00437292	1.168760977	0.051787446
13.00368928	1.164768511	0.064448095
14.00147357	1.159296271	
15.00222855	1.134608464	
15.98915755	1.101512709	

Table B.13.: Experimental data for RG-15 with rime (-15°C) ice at Re = 100 000.

α [°]	$\mathbf{C}_l$ [-]	$\mathbf{C}_d$ [-]
-5.99971759	-0.46271502	0.065614705
-5.00193176	-0.337492131	0.03782849
-3.997504836	-0.235297994	0.029677585
-2.991595264	-0.132901805	0.025997431
-2.011158775	-0.03288632	0.024020858
-1.006300924	0.071369891	0.022921463
0.018309336	0.180723312	0.022551817
0.990796989	0.283633603	0.022378015
1.987705118	0.390678267	0.02317232
2.992468003	0.497499069	0.024013905
3.988970313	0.600719292	0.02513436
4.989538644	0.702097849	0.026414364
6.003207338	0.799048599	0.02815767
6.990358865	0.887225303	0.030153667
8.005677442	0.96579876	0.033814656
9.009427022	1.036142629	0.038378282
10.00454933	1.095159016	0.04416094
10.99720389	1.134765647	0.052315556
12.02248035	1.123512086	0.071431984
12.9907556	1.105107548	
13.99666716	1.07802694	
15.01477884	1.054065889	
16.00304327	1.040556603	

Table B.14.: Experimental data for RG-15 with rime (-15°C) ice at Re = 200 000.

α [°]	$\mathbf{C}_l$ [-]	$\mathbf{C}_d$ [-]
-6.017613828	-0.477583704	0.067886644
-4.9828656	-0.346818777	0.040134332
-4.014421683	-0.2446977	0.030545159
-2.992965128	-0.137061538	0.026422934
-2.009414798	-0.034609226	0.024534436
-1.008470843	0.073023987	0.02313558
-0.02039631	0.181215941	0.022528342
0.984491211	0.292969922	0.022670364
1.991626692	0.40501911	0.023250653
3.006629259	0.515670079	0.024143403
4.019399807	0.624275854	0.024944188
4.993488307	0.722387871	0.02648617
6.009182551	0.820068435	0.028358031
7.00689272	0.909822155	0.030964416
8.006400413	0.99359557	0.034133134
9.010305074	1.069383197	0.038179614
10.0162766	1.134287725	0.043770698
11.00403909	1.178945984	0.051916215
11.99523686	1.167383067	0.072029237
13.01851355	1.124405368	
14.00818905	1.083071586	
15.00532089	1.057115779	
15.99832192	1.050410349	

Table B.15.: Experimental data for RG-15 with rime (-15°C) ice at Re = 300 000.

C. Normalized Polars of Rime Ice Shapes

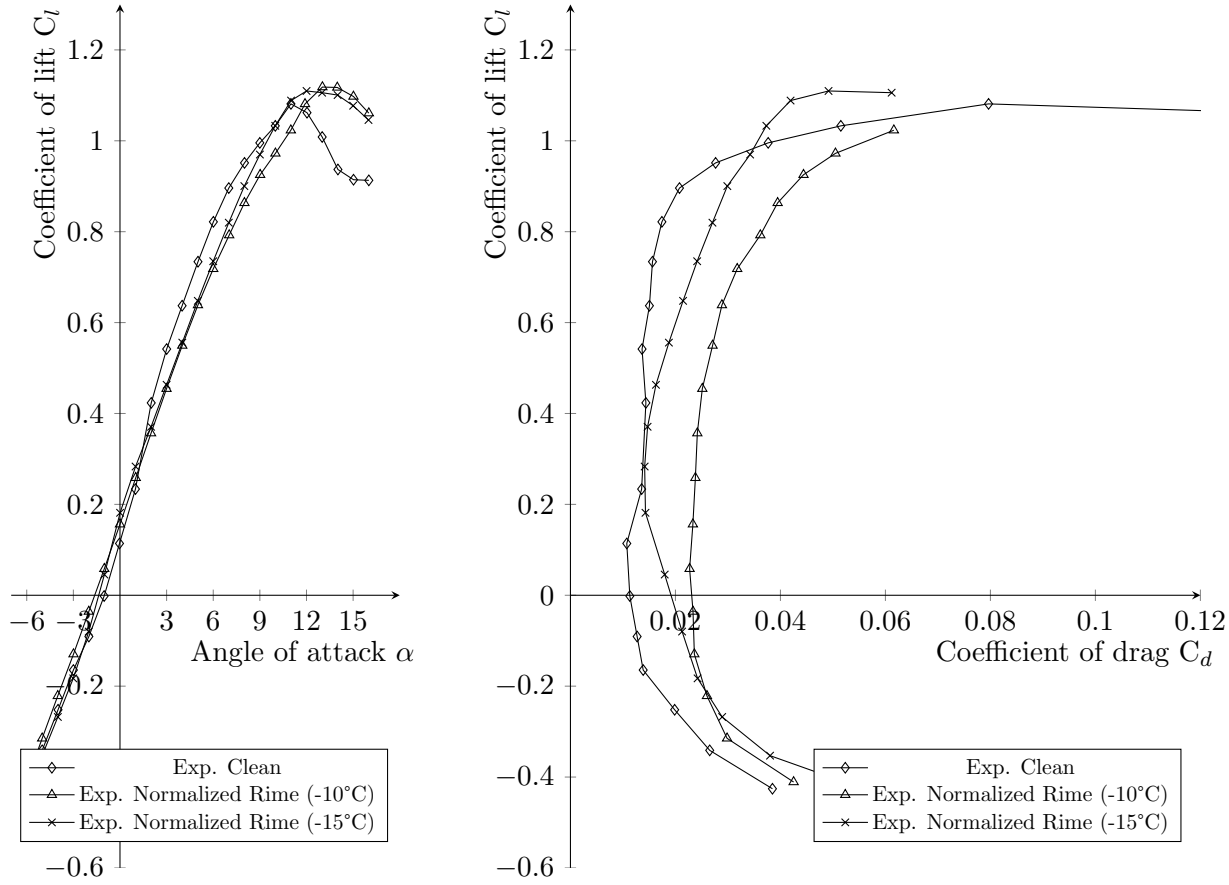

Figure C.1.: Comparison of normalized results of rime (-10°C) and rime (-15°C) ice with clean airfoil at Re = 100 000.

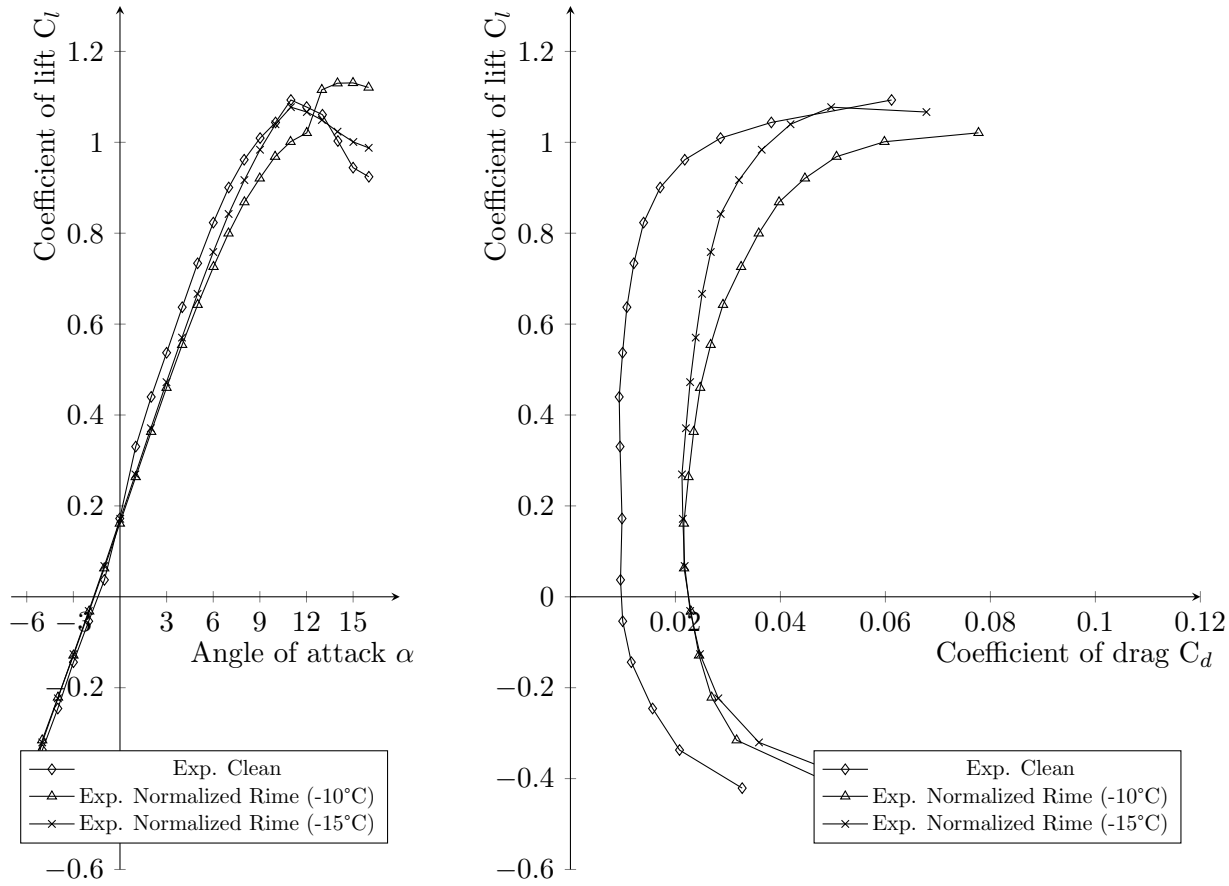

Figure C.2.: Comparison of normalized results of rime (-10°C) and rime (-15°C) ice with clean airfoil at Re = 200 000.

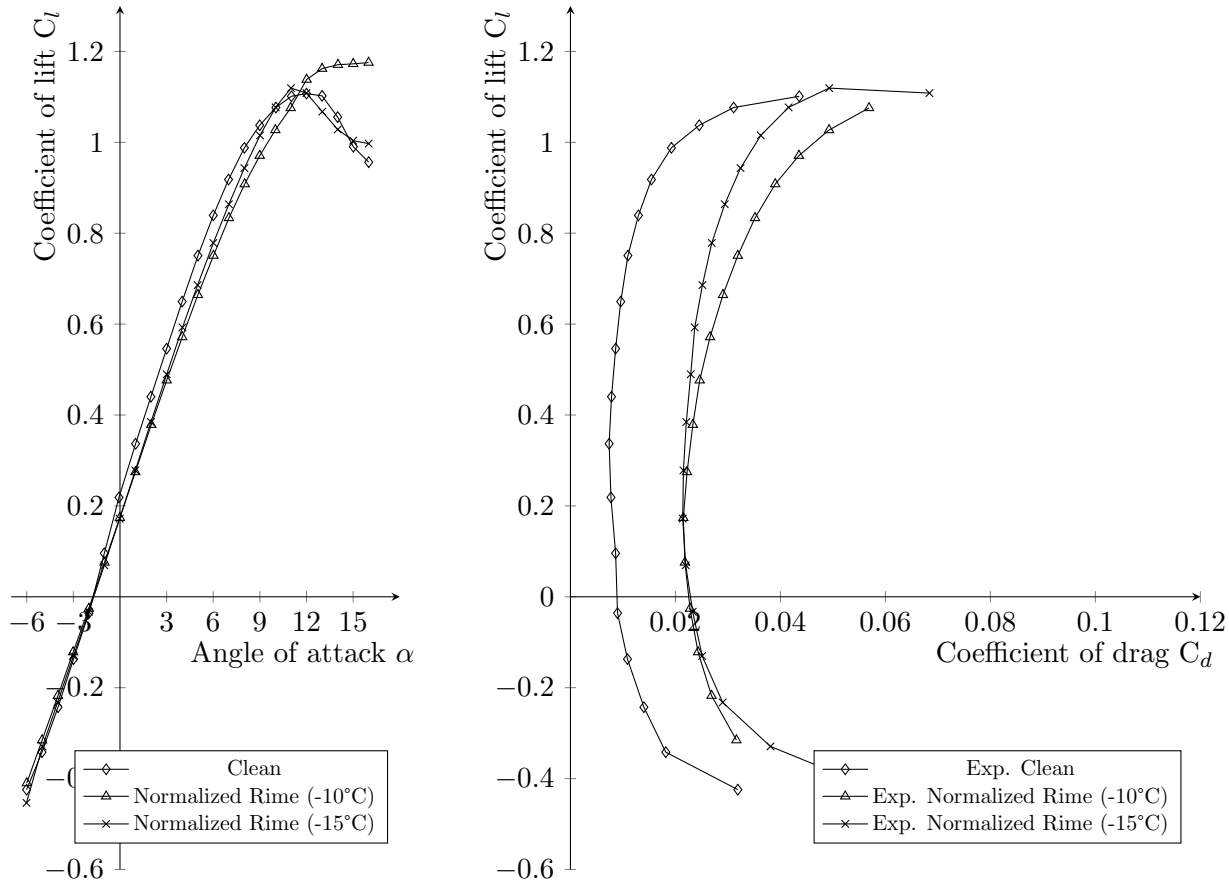

Figure C.3.: Comparison of normalized results of rime (-10°C) and rime (-15°C) ice with clean airfoil at Re = 300 000.